공학박사학위논문

임의 단면을 갖는 박판 보 연결 구조의 일차원 모델링

One-dimensional Modeling of Thin-walled Beams with Arbitrary Cross-sections and Their Jointed Structures

2021년 2월

서울대학교 대학원

기계항공공학부

김 재 용

임의 단면을 갖는 박판 보 연결 구조의 일차원 모델링

One-dimensional Modeling of Thin-walled Beams with Arbitrary Cross-sections and Their Jointed Structures

지도교수 김 윤 영

이 논문을 공학박사 학위논문으로 제출함

2020 년 10 월

서울대학교 대학원

기계항공공학부

김 재 용

김재용의 공학박사 학위논문을 인준함

2020 년 12 월

위 원 장 : 윤 병 동 (인)

부위원장 : 김 윤 영 (인)

위 원 : 김 도 년 (인)

위 원 : 최 수 민 최수민

위 원 : 장 강 원 (인)

ABSTRACT

One-dimensional Modeling of Thin-walled Beams with Arbitrary Cross-sections and Their Jointed Structures

Jaeyong Kim
School of Mechanical and Aerospace Engineering
The Graduate School
Seoul National University

In a one-dimensional analysis model, displacement field is expressed by cross-section modes. In the classical beam theories, since only six rigid-body cross-section modes are considered, detailed behaviors cannot be expressed, leading to a stiffer structural rigidity compared to three-dimensional analysis models. This limitation can be overcome by considering higher-order modes that represent distortion or warping deformations of a cross-section. Although an accurate analysis of a single beam can be made through this advanced approach, it also arouses another difficulty when analyzing beam structures like space frames. At

joints of a beam structure, where multiple beams are connected, joint conditions are needed to define coupling relations of the cross-section modes. In the classical beam theories, a coordinate transformation matrix for the rigid-body cross-section modes can be used as a joint condition. However, when considering the higher-order modes in addition to the rigid-body cross-section modes, a standard transformation is no longer valid, since the higher-order modes have no resultant.

In this thesis, fist, a new process to derive cross-section modes is proposed. Equations of cross-section modes are derived from the constitutive relations for a plane stress state, then, the equations are transformed to an eigenvalue problem using mode orthogonality condition. Finally, a set of the cross-section modes are defined through the inner products of a basis function vector and obtained eigenvectors. As this process is repeated, the cross-section modes are recursively derived from the lowest set to higher sets.

Second, this thesis proposes a new joint condition that is applicable to a joint of thin-walled beams analyzed by the higher-order modes as well as the six-rigid body modes. The proposed joint condition is defined using the continuities in displacements and rotations at designated connection points along the beam sections. The proposed joint condition two unique features; the connection points are set in a consistent way, and additional displacements induced by mismatch between the beam section and the joint section are taken into account. Without this theory using these features, accurate analyses of complicated beam structures would be impossible.

Several numerical case studies covered in this dissertation show that the proposed approaches for the one-dimensional modeling are appropriate to analyze a complicated beam structure with arbitrary sectioned members.

Keywords: Thin-walled beam, Cross-section mode, Higher-order beam theory, Beam structure, Joint condition, Mode coupling relation

Student Number: 2016-30174

CONTENTS

LIST OF TABLES

LIST OF FIGURES

CHAPTER 1.
INTRODUCTION

1.1 Motivation and literature survey

The inclusion of higher-order cross-section modes in addition to 6 fundamental rigid-body cross-section modes is crucial for an accurate beam-based analysis of thin-walled beams. Since Vlasov [1] demonstrated that the accuracy of the torsional stiffness of thin-walled beams can be significantly improved by adding warping modes, various studies have been conducted to find higher-order modes of thin-walled cross-sections. Carrera et al. [2-4] expressed cross-section deformations using polynomial functions defined through the Lagrangian expansion or Taylor expansion. Beside, approaches that assume a thin-walled cross-section as a beam frame and define free vibration modes as cross-section modes were also presented [5-8].

For the analysis of thin-walled beams, recent studies focus on the derivation of cross-section modes by decomposing a three-dimensional continuum problem into a cross-section analysis and a one-dimensional analysis. In the generalized beam theory (GBT), proposed by Schardt [9-11] and significantly improved by Camotim et al. [12-17], the cross-section modes are derived starting from initial modes of a discretized cross-section. The strain energy by the initial modes can be represented in a matrix form using initial mode vectors and matrices of the sectional constants. By combining the initial modes with eigenvectors of the matrices of sectional constants, higher-order cross-section modes can be derived. Garcea and his colleagues proposed the method of generalized eigenvectors (GE) [18-23]. In the GE method, initial displacement fields are represented by two-dimensional discretization, and cross-section modes are defined based on the Saint-Venant (SV) rod theory [24], inspired by other SV theory-based works [25-28]. Vieira et al. [29-31] also employed a generalized eigenvector approach for a cross-section analysis of thin-walled beams. The validities of the GBT and the GE method have been confirmed in static, vibration and buckling analyses. Also, Hodges et al. [32-34] proposed the variational asymptotic beam sectional analysis (VABS), defining cross-section modes through an asymptotic analysis of an energy functional, and Kim et al. [35-40] derived warping and distortion modes using orthogonality condition among the cross-section modes.

These advancements of beam theories have led to the accurate and efficient one-dimensional analyses. At the same time, however, the introduction of these higher-order modes makes it difficult to define joint condition that means the coupling relations of cross-section modes at a joint where multiple beams are connected as shown in Fig. 1.1.

The joint condition is essential to analyze beam structures like space frames of buildings or vehicle frames. In the classical beam theories that use six rigid-body modes only, the joint condition can be easily defined by using a coordinate transformation matrix, since their directions are defined on the cross-section as illustrated in Fig. 1.2(a). However, in the higher-order beam theories, coupling relations of the cross-section modes cannot be defined using the coordinate transformation matrix, since a higher-order mode does not generate the resultant that defines the direction on the cross-section as can be seen in Fig. 1.2(b). For this reason, some researchers have applied the spring stiffness into the joints of the classical beam models, rather than introducing the higher-order modes. In these approaches, spring stiffnesses are assessed through experimental [41, 42] or numerical studies [43-45], or are calculated by using the sectional moment of inertia [46, 47]. Some authors used these beam-spring models to analyze complicated structures like vehicle frames [45, 48, 49]. Donders et al. used a shell element-based super element to evaluate joint flexibility more accurately [50, 51], rather than using spring stiffness. However, these classical beam-based approaches have limitations in that the torsional stiffness of each beam member cannot be assessed correctly by the classical beam theories. Also, local deformations occurred near the joints cannot be captured by the spring elements.

To overcome the limitations of the classical beam-based approaches, many attempts have been made to define the joint condition for the higher-order modes. In the early days, studies were mainly conducted to identify the warping transmission mechanism at the joints of open-sectioned thin-walled beams that are used in space frames [52-54], and later, researches have been conducted to define the coupling relations of more complicated higher-order modes at the joints. Choi et al. defined coupling relations of warping and distortion modes at the joints where two box beams are connected [55, 56]. In their method, the joint condition is initially set as an unknown square matrix. To fine the unknown components in the matrix, they use displacement and rotation continuities as well as linear algebraic conditions. Also, in their later study [37], they developed the conditions to be applicable to the joints where three or more beams are connected. To do this, they proposed the consideration of the equilibrium of edge resultants that mean the forces and moments calculated for each cross-section edge. Although their approaches lead to effective and consistent joint conditions for beam structures, their joint conditions are limited only to the rectangular cross-sections. Jang at al. proposed a cross-sectional displacement continuity at the joints [57-61]. They introduced a virtual section that is referred to as the joint section to define displacements at the joint. Then they defined the joint condition by minimizing the mismatches of displacements on the joint section. Due to the condition of minimization, the joint condition is defined as a square matrix. Although they showed excellent performances for various cross-sections, their approach is appropriate only for the joint where two beams are connected, since the minimization process becomes complicated when three or more beams are connected [61]. In the GBT, the joint condition is defined by using displacement and rotation continuities at connection points [62-70]. They carefully investigated the joint conditions for various cross-sections, mainly focusing on the open sections that are used in space frames, e.g., C-sections, I-sections and lipped sections. Their method has shown outstanding performances in static, vibration and buckling analyses for various structures. However, their approach is not appropriate for complicated beam structures like vehicle frames, since the way the connection points are set is not consistent depending on the cross-section shapes. Also, the directions of displacement and rotation continuities are not consistent for the points.

1.2 Research objectives

First, we propose a new approach to derive cross-section modes for thin-walled beams with arbitrary cross-sections, by extending the higher-order beam theory (HoBT) of Kim and his colleagues [38, 39]. Compared to other cross-section mode derivation approaches, the proposed method has following advantages. 1) A set of "orthogonal" higher-order modes are derived hierarchically and recursively from four initial rigid-body modes. 2) Due to the orthogonality among the modes and the differential relations between the in-plane and out-of-plane modes, generalized forces can be decoupled in the stress expressions. 3) Mode derivation equations are developed based on field consistency between stress and strain (or constitutive equations). 4) The cross-section shape functions are defined edgewise, so no section discretization is required.

Recently, Choi and Kim [38, 39] determined higher-order modes for rectangular cross-sections using constitutive equations of the plane stress state and mode orthogonality. However, the use of geometric symmetry was essential in their approach, implying that it cannot be applied to cross-sections with general thin-walled shapes. To overcome this difficulty, we propose a new method utilizing an eigenvalue problem, which is formulated using the orthogonality among cross-section modes. A set of higher-order modes are simultaneously derived by combining basis functions with corresponding coefficients, which are obtained as eigenvectors of the eigenvalue problem. By doing so, orthogonal sets of higher-order modes can be uniquely determined for any thin-walled cross-sections with arbitrary geometries, seamlessly extending key features of Choi and Kim [38, 39] while overcoming critical limitation of their work. Once a new set of cross-section modes are calculated, the stress field is updated. The next higher set of modes are determined so that they can satisfy the field consistency; they should represent the strain field induced by the updated stress field. Because lower-order modes make higher contributions to the strain energy, the determination of the level of the highest modes depends on the required accuracy for the analysis.

Second, we present a new consistent and effective method to define the joint condition. The proposed method is inspired by several other studies; displacement and rotation continuities at the connection points are calculated as in the GBT, and the joint section proposed by Jang at el. is used. However, we newly propose some approaches to overcome the limitations in the existing studies. 1) A consistent rule is proposed to set the connection points; the connection points are set at the cross-section corners that mean the end points of each cross-section edge and at the joint axis. This rule is applied consistently regardless of the cross-section shapes. At each connection point, continuities of three dimensional displacements and rotations are imposed. 2) Additional displacements on the joint section are taken into account. Because the cross-section of a beam is normal to the beam axis, the beam section and the joint section do not match in general. Therefore, displacements on the joint sections should be carefully assessed when using field variables of beam theories. The additional displacements on a joint section are calculated by using the rotations on the beam section, leading to the correct calculation of displacements at the joint. Since the warping modes derived by the proposed mode derivation approach meet the C^1 continuity, the rotations at a connection point are uniquely defined. One of the merit of the proposed method is that it can be applied to various shapes of beam structures in a consistent manner.

To verify the effectiveness of the proposed cross-section modes and joint condition, static and vibration problems are solved for thin-walled beams with various shapes of cross-sections. Also, several complicated beam structures like vehicle frame in Fig. 1.3 are analyzed. The results of the proposed approach are shown to be highly accurate when comparing with the results from the shell theory.

1.3 Outline of thesis

The thesis is organized as follows.

In **Chapter 2**, displacement, strain, stress and governing equations are explained in the frame work of the proposed HoBT. Also, this chapter shows that generalized forces are derived from the governing equation, where the generalized forces mean the work conjugates of cross-section modes in beam theories. Since the cross-section modes are derived from the constitutive relations in the proposed HoBT, the stresses are expressed for the generalized forces. At the end of the chapter, a finite element formulation that is used to analyze thin-walled beam structures is presented.

In **Chapter 3**, a new cross-section analysis approach is presented. In the cross-section analysis, equations of cross-section modes of a thin-walled beam are derived from the constitutive relations. The equations are solved by formulating eigenvalue problems using the mode orthogonality. By solving the eigenvalue problems with constraint matrices of mode continuity conditions, cross-section modes are defined. This chapter also shows recursive and hierarchical process of the cross-section mode derivation approach.

In **Chapter 4**, a new coupling relations of the cross-section modes at a joint, or joint conditions, are presented. The proposed joint conditions are derived in a consistent and simple manner, while existing other approaches are inconsistent for the cross-section shapes or too complicated. The consistency and simplicity of the proposed approach make it possible to analyze even complicated structures like a vehicle structure. This chapter shows detailed process to define the joint conditions that are derived by continuities of displacement and rotations at connection points on a thin-walled beam cross-section.

In **Chapter 5**, the overall conclusion of this dissertation is presented.

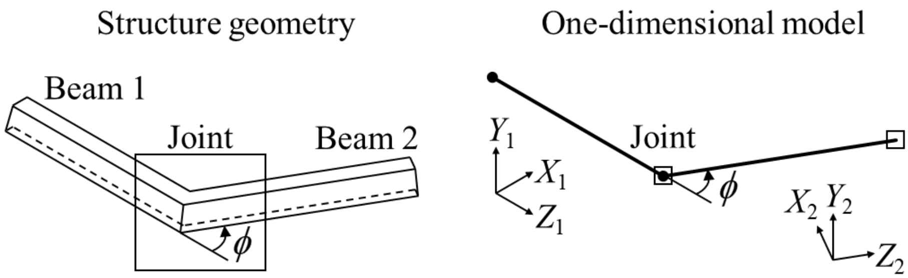

Fig. 1.1 One-dimensional models of L-type and T-type joint structures

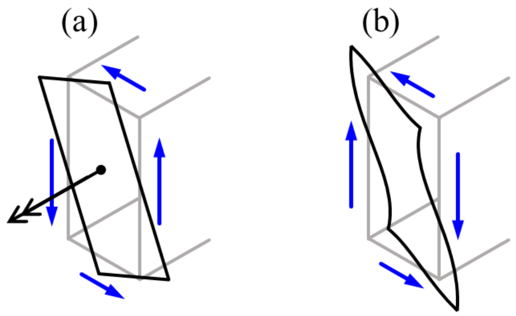

Fig. 1.2 Cross-section modes of a box beam: (a) torsional rotation mode and (b) distortion mode

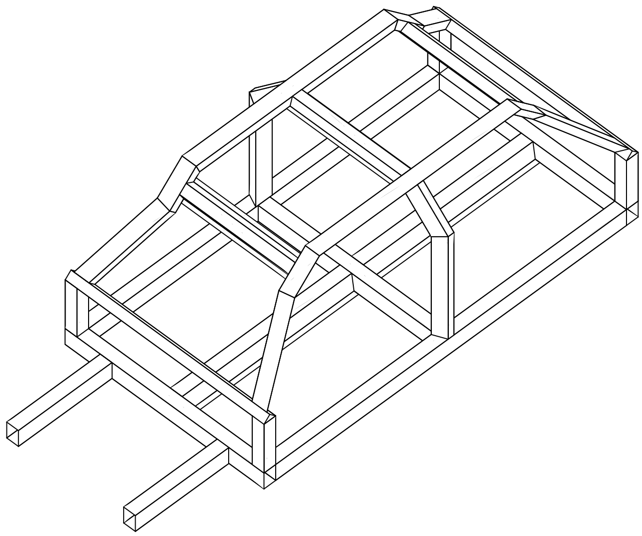

Fig. 1.3 A simplified automotive body frame

CHAPTER 2.
Higher-order beam theory

2.1 Displacement field and governing equations

A thin-walled cross-section consisting of N_E edges is illustrated in Fig. 2.1, where X, Y and Z are the global coordinates and n_e and s_e, defined on the midline of edge e (e = 1, 2, ⋯, N_E), are local coordinates representing normal and shear directions, respectively. The origin of the local coordinates is located at (X_e, Y_e), one of the corners of the edge. The angle of edge e with respect to the X axis is denoted as α_e. In the proposed higher-order beam theory, three-dimensional displacements on the midline are expressed by superposing displacements by each cross-section mode:

$$u_k(s,z)=\sum_{i=1}^{N_D}\psi_k^{\xi_i}(s)\xi_i(z)=\boldsymbol{\psi}_k(s)\boldsymbol{\xi}(z),\ (k=n,s,z), \tag{2.1}$$

where u_k is the k-directional displacement on the midline and $\psi_k^{\xi_i}$ is the shape function for u_k associated with cross-section mode ξ_i (i = 1, 2, ⋯, N_D; N_D: number of cross-section modes). In Eq. (2.1), s is used without denoting the edge index for simplification, and z is the axial coordinate, defined orthogonal with respect to s and n. The cross-section mode vector $\boldsymbol{\xi}$ in Eq. (2.1) consists of six rigid-body modes and higher-order modes as

$$\boldsymbol{\xi} = \left\{\xi_m\right\}_{m=1,\cdots,N_D} = \{U_x, U_y, U_z, \theta_{\bar{x}}, \theta_{\bar{y}}, \theta_z, \xi_7, \cdots, \xi_{N_D}\}^{\mathrm{T}}, \tag{2.2}$$

where $\{U_x, U_y, U_z, \theta_{\bar{x}}, \theta_{\bar{y}}, \theta_z\}$ are the rigid-body modes, and $\{\xi_7, \cdots, \xi_{N_D}\}$ are the higher-order modes. The higher-order modes are grouped into out-of-plane modes (or warping modes) having z-directional deformations only and in-plane modes. In-plane modes are further classified into distortion modes with both n- and s-directional deformations, leading to shear deformations of a cross-section, and wall-bending modes with n-directional deformations only, not accompanying shear deformations. Note in Eq. (2.2) that deflection modes are defined for (x, y) directions while bending rotation modes are defined for principal axes $(\bar{x}, \bar{y})$, because the cross-section modes in the proposed approach are defined orthogonal each other. The directions and the center of (x, y) and $(\bar{x}, \bar{y})$ are given in Chapter 3 and Appendix A, respectively.

Using the displacement on the midline, the three-dimensional displacement $\tilde{u}_k$ (k = n, s, z) at a generic point on the cross-section can be written as

$$\tilde{u}_n(n,s,z) = u_n(s,z), \tag{2.3a}$$

$$\tilde{u}_s(n,s,z) = u_s(s,z) - n\dot{u}_n(s,z) = u_s(s,z) + \bar{u}_s(n,s,z), \tag{2.3b}$$

$$\tilde{u}_z(n,s,z) = u_z(s,z) - nu_n'(s,z) = u_z(s,z) + \bar{u}_z(n,s,z), \tag{2.3c}$$

where $(\dot{\ }) = \partial(\ )/\partial s$ and $(\ )' = \partial(\ )/\partial z$. In Eqs. (2.3b, c), displacements by wall bending are given as the derivatives of u_n according to the Kirchhoff plate theory, expressed as $\bar{(\ )}$. The approximations of three-dimensional displacements in Eqs. (2.1, 3) are the same as in the GBT [12-17] except for the use of $\xi_i(z)$, not its derivative form, for the axial displacement.

Assuming a plane stress state, the stress $(\tilde{\sigma})$ and strain (normal component $\tilde{\varepsilon}$ and shear component $\tilde{\gamma}$) are calculated as

$$\tilde{\varepsilon}_{ss} = \dot{\tilde{u}}_s = \dot{u}_s - n\ddot{u}_n, \tag{2.4a}$$

$$\tilde{\varepsilon}_{zz} = \tilde{u}_z' = u_z' - nu_n'', \tag{2.4b}$$

$$\tilde{\gamma}_{zs} = \tilde{u}_s' + \dot{\tilde{u}}_z = u_s' + \dot{u}_z - 2n\dot{u}_n', \tag{2.4c}$$

$$\tilde{\sigma}_{ss} = E_1(\tilde{\varepsilon}_{ss} + v\tilde{\varepsilon}_{zz});\ \tilde{\sigma}_{zz} = E_1(v\tilde{\varepsilon}_{ss} + \tilde{\varepsilon}_{zz});\ \tilde{\sigma}_{zs} = G\tilde{\gamma}_{zs}, \tag{2.5}$$

where $E_1=E/(1-v^2)$, and E, v and G represent the Young's modulus, Poisson's ratio, and the shear modulus, respectively.

Using the displacement, strain and stress fields, the total potential energy of a thin-walled beam can be written as:

$$\begin{aligned}\prod &= U + \Omega \\ &= \frac{1}{2}\int_V (\tilde{\sigma}_{ss}\tilde{\varepsilon}_{ss} + \tilde{\sigma}_{zz}\tilde{\varepsilon}_{zz} + \tilde{\sigma}_{zs}\tilde{\gamma}_{zs})dV - \int_V (f_n\tilde{u}_n + f_s\tilde{u}_s + f_z\tilde{u}_z)dV,\end{aligned} \tag{2.6}$$

where U is the internal strain energy and Ω is an external work done by body forces, f_n, f_s and f_z [N/m^3]. In Eq. (2.6), one end of a beam (z=0) is fixed while surface tractions t_{zz} and t_{zs} are imposed on the other end, z=L. The strain energy can be expressed using Eqs. (2.1) and (2.3-2.5):

$$U = U_1 + U_2 + U_3 + U_4 + U_5, \tag{2.7a}$$

where

$$U_1 = \frac{1}{2}\int_z \boldsymbol{\xi}^{\mathrm{T}} \int_A \left[E_1 \left(\dot{\boldsymbol{\psi}}_s^{\mathrm{T}} \dot{\boldsymbol{\psi}}_s + n^2 \ddot{\boldsymbol{\psi}}_n^{\mathrm{T}} \ddot{\boldsymbol{\psi}}_n \right) + G \dot{\boldsymbol{\psi}}_z^{\mathrm{T}} \dot{\boldsymbol{\psi}}_z \right] dA \boldsymbol{\xi} dz, \tag{2.7b}$$

$$U_2 = \int_z \boldsymbol{\xi}^{\mathrm{T}} \int_A \left(\nu E_1 \dot{\boldsymbol{\psi}}_s^{\mathrm{T}} \boldsymbol{\psi}_z + G \dot{\boldsymbol{\psi}}_z^{\mathrm{T}} \boldsymbol{\psi}_s \right) dA \boldsymbol{\xi}' dz, \tag{2.7c}$$

$$U_3 = \frac{1}{2}\int_z \boldsymbol{\xi}'^{\mathrm{T}} \int_A \left[E_1 \boldsymbol{\psi}_z^{\mathrm{T}} \boldsymbol{\psi}_z + G \left(\boldsymbol{\psi}_s^{\mathrm{T}} \boldsymbol{\psi}_s + 4n^2 \dot{\boldsymbol{\psi}}_n^{\mathrm{T}} \dot{\boldsymbol{\psi}}_n \right) \right] dA \boldsymbol{\xi}' dz, \tag{2.7d}$$

$$U_4 = \int_z \boldsymbol{\xi}^{\mathrm{T}} \int_A \nu E_1 n^2 \ddot{\boldsymbol{\psi}}_n^{\mathrm{T}} \boldsymbol{\psi}_n dA \boldsymbol{\xi}'' dz, \tag{2.7e}$$

$$U_5 = \frac{1}{2}\int_z \boldsymbol{\xi}''^{\mathrm{T}} \int_A E_1 n^2 \boldsymbol{\psi}_n^{\mathrm{T}} \boldsymbol{\psi}_n dA \boldsymbol{\xi}'' dz, \tag{2.7f}$$

and the external work is

$$\Omega = -\int_z \int_A \left(f_n \boldsymbol{\psi}_n + f_s \boldsymbol{\psi}_s + f_z \boldsymbol{\psi}_z \right) dA \boldsymbol{\xi} dz. \tag{2.8}$$

In Eq. (2.8), the body forces are assumed constant in the thickness direction.

Based on the principle of minimum total potential energy, the matrix forms of the governing equations and boundary conditions can be found by taking the first variation of the total potential energy and setting it to zero:

$$\mathbf{C}_1 \boldsymbol{\xi} + \mathbf{C}_2 \boldsymbol{\xi}' + \mathbf{C}_3 \boldsymbol{\xi}'' + \mathbf{C}_4 \boldsymbol{\xi}'''' = \mathbf{F}, \tag{2.9a}$$

where coefficient matrices and force vector are given as

$$\mathbf{C}_1 = \int_A \left[E_1 \left(\dot{\boldsymbol{\psi}}_s^{\mathrm{T}} \dot{\boldsymbol{\psi}}_s + n^2 \ddot{\boldsymbol{\psi}}_n^{\mathrm{T}} \ddot{\boldsymbol{\psi}}_n \right) + G \dot{\boldsymbol{\psi}}_z^{\mathrm{T}} \dot{\boldsymbol{\psi}}_z \right] dA, \tag{2.9b}$$

$$\mathbf{C}_2 = \int_A \left[\nu E_1 \left(\dot{\boldsymbol{\psi}}_s^{\mathrm{T}} \boldsymbol{\psi}_z - \boldsymbol{\psi}_z^{\mathrm{T}} \dot{\boldsymbol{\psi}}_s \right) + G \left(\dot{\boldsymbol{\psi}}_z^{\mathrm{T}} \boldsymbol{\psi}_s - \boldsymbol{\psi}_s^{\mathrm{T}} \dot{\boldsymbol{\psi}}_z \right) \right] dA, \tag{2.9c}$$

$$\mathbf{C}_3 = -\int_A \left[E_1 \boldsymbol{\psi}_z^{\mathrm{T}} \boldsymbol{\psi}_z + G\left(\boldsymbol{\psi}_s^{\mathrm{T}} \boldsymbol{\psi}_s + 4n^2 \dot{\boldsymbol{\psi}}_n^{\mathrm{T}} \dot{\boldsymbol{\psi}}_n \right) \right] dA \\ + \int_A \nu E_1 n^2 \left(\ddot{\boldsymbol{\psi}}_n^{\mathrm{T}} \boldsymbol{\psi}_n + \boldsymbol{\psi}_n^{\mathrm{T}} \ddot{\boldsymbol{\psi}}_n \right) dA, \tag{2.9d}$$

$$\mathbf{C}_4 = \int_A E_1 n^2 \boldsymbol{\psi}_n^{\mathrm{T}} \boldsymbol{\psi}_n dA, \tag{2.9e}$$

$$\mathbf{F} = \int_A \left(f_n \boldsymbol{\psi}_n^{\mathrm{T}} + f_s \boldsymbol{\psi}_s^{\mathrm{T}} + f_z \boldsymbol{\psi}_z^{\mathrm{T}} \right) dA. \tag{2.9f}$$

The generalized forces are obtained as stress resultants from the boundary terms:

$$\begin{aligned} \mathbf{R} &= \int_A \left(\boldsymbol{\psi}_z^{\mathrm{T}} \sigma_{zz} + \boldsymbol{\psi}_s^{\mathrm{T}} \sigma_{zs} \right) dA \\ &= \int_A \left(\nu E_1 \boldsymbol{\psi}_z^{\mathrm{T}} \dot{\boldsymbol{\psi}}_s + G \boldsymbol{\psi}_s^{\mathrm{T}} \dot{\boldsymbol{\psi}}_z \right) dA \boldsymbol{\xi} \\ &\quad + \int_A \left[E_1 \boldsymbol{\psi}_z^{\mathrm{T}} \boldsymbol{\psi}_z + G\left(\boldsymbol{\psi}_s^{\mathrm{T}} \boldsymbol{\psi}_s + 4n^2 \dot{\boldsymbol{\psi}}_n^{\mathrm{T}} \dot{\boldsymbol{\psi}}_n \right) \right] dA \boldsymbol{\xi}' \\ &\quad - \int_A \nu E_1 n^2 \boldsymbol{\psi}_n^{\mathrm{T}} \ddot{\boldsymbol{\psi}}_n dA \boldsymbol{\xi}' - \int_A E_1 n^2 \boldsymbol{\psi}_n^{\mathrm{T}} \boldsymbol{\psi}_n dA \boldsymbol{\xi}''', \end{aligned} \tag{2.10}$$

2.2 Generalized forces

The generalized forces in Eq. (2.10) can be mode-wisely written for an in-plane mode and an out-of-plane mode as

$$F_i = \int_A \sigma_{zs} \psi_s^{\xi_i} dA, \tag{2.11a}$$

$$F_j = \int_A \sigma_{zz} \psi_z^{\xi_j} dA, \tag{2.11b}$$

where subindices i and j denote in-plane modes and out-of-plane modes, respectively.

If cross-section modes are defined orthogonal each other as $\int_A \psi_k^p \psi_k^q dA = 0$, ($k$=$s$, z) for $p \neq q$, the generalized force in Eqs. (2.11) can be expressed in terms of the shape function of its corresponding mode only, from which generalized forces can be decoupled in the stress expressions. The derivation of orthogonal cross-section modes will be discussed in Chapter 3.

To derive the explicit generalized force-stress relation for an in-plane mode, the shear stress acting on the midline is considered. Using Eqs. (2.1) and (2.3-2.5), the stress is

$$\sigma_{zs} = G\gamma_{zs} = G\left(\frac{\partial u_s}{\partial z} + \frac{\partial u_z}{\partial s}\right) = G\left(\sum_i \psi_s^{\xi_i} \xi_i' + \sum_j \dot{\psi}_z^{\xi_j} \xi_j\right). \tag{2.12}$$

Because $\dot{\psi}_z^{\xi_j} = \sum_i c_{j,i} \psi_s^{\xi_i}$ ($c_{j,i}$: coefficient; this will be proved in Sections 4 and 5), Eq. (2.12) can be rewritten as

$$\sigma_{zs} = \sum_i S_i \psi_s^{\xi_i}, \tag{2.13}$$

where the coefficient S_i consists of $c_{j,i}$, material properties, ξ_j and ξ_i'. Substituting Eq. (2.13) into Eq. (2.11a) and using the orthogonality among in-plane modes, the generalized force is obtained as

$$F_i = S_i \lambda_i, \tag{2.14}$$

where $\lambda_i = \int_A (\psi_s^{\xi_i})^2 dA$ (A: cross-section area) is the sectional moment of inertia for ξ_i. Note that the terms for modes other than ξ_i are dropped due to the orthogonality. Using Eq. (2.14), the stress in Eq. (2.13) can be expressed in terms of the generalized forces:

$$\sigma_{zs} = \sum_i \frac{F_i}{\lambda_i} \psi_s^{\xi_i}. \tag{2.15}$$

Similarly, the generalized force-stress relation for an out-of-plane mode can be obtained as

$$\sigma_{zz} = \sum_j \frac{F_j}{\lambda_j} \psi_z^{\xi_j}, \tag{2.16}$$

and the relation between wall-bending stress and generalized forces is

$$\bar{\sigma}_{zz} = -n \left(\sum_k \frac{\bar{F}_k}{\bar{\lambda}_k} \psi_n^{\eta_k} + \sum_i \frac{\bar{F}_i}{\bar{\lambda}_i} \psi_n^{\xi_i} \right), \tag{2.17}$$

where $\bar{\sigma}_{zz}$ and $\bar{F}_k$ are the wall-bending stress and the generalized force of wall-bending mode η_k, respectively.

Note that the relations between stresses and generalized forces in Eqs. (2.15-2.17) are valid only if the modes are defined orthogonal with respect to each other. Although effective relations of stresses and generalized forces can also be found in other studies such as Genoese et al. [19], those in Eqs. (2.15-2.17) are expressed explicitly for each cross-section mode. This is meaningful because the stress at a point can be decomposed into those by corresponding generalized forces. In other words, the contribution of each generalized force to the stress can be analyzed due to the decoupled generalized force-stress relations. This will be shown in the case studies of Section 3.3. In addition, the generalized force-stress relations can be employed to solve a jointed beam problem, where the transfer mechanism of generalized forces at a beam joint can be derived from the equilibrium of the resultants on cross-section edges [37].

2.3 Finite element formulation

The three-dimensional displacements in Eq. (2.3) are discretized as

$$\tilde{\mathbf{u}} = \begin{Bmatrix} \tilde{u}_n \\ \tilde{u}_s \\ \tilde{u}_z \end{Bmatrix} = \begin{bmatrix} 1 & 0 & 0 \\ -n\frac{\partial}{\partial s} & 1 & 0 \\ -n\frac{\partial}{\partial z} & 0 & 1 \end{bmatrix} \begin{Bmatrix} u_n \\ u_s \\ u_z \end{Bmatrix} = \mathbf{A}(n)\boldsymbol{\psi}(s)\mathbf{N}(z)\mathbf{d}, \tag{2.18}$$

where $\mathbf{A}$ is the matrix mapping displacements on the midline of an edge to those at a generic point on the cross-section, $\boldsymbol{\psi}$ is the matrix consisting of ψ's, $\mathbf{N}$ is the shape function matrix, and $\mathbf{d}$ is the nodal solution vector of $\boldsymbol{\xi}$. The Hermite cubic polynomials are employed for shape functions in $\mathbf{N}$:

$$\mathbf{N}(\kappa) = \left[N_1(\kappa)\mathbf{I} \quad N_2(\kappa)\mathbf{I} \quad N_3(\kappa)\mathbf{I} \quad N_4(\kappa)\mathbf{I} \right], \tag{2.19}$$

where

$$\begin{aligned} N_1(\kappa) &= \frac{1}{4}(\kappa^3 - 3\kappa + 2), \\ N_2(\kappa) &= \frac{1}{4}(\kappa^3 - \kappa^2 - \kappa + 1), \\ N_3(\kappa) &= \frac{1}{4}(-\kappa^3 + 3\kappa + 2), \\ N_4(\kappa) &= \frac{1}{4}(\kappa^3 + \kappa^2 - \kappa - 1), \end{aligned} \tag{2.20}$$

where $\mathbf{I}$ is an identity matrix with the size N_D, and κ is the natural coordinate of an element. Note that the second derivative terms in Eq. (2.4b) can be conserved by using the Hermite cubic polynomials, whose effect can be noticeable on the accuracy of problems with dominant wall-bending deformations.

The strains and stresses in Eqs. (2.4) and (2.5) can be written in matrix form as

$$\tilde{\boldsymbol{\varepsilon}}=\begin{Bmatrix}\tilde{\varepsilon}_{ss}\\ \tilde{\varepsilon}_{zz}\\ \tilde{\gamma}_{zs}\end{Bmatrix}=\begin{bmatrix}0 & \partial/\partial s & 0\\ 0 & 0 & \partial/\partial z\\ 0 & \partial/\partial z & \partial/\partial s\end{bmatrix}\begin{Bmatrix}\tilde{u}_n\\ \tilde{u}_s\\ \tilde{u}_z\end{Bmatrix}=\mathbf{LA}(n)\boldsymbol{\psi}(s)\mathbf{N}(z)\mathbf{d}, \qquad (2.21)$$

$$\tilde{\boldsymbol{\sigma}}=\begin{Bmatrix}\tilde{\sigma}_{ss}\\ \tilde{\sigma}_{zz}\\ \tilde{\sigma}_{zs}\end{Bmatrix}=\begin{bmatrix}E_1 & \nu E_1 & 0\\ \nu E_1 & E_1 & 0\\ 0 & 0 & G\end{bmatrix}\begin{Bmatrix}\tilde{\varepsilon}_{ss}\\ \tilde{\varepsilon}_{zz}\\ \tilde{\gamma}_{zs}\end{Bmatrix}=\mathbf{CLA}(n)\boldsymbol{\psi}(s)\mathbf{N}(z)\mathbf{d}, \qquad (2.22)$$

where $\mathbf{L}$ represents the operator matrix, and $\mathbf{C}$ is the elasticity matrix. The total potential energy of a beam can be written as

$$\begin{aligned}\Pi &= \frac{1}{2}\int_z\int_A \tilde{\boldsymbol{\sigma}}^{\mathrm{T}}\tilde{\boldsymbol{\varepsilon}}\, dAdz+\rho\int_z\int_A \tilde{\mathbf{u}}^{\mathrm{T}}\tilde{\mathbf{u}}_{,tt}dAdz-\int_z\int_A \tilde{\mathbf{u}}^{\mathrm{T}}\mathbf{f}dAdz\\ &=\frac{1}{2}\mathbf{d}^{\mathrm{T}}\mathbf{Kd}+\mathbf{d}^{\mathrm{T}}\mathbf{Md}_{,tt}-\mathbf{d}^{\mathrm{T}}\mathbf{F},\end{aligned} \qquad (2.23)$$

where $(\ )_{,tt}$ is the second derivative with respect to time, ρ is the density, $\mathbf{f}$ is the body force vector, and $\mathbf{K}$, $\mathbf{M}$ and $\mathbf{F}$ are the stiffness matrix, mass matrix and force vector, respectively. By minimizing the total potential energy, the discretized dynamic equation can be derived. Substituting Eqs. (2.19-23) into Eq. (2.24) gives the stiffness matrix, mass matrix and force vector as

$$\mathbf{K}=\int_z \mathbf{N}^{\mathrm{T}}\mathbf{SN}dz, \qquad (2.24)$$

$$\mathbf{M}=\rho\int_z \mathbf{N}^{\mathrm{T}}\mathbf{TN}dz, \qquad (2.25)$$

$$\mathbf{F}=\int_z \mathbf{N}^{\mathrm{T}}\mathbf{R}dz, \qquad (2.26)$$

where

$$\mathbf{S}=\int_A \boldsymbol{\psi}^{\mathrm{T}}\mathbf{A}^{\mathrm{T}}\mathbf{L}^{\mathrm{T}}\mathbf{CLA}\boldsymbol{\psi}dA, \qquad (2.27)$$

$$\mathbf{T} = \int_A \boldsymbol{\psi}^{\mathrm{T}} \mathbf{A}^{\mathrm{T}} \mathbf{A} \boldsymbol{\psi} \, dA, \tag{2.28}$$

$$\mathbf{R} = \int_A \boldsymbol{\psi}^{\mathrm{T}} \mathbf{A}^{\mathrm{T}} \mathbf{f} \, dA. \tag{2.29}$$

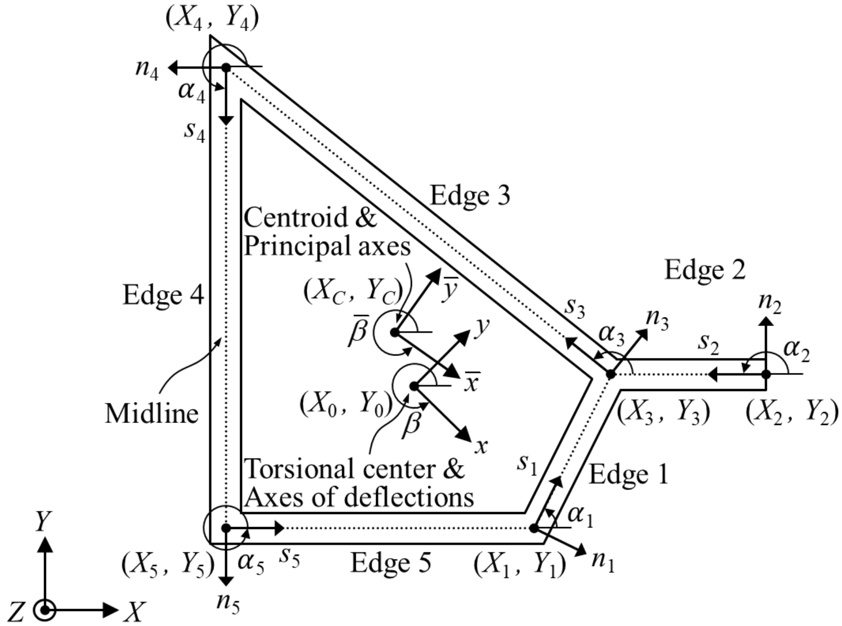

Fig. 2.1 The geometry of a thin-walled cross-section, and local and global coordinates

CHAPTER 3.
Derivation of cross-section modes for thin-walled beams with arbitrary sections

3.1 Prerequisites and lower-order modes

The shape functions of the proposed cross-section modes are derived based on following assumptions:

Assumption 1: Linear warping and inextensional distortion modes are induced by shear stress aroused by generalized forces of in-plane rigid-body modes.

Assumption 2: Extensional distortion and wall-bending modes are induced by the Poisson's effect for the axial stress σ_{zz} (or $\bar{\sigma}_{zz}$) (see Figs. 3.1(a) and (b)). Therefore, they are generated as the next higher-order modes of the corresponding out-of-plane deformation modes [38, 39].

Assumption 3: Nonlinear warping modes are aroused by the shear stress σ_{zs} (see Fig. 3.1(c)). They are derived to satisfy field consistency in the shear stress for the given in-plane deformation modes [38].

Lower-order modes, including linear warping modes and inextensional distortion modes, are presented in this chapter. Extensional distortion modes, wall-bending modes and nonlinear warping modes will be derived in the next chapter, for which the generalized force-stress relations obtained in Section 2.2 are used to derive the differential relations among the shape functions.

3.1.1 In-plane rigid-body modes

Shape functions $\psi_{k(e)}^{\mu}$ ($\mu = U_x$, U_y, θ_z; $k = n$, s) representing in-plane rigid-body modes are defined for each edge e in terms of the (x, y) coordinates (see Fig. 2.1) as

$$\psi_{s(e)}^{U_x} = \cos(\alpha_e - \beta); \ \psi_{n(e)}^{U_x} = \sin(\alpha_e - \beta), \tag{3.1}$$

$$\psi_{s(e)}^{U_y} = \sin(\alpha_e - \beta); \ \psi_{n(e)}^{U_y} = -\cos(\alpha_e - \beta), \tag{3.2}$$

$$\psi_{s(e)}^{\theta_z} = (X_e - X_0)\sin\alpha_e - (Y_e - Y_0)\cos\alpha_e, \tag{3.3a}$$

$$\psi_{n(e)}^{\theta_z} = -(X_e - X_0)\cos\alpha_e - (Y_e - Y_0)\sin\alpha_e - s_e, \tag{3.3b}$$

where (X_0, Y_0) and β are the origin and the orientation angle of the (x, y) coordinate system, respectively. Note that the center of torsional rotation θ_z is set at the origin of (x, y). Using the orthogonality between U_x and U_y, $\int_A \psi_s^{U_x}\psi_s^{U_y} dA = 0$, β can be determined as

$$\beta = \frac{1}{2}\tan^{-1}\left(\frac{\sum_{e=1}^{N_E} l_e \sin 2\alpha_e}{\sum_{e=1}^{N_E} l_e \cos 2\alpha_e} \right), \tag{3.4}$$

where l_e and α_e are the length and angle of edge e, respectively, and N_E is the number of the cross-section edges. Similarly, using $\int_A \psi_s^{U_x} \psi_s^{\theta_z} dA = 0$ and $\int_A \psi_s^{U_y} \psi_s^{\theta_z} dA = 0$, the origin of (x, y) is calculated as

$$\begin{Bmatrix} X_0 \\ Y_0 \end{Bmatrix} = \mathbf{A}_1^{-1} \mathbf{A}_2, \tag{3.5a}$$

where

$$\mathbf{A}_1 = \sum_{e=1}^{N_E} l_e \begin{bmatrix} \sin\alpha_e \sin(\alpha_e - \beta) & -\cos\alpha_e \sin(\alpha_e - \beta) \\ \sin\alpha_e \cos(\alpha_e - \beta) & -\cos\alpha_e \cos(\alpha_e - \beta) \end{bmatrix}, \tag{3.5b}$$

$$\mathbf{A}_2 = \sum_{e=1}^{N_E} l_e \begin{Bmatrix} X_e \sin\alpha_e \sin(\alpha_e - \beta) - Y_e \cos\alpha_e \sin(\alpha_e - \beta) \\ X_e \sin\alpha_e \cos(\alpha_e - \beta) - Y_e \cos\alpha_e \cos(\alpha_e - \beta) \end{Bmatrix}. \tag{3.5c}$$

3.1.2 Linear warping and inextensional distortion modes

Following in assumption 1, the linear warping and inextensional distortion modes are defined so that the shear strain caused by them can satisfy the field consistency requirement with shear stress aroused by the generalized forces of the in-plane rigid-body modes:

$$\frac{\sigma_{zs}(s,z)}{G} = \frac{\partial u_s^{\chi^*}(s,z)}{\partial z} + \frac{\partial u_z^{W^*}(s,z)}{\partial s} = \psi_s^{\chi^*}(s)\chi^{*\prime}(z) + \dot{\psi}_z^{W^*}(s)W^*(z), \tag{3.6}$$

where $u_s^{\chi^*}$ is the s-directional displacement by the inextensional distortion χ^* and $u_z^{W^*}$ is the z-directional displacement by linear warping W^*. Using the generalized force-stress relation in Eq. (2.15), the shear stress in Eq. (3.6) can be written as

$$\sigma_{zs}(s,z)=\sum_{\mu}\frac{F_{\mu}(z)}{\lambda_{\mu}}\psi_s^{\mu}(s), \tag{3.7}$$

where $\mu = U_x$, U_y, θ_z. Substituting Eq. (3.7) into Eq. (3.6) gives

$$\dot{\psi}_z^{W^*}(s)=\sum_{\mu}\frac{F_{\mu}(z)}{G\lambda_{\mu}W^*(z)}\psi_s^{\mu}(s)-\frac{\chi^{*\prime}(z)}{W^*(z)}\psi_s^{\chi^*}(s). \tag{3.8}$$

In Eq. (3.8), the relation between the cross-section shape functions is obtained as

$$\dot{\psi}_z^{W^*}(s)=\sum_{\mu}c_{\mu}\psi_s^{\mu}(s)+\psi_s^{\chi^*}(s), \tag{3.9}$$

where c_{μ} is constant for a given z. Note that the coefficient for $\psi_s^{\chi^*}$ is set as unity because $\psi_s^{\chi^*}$ is freely scalable.

Because χ^* in Eq. (3.9) has inextensional wall deformation, its shape function for s-directional displacement is edgewise constant; the displacement is constant on each edge, which may differ from those on other edges. Therefore, $\psi_s^{\chi^*}$ in Eq. (3.9) can be rewritten by introducing an unknown constant of edge e, c_e^*, as

$$\dot{\psi}_z^{W^*}(s)=\sum_{\mu}c_{\mu}\psi_s^{\mu}(s)+\sum_{e=1}^{N_E}c_e^*\delta_e, \tag{3.10}$$

where δ_e=1 on edge e and δ_e=0 otherwise. Integrating Eq. (3.10) gives

$$\psi_z^{W^*}(s)=\sum_{\mu}c_{\mu}\Psi_s^{\mu}(s)+\sum_{e=1}^{N_E}c_e^*\delta_e s+\sum_{e=1}^{N_E}c_e\delta_e, \tag{3.11}$$

where Ψ_s^{μ} is the integrated function of ψ_s^{μ} excluding the integration constant. Note that δ_e is used again in Eq. (3.11) to express the edgewise integration constant c_e. In matrix form, Eq. (3.11) is

$$\psi_z^{W*} = \left\{ \mathbf{\Psi}_s^{\mu},\ \boldsymbol{\delta}s,\ \boldsymbol{\delta} \right\} \begin{Bmatrix} \mathbf{c}_{\mu} \\ \mathbf{c}^{*} \\ \mathbf{c}_e \end{Bmatrix} \triangleq \boldsymbol{\varphi}^{W*}\mathbf{c}, \tag{3.12}$$

where $\mathbf{\Psi}_s^{\mu} = \{\Psi_s^{U_x}, \Psi_s^{U_y}, \Psi_s^{\theta_z}\}$, $\boldsymbol{\delta} = \{\delta_1, \delta_2, \cdots, \delta_{N_E}\}$, $\mathbf{c}_{\mu} = \{c_{U_x}, c_{U_y}, c_{\theta_z}\}^{\mathrm{T}}$, $\mathbf{c}^{*} = \{c_1^{*}, c_2^{*} \cdots, c_{N_E}^{*}\}^{\mathrm{T}}$ and $\mathbf{c}_e = \{c_1, c_2, \cdots, c_{N_E}\}^{\mathrm{T}}$.

In Eq. (3.12), multiple linear warping modes can be obtained by determining **c** differently, which should be determined to satisfy the orthogonality among the linear warping modes. For two linear warping modes W_i^{*} and W_j^{*} , the orthogonality between the modes can be written as

$$\int_A \psi_z^{W_i^*} \psi_z^{W_j^*} \, dA = \lambda \delta_{ij}, \tag{3.13}$$

where λ is the sectional moment of inertia, and δ_{ij} is the Kronecker delta. Using Eq. (3.12), the orthogonality in Eq. (3.13) can be rewritten as

$$\mathbf{c}_i^{\mathrm{T}} \int_A (\boldsymbol{\varphi}^{W*})^{\mathrm{T}} \boldsymbol{\varphi}^{W*} dA \mathbf{c}_j = \mathbf{c}_i^{\mathrm{T}} \mathbf{P}^{W*} \mathbf{c}_j = \lambda \delta_{ij}. \tag{3.14}$$

Because $\mathbf{P}^{W*}$ is a symmetric matrix, Eq. (3.14) can be expressed as a typical eigenvalue problem:

$$\mathbf{P}^{W*}\mathbf{c} = \lambda \mathbf{c}. \tag{3.15}$$

The eigenvector **c** obtained by solving Eq. (3.15) is employed as the coefficient vector in Eq. (3.12). Therefore, multiple new linear warping modes are simultaneously obtained by solving the eigenvalue problem in Eq. (3.15).

Although orthogonality is not an essential requirement for higher-order modes, it is very important in that generalized forces can be decoupled in the stress expressions only if the cross-section modes are orthogonal to each other, as can be seen in Eq. (2.15-2.17). This decoupling is essential in this paper given that the proposed higher-order modes are considered as secondary deformations induced by sectional stresses whose distributions are expressed by decoupled generalized force-stress relations.

When solving the eigenvalue problem in Eq. (3.15), the constraint conditions for **c** should be imposed so that the linear warping modes can satisfy the orthogonality with existing out-of-plane modes and the displacement continuity at the cross-section corners.

The orthogonality between a linear warping mode and an existing out-of-plane mode can be written as

$$\int_A \psi_z^{U_z} \psi_z^{W*} dA = \int_A \psi_z^{U_z} \boldsymbol{\varphi}^{W*} dA \mathbf{c} \triangleq \mathbf{Q}^{W*} \mathbf{c} = 0. \tag{3.16}$$

Note that because the linear warping modes are the first derived warping modes, only the axial rigid-body mode U_z is considered for the orthogonality condition.

The displacement continuity at the cross-section corners can also be defined as a constraint condition for **c**. For example, for the cross-section in Fig. 2.1, the corner continuity is

$$\begin{bmatrix} \boldsymbol{\varphi}_{(1)}^{W*}(l_1) - \boldsymbol{\varphi}_{(2)}^{W*}(l_2) \\ \boldsymbol{\varphi}_{(1)}^{W*}(l_1) - \boldsymbol{\varphi}_{(3)}^{W*}(0) \\ \boldsymbol{\varphi}_{(3)}^{W*}(l_3) - \boldsymbol{\varphi}_{(4)}^{W*}(0) \\ \boldsymbol{\varphi}_{(4)}^{W*}(l_4) - \boldsymbol{\varphi}_{(5)}^{W*}(0) \\ \boldsymbol{\varphi}_{(5)}^{W*}(l_5) - \boldsymbol{\varphi}_{(1)}^{W*}(0) \end{bmatrix} \mathbf{c} = \mathbf{R}^{W*} \mathbf{c} = 0, \tag{3.17}$$

where $\boldsymbol{\varphi}^{W*}(s)=\boldsymbol{\varphi}^{W*}_{(e)}(s_e)$ for edge e.

In addition to the conditions for the linear warping modes, those for the inextensional distortion modes should also be considered. Because the shape function of an inextensional distortion mode can be written as $\psi_s^{\chi^*}=\boldsymbol{\delta}\mathbf{c}^*$ according to Eqs. (3.9-3.12), where $\mathbf{c}^*$ is included in $\mathbf{c}$, the conditions for the inextensional distortion modes can be dealt with as the constraint condition of the eigenvalue problem in Eq. (3.15).

The orthogonality between an inextensional distortion modes and other existing in-plane modes can be written as

$$\int_A \{\psi_s^{\mu}\}\psi_s^{\chi^*}dA=\int_A \{\psi_s^{\mu}\}\boldsymbol{\delta}dA\mathbf{c}^* \triangleq \mathbf{Q}^{\chi^*}\mathbf{c}^*=0, \tag{3.18}$$

where $\{\psi_s^{\mu}\}=\{\psi_s^{U_x},\psi_s^{U_y},\psi_s^{\theta_z}\}^{\mathrm{T}}$. Note in Eq. (3.18) that the in-plane modes defined earlier than inextensional distortion modes are only in-plane rigid body modes.

The displacement continuity at the cross-section corners can be defined similarly to that of a linear warping mode in Eq. (3.17):

$$\mathbf{R}^{\chi^*}\mathbf{c}^*=0, \tag{3.19}$$

where $\mathbf{R}^{\chi^*}$ is given in Appendix B for a cross-section corner. The conditions in Eqs. (3.16-3.19) are set as constraint matrices for the eigenvalue problem of Eq. (3.15), which are treated, for example, using Lagrange multipliers. After defining the s-directional shape functions of the inextensional distortion modes, corresponding n-directional shape functions are calculated such that the conditions of displacement continuity, slope continuity and moment equilibrium at the corners are met [36, 39] (See Appendix C for details).

Note that rigid-body bending rotations $\theta_{\bar{x}}$ and $\theta_{\bar{y}}$ are also obtained from the results of the eigenvalue problem in Eq. (3.15). Moreover, the axes of these bending rotation modes coincide with the principal axes $(\bar{x},\bar{y})$ (see Fig. 2.1) owing to the orthogonality between the bending rotation modes. The torsional rotation mode is orthogonal to the x- and y-directional translations (bending deflections), from which the center of torsional rotation is determined, as expressed by Eqs. (3.5). However, the center of torsional rotation differs from the shear center. The linear warping modes of the proposed formulation are found to be identical to those by the GBT [12-17]. This is, however, not the case for nonlinear warping modes in higher sets. In addition, because the zero-shear stress condition on the midline of edges (or Vlasov condition) is not adopted in the proposed beam theory, warping modes and in-plane modes are not directly coupled.

3.2 Recursive derivation of higher-order modes

3.2.1 Extensional distortion and wall-bending modes

Following assumption 2, the extensional distortion modes are defined to express wall-extending/shrinking deformations caused by the Poisson effect when axial stress acts on the cross-section:

$$\frac{\partial u_s^{\chi}}{\partial s} = -\frac{\nu}{E}\sigma_{zz}, \tag{3.20}$$

which can be rewritten as

$$\chi(z)\dot{\psi}_s^{\chi}(s) = -\frac{\nu}{E}\left(\frac{F_{U_z}(z)}{\lambda_{U_z}}\psi_z^{U_z}(s) + \sum_{\hat{W}}\frac{F_{\hat{W}}(z)}{\lambda_{\hat{W}}}\psi_z^{\hat{W}}(s)\right), \tag{3.21}$$

where u_s^{χ} is the s-directional displacement by the extensional distortion mode χ and the $\hat{W}$ variables denote the warping modes in lower sets. Note that the axial stress is expressed in terms of generalized forces of existing out-of-plane modes using Eq. (2.16). For a given z, Eq. (3.21) can be rewritten as

$$\dot{\psi}_s^{\chi}(s) = c_{U_z}\psi_z^{U_z}(s) + \sum_{\hat{W}} c_{\hat{W}}\psi_z^{\hat{W}}(s), \tag{3.22}$$

where c_{U_z} and $c_{\hat{W}}$ are constants. Integrating Eq. (3.22) gives

$$\psi_s^{\chi}(s) = c_{U_z}\Psi_z^{U_z}(s) + \sum_{\hat{W}} c_{\hat{W}}\Psi_z^{\hat{W}}(s) + \sum_{e=1}^{N_E} c_e\delta_e, \tag{3.23}$$

whose matrix form is

$$\psi_s^\chi(s) = \left\{ \Psi_z^{U_z},\ \mathbf{\Psi}_z^{\hat{W}},\ \boldsymbol{\delta} \right\} \begin{Bmatrix} c_{U_z} \\ \mathbf{c}_{\hat{W}} \\ \mathbf{c}_e \end{Bmatrix} \triangleq \boldsymbol{\varphi}^\chi \mathbf{c}, \tag{3.24}$$

where $\mathbf{\Psi}_z^{\hat{W}} = \{\Psi_z^{\hat{W}}\}^{\mathrm{T}}$ and $\mathbf{c}_{\hat{W}} = \{c_{\hat{W}}\}$. As in the eigenvalue formulation of linear warping modes in Eqs. (3.13-3.15), considering the orthogonality among the extensional distortion modes gives

$$\mathbf{P}^\chi \mathbf{c} = \lambda \mathbf{c}, \tag{3.25}$$

where $\mathbf{P}^\chi = \int_A (\boldsymbol{\varphi}^\chi)^{\mathrm{T}} \boldsymbol{\varphi}^\chi dA$. The coefficients in Eq. (3.23) (or (3.24)) can be found by solving the eigenvalue problem with the constraints of orthogonality and corner continuity, akin to when the inextensional distortion modes were calculated. It should be noted that the constraint matrix for orthogonality should be constructed by considering distortions in lower sets as well as in-plane rigid-body modes.

As shown in Fig. 3.1(b), n-directional deformation is caused by the Poisson's effect when the bending stress acts on the cross-section. This relation can be written as

$$\frac{\partial \bar{u}_s}{\partial s} = -\frac{\nu}{E}\bar{\sigma}_{zz}, \tag{3.26}$$

where $\bar{u}_s$ is the s-directional displacement caused by the wall-bending mode, η:

$$\bar{u}_s = -n\frac{\partial u_n^\eta}{\partial s} = -n\eta(z)\dot{\psi}_n^\eta(s), \tag{3.27}$$

and the bending stress $\bar{\sigma}_{zz}$ can be written in terms of the generalized forces in Eq. (2.17) as

$$\bar{\sigma}_{zz} = -n\left(\sum_{\hat{\eta}} \frac{\bar{F}_{\hat{\eta}}(z)}{\bar{\lambda}_{\hat{\eta}}} \psi_n^{\hat{\eta}}(s) + \sum_{\hat{\chi}} \frac{\bar{F}_{\hat{\chi}}(z)}{\bar{\lambda}_{\hat{\chi}}} \psi_n^{\hat{\chi}}(s) + \sum_{\mu} \frac{\bar{F}_{\mu}(z)}{\bar{\lambda}_{\mu}} \psi_n^{\mu}(s)\right). \qquad (3.28)$$

In Eq. (3.28), $\hat{\eta}$ and $\hat{\chi}$ are wall-bending and distortion modes in lower sets, respectively. Substituting Eqs. (3.27, 3.28) into Eq. (3.26) gives

$$\ddot{\psi}_n^{\eta}(s) = \sum_{\hat{\eta}} c_{\hat{\eta}} \psi_n^{\hat{\eta}}(s) + \sum_{\hat{\chi}} c_{\hat{\chi}} \psi_n^{\hat{\chi}}(s) + \sum_{\mu} c_{\mu} \psi_n^{\mu}(s). \qquad (3.29)$$

By integrating Eq. (3.29), the shape function for a wall-bending mode is obtained as

$$\psi_n^{\eta}(s) = \sum_{\hat{\eta}} c_{\hat{\eta}} \bar{\Psi}_n^{\hat{\eta}}(s) + \sum_{\hat{\chi}} c_{\hat{\chi}} \bar{\Psi}_n^{\hat{\chi}}(s) + \sum_{\mu} c_{\mu} \bar{\Psi}_n^{\mu}(s) + \sum_{e=1}^{N_E} \left(c_{e,1}s + c_{e,0}\right)\delta_e, \qquad (3.30)$$

where $\bar{\Psi}_n^{\xi}$ $(\xi = \hat{\eta}, \hat{\chi}, \mu)$ is the double integrated function of ψ_n^{ξ} excluding integration constants. The n-directional shape functions must be defined so that they can satisfy the displacement continuity, slope continuity, and moment equilibrium at the corners [36, 39]. However, there are too few unknown integration constants in Eq. (3.30), two for each edge ($c_{e,0}$ and $c_{e,1}$), to satisfy all of these corner conditions. To resolve this, the last term in Eq. (3.30) is modified to cubic polynomials [39]:

$$\psi_n^{\eta}(s) = \sum_{\hat{\eta}} c_{\hat{\eta}} \bar{\Psi}_n^{\hat{\eta}}(s) + \sum_{\hat{\chi}} c_{\hat{\chi}} \bar{\Psi}_n^{\hat{\chi}}(s) + \sum_{\mu} c_{\mu} \bar{\Psi}_n^{\mu}(s) + \sum_{e=1}^{N_E} \sum_{p=0}^{3} c_{e,p} s^p \delta_e = \boldsymbol{\varphi}^{\eta}\mathbf{c}, \qquad (3.31)$$

from which the eigenvalue problem can be derived, as in Eqs. (3.13-3.15). Orthogonality between wall-bending modes in the new set and those in the lower sets, continuity conditions, and moment equilibrium at the cross-section corners should be imposed as constraints for the eigenvalue problem (see Appendix C).

3.2.2 Nonlinear warping modes

Once the extensional distortion modes are defined in a mode set, the distribution of the sectional shear stress is updated to include the newly defined modes following Eq. (2.15):

$$\sigma_{zs}(s,z)=\sum_{\mu}\frac{F_{\mu}(z)}{\lambda_{\mu}}\psi_s^{\mu}(s)+\sum_{\hat{\chi}}\frac{F_{\hat{\chi}}(z)}{\lambda_{\hat{\chi}}}\psi_s^{\hat{\chi}}(s). \tag{3.32}$$

The nonlinear warping modes are defined to express the secondary deformations in the constitutive equation for this updated shear stress:

$$\frac{\sigma_{zs}(s,z)}{G}=\frac{\partial u_s(s,z)}{\partial z}+\frac{\partial u_z^W(s,z)}{\partial s}, \tag{3.33}$$

where u_s is the s-directional displacement, and u_z^W is the z-directional displacement caused by the nonlinear warping mode W, as expressed by

$$u_s(s,z)=\sum_{\mu}\mu(z)\psi_s^{\mu}(s)+\hat{\chi}(z)\psi_s^{\hat{\chi}}(s), \tag{3.34}$$

$$u_z^W(s,z)=W(z)\psi_z^W(s). \tag{3.35}$$

Note that the s-directional displacement is expressed using existing in-plane modes because in this section, the focus is on defining deformable shapes in the z-direction.

Substituting Eqs. (3.32, 3.34, 3.35) into Eq. (3.33) gives

$$W(z)\dot{\psi}_z^W(s) = \sum_{\mu}\left(\frac{F_\mu(z)}{G\lambda_\mu} - \mu'(z)\right)\psi_s^\mu(s) + \sum_{\hat{\chi}}\left(\frac{F_{\hat{\chi}}(z)}{G\lambda_{\hat{\chi}}} - \hat{\chi}'(z)\right)\psi_s^{\hat{\chi}}(s), \quad (3.36)$$

which leads to

$$\dot{\psi}_z^W(s) = \sum_{\mu} c_\mu \psi_s^\mu(s) + \sum_{\hat{\chi}} c_{\hat{\chi}} \psi_s^{\hat{\chi}}(s), \quad (3.37)$$

where c_μ and $c_{\hat{\chi}}$ are constants for a given z. Integrating Eq. (3.37) gives

$$\psi_z^W(s) = \sum_{\mu} c_\mu \Psi_s^\mu(s) + \sum_{\hat{\chi}} c_{\hat{\chi}} \Psi_s^{\hat{\chi}}(s) + \sum_{e=1}^{N_E} c_e \delta_e = \boldsymbol{\varphi}^W \mathbf{c}. \quad (3.38)$$

Using the orthogonality among the warping modes in the current set, an eigenvalue problem similar to that in Eq. (3.15) can be defined. The constraint matrix consists of the continuity condition in Eq. (3.17) and the orthogonality condition, for which warping modes in lower sets as well as the axial rigid-body mode should be considered.

The derived warping modes in Eq. (3.38) update the axial stress in Eq. (3.20), inducing higher-order distortion modes. The proposed higher-order modes are derived by this recursive process. The number of mode sets employed for the analysis can be determined according to the required level of accuracy. Due to the integration form of the mode-derivation equations of Eqs. (3.23, 3.31, 3.38), the polynomial orders of shape functions for distortion and warping modes increase by one as the set number M increases (see Fig. 3.2), while those for wall-bending modes increase by two.

Referring to our previous works [38, 39] would be helpful to understand a step-by-step procedure for calculating cross-section modes. Although they present cross-section modes only for rectangular cross-sections, the overall procedure is similar except that those studies use the symmetry of a cross-section to calculate the coefficients of a shape function instead of conducting an eigenvalue analysis.

3.3 Numerical examples

The proposed HoBT is applied to derive cross-section modes for open, closed, and flanged cross-sections in Fig. 3.3. Figures 3.4-3.6 show the corresponding cross-section modes. In the figures, bending rotation modes $\theta_{\bar{x}}$ and $\theta_{\bar{y}}$ are listed as linear warping modes because they are derived by solving the eigenvalue problem for linear warping modes. Table 3.1 shows the number of cross-section modes for each mode set obtained by Eqs. (D.1-D.5) in Appendix D.

The derived cross-section modes are used to solve static or modal analysis problems of thin-walled beams. The results by the proposed HoBT are compared with those obtained by shell elements (ABAQUS S8R elements) and other beam-based approaches, for which the Timoshenko beam theory, the generalized beam theory (GBT) [12-17] and the method of generalized eigenvectors (GE) [18-23] are considered. For the material properties of the beams, Young's modulus is set as E = 210 GPa for the example in Section 3.3.2 and as E = 200 GPa for the other examples, and the Poisson's ratio and density are correspondingly set as ν = 0.3 and ρ = 7850 kg/m^3 for all examples.

3.3.1 Static analysis: a cantilever beam with an open cross-section

A static analysis is conducted for the thin-walled beam (length: 900 mm and thickness: 1 mm) with the open cross-section shown in Fig. 3.3(a). One end of the beam (z = 0) is fixed and the cross-section on the other end (z = 900 mm) is subjected to a set of distributed loads in the s- and z-directions, representing complex loading at the joint of a beam frame structure approximating a T-joint (see Fig. 3.3(a)). In total, 200 finite elements are used in the numerical analysis. To capture the rapidly changing end effect, 100 elements are assigned near the loaded end (from z=800 mm to z=900 mm).

For the analyses, various numbers of cross-section modes are used, in this case 26 modes, 44 modes, 65 modes and 161 modes, which correspond to the number of the modes for the highest mode set, M= 2, 3, 4 and 9, respectively. In the analyses, warping modes in the last set are not employed because they influence the solution accuracy less compared to those of the other modes in the same set. Figures 3.7(a) and (b) show three-dimensional displacements and stress results, respectively, measured on the axial line corresponding to point P in Fig. 3.3(a). In these figures, the numbers in parentheses indicate the number of cross-section modes used for the analysis. These figures also show that excellent accuracy can be obtained for three-dimensional displacements by the proposed HoBT only by using up to the second set of the cross-section shape functions. The stress results in Fig. 3.7(b), however, show that higher sets of modes are required for a correct estimation of the rapidly changing stress variation due to the end effect. The difference in the peak value of σ_{zz} in Fig. 3.7(b) between the result by the present HoBT and that of the shell elements is plotted in Fig. 3.8 with respect to the highest mode set number (and number of modes). In the figure, the use of M = 4 for the present HoBT yields stress only within 4% error with respect to the shell-based calculation. These numerical tests suggest that satisfactory results can be obtained with $M = 2$ for the displacement calculations and $M = 4$ for the stress calculations (within 4% errors). If $M \geq 9$ is used, the stress prediction can be accurate within 1% error relative to the shell results.

Figure 3.9 shows the overall contribution of the three dominant distortion modes to the shear stress (σ_{ZX}) in Fig. 3.7(b) calculated using the generalized force-stress relation in Eq. (2.15). Because the generalized forces are the work conjugates of one-dimensional deformations, element force vectors associated with the points of interest are used to calculate the stress curves in Fig. 3.9. Note in the figure that the three most influential distortion modes, χ_2, χ_3 and χ_{10}, show edge-extending/shrinking deformations, especially on both horizontal cross-section edges. These dominant modes can be restrained by rigidly connecting two corners on the bottom edge in Fig. 3.3(a) (or two points at s_2=0 and s_3=0). For verification, an additional numerical test is conducted, showing that the peak stress is reduced from 112.3Pa to 66.4Pa (40.9% reduction) when the suggested constraint is imposed.

Figure 3.10 shows the stress results measured on the inner surface ($n = -t/2$), outer surface ($n = t/2$), and midline at point P along the axial direction, which are perfectly matched with those obtained by the shell elements.

3.3.2 Static analysis: a simply supported beam with an open cross-section

The simply supported beam problem with an open cross-section subjected to a sinusoidal load in Fig. 3.11(a), as studied initially in earlier work [23], is analyzed by the proposed HoBT, the GBT and the GE methods. For the proposed beam analysis, cross-section modes of M=2 corresponding to the first 24 cross-section modes in Fig. 3.4 are used (although there is a slight difference in the dimension between the cross-sections in Fig. 3.3(a) and Fig. 3.11(a), the shapes of the modes for both cross-sections are found to be almost the same). For the GBT analysis, the modes are obtained using the program GBTUL [12-17] with cross-section discretization of three intermediate nodes for the web and two intermediate nodes for each flange. Among the 39 modes obtained, the first 15 modes, shown in Fig. E.1 in Appendix E, are utilized in the analysis. In total, 50 finite elements with even discretization are used for the GBT and the proposed approach. For the GE method, the result available in the aforementioned study [23], obtained using 19 in-plane modes and 19 out-of-plane modes, is used for comparison. In Fig. 3.11(b), the lateral displacements on the loading line obtained by the three methods show good agreement with the result by the shell elements.

Figure 3.12 shows the contribution of each mode to the total strain energy and the displacement at the middle point of the loading line. In Fig. 3.12, while the proposed modes that make large contributions to the strain energy are found to be identical to those by the GBT, the modes that make large contributions to the displacement are fewer than those by the GBT. This occurs because the point of the displacement measurement is in the middle of the beam, where only in-plane modes are aroused. Therefore, the out-of-plane modes corresponding to mode 3 and mode 5 of the GBT make zero contributions to the displacement in the figure on the right in Fig. 3.12. A similar aspect is also observed in the GE modes; a detailed report of this is given in the references [23].

3.3.3 Static analysis: a cantilever beam with a closed cross-section

The free end of a clamped thin-walled beam with the cross-section in Fig. 3.3(b) is under vertical concentrated force at the lower right corner of the cross-section. The beam length is 400 mm and the wall thickness is 2 mm. The displacement and stress results at point P along the axial direction calculated by the proposed HoBT as well as the GBT are plotted in Figs. 3.13(a) and (b), respectively. For the cross-section discretization of the GBT, three cases are studied; each edge is uniformly discretized with 1, 5 and 7 intermediate nodes, resulting in 78, 234 and 312 modes, respectively (see Fig. E.2 in Appendix E for the cross-section modes obtained using one intermediate node). Here, 200 finite elements in total are employed for the analysis of the GBT and the proposed HoBT, while 100 elements are assigned near the loaded end (from z=350 mm to z=400 mm).

In Fig. 3.13(a), moderate accuracy for the displacements can be obtained using M=2 (62 modes) in the proposed approach and 78 modes in the GBT, while more modes (M=5 or 213 modes in the proposed approach and 234 modes in the GBT) are required to capture the end effect of u_z. For an accurate prediction of the stress, as in Fig. 3.13(b), M=7 (311 modes) and 312 modes are needed for the proposed HoBT and GBT, respectively.

The contribution of the generalized forces to σ_{zz} in Fig. 3.13(b) is shown in Fig. 3.14, where W_3^* is calculated as the most dominant higher-order mode for the axial stress. Figures 3.15(a) and (b) show the von Mises stress and deformed shape on the cross-section midline calculated at z = 380 mm, where the peak of the shear stress σ_{ZY} occurs. In the figure, the results by the proposed approach and GBT are in good agreement with the shell results.

3.3.4 Modal analysis: a beam with a flanged cross-section with a free-free support condition

A modal analysis is conducted for a thin-walled beam with a flanged cross-section, as shown in Fig. 3.3(c), with no support condition. The beam length is 500 mm and the wall thickness is 1 mm. Figure 3.16 shows the free vibration mode shapes obtained using the shell elements, GBT and proposed HoBT, whose corresponding natural frequencies are listed in Table 3.2. Two intermediate nodes are placed for each cross-section edge to derive the GBT modes (see Fig. E.3 for the cross-section modes). For the proposed HoBT, 21 modes are used, with M=2. In total, 50 finite elements with even discretization are used for the analyses of the GBT and the proposed HoBT. Although relatively few cross-section modes are employed, the free vibration characteristics of the beam are accurately predicted by both approaches. Specifically, the proposed HoBT gives results with less than 1% of a difference relative to the shell results.

Table 3.1 The number of cross-section modes for the cross-sections in Fig. 3.3

	Open section				**Closed section**				**Flanged section**			
Set	N_χ	N_η	N_W	Total	N_χ	N_η	N_W	Total	N_χ	N_η	N_W	Total
1	2	0	5	11(7+4)	10	0	12	26(22+4)	1	0	3	8(4+4)
2	6	9	6	32	13	23	13	75	4	9	4	25
3	6	6	6	50	13	24	13	125	4	9	4	42
4	6	9	6	71	13	25	13	176	4	9	4	59
5	6	6	6	89	13	24	13	226	4	9	4	76
6	6	8	6	109	13	23	13	275	4	9	4	93
7	6	7	6	128	13	23	13	324	4	8	4	109
8	6	6	6	146	13	22	13	272	4	9	4	126
9	6	9	6	167	13	21	13	419	4	8	4	142

Table 3.2 Natural frequencies (Hz) of a beam with a flanged cross-section (numbers in parentheses denote the difference (%) from the shell results)

Mode	**1**	**2**	**3**	**4**	**5**	**6**	**7**
Shell	582.08	788.94	1482.1	1948.6	2098.0	2401.2	2850.9
GBT	583.97 (0.33)	791.56 (0.33)	1485.7 (0.24)	1953.1 (0.23)	2097.0 (0.05)	2398.5 (0.11)	2846.4 (0.16)
Proposed	583.35 (0.22)	790.53 (0.20)	1492.5 (0.71)	1961.1 (0.64)	2100.8 (0.13)	2424.1 (0.95)	2873.2 (0.78)

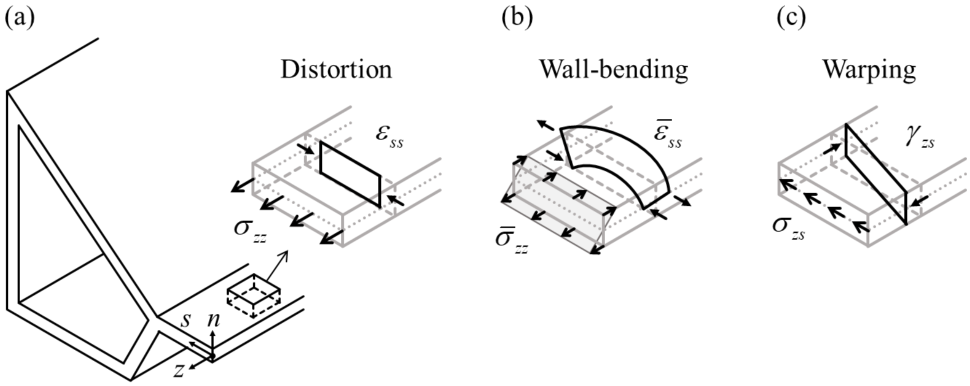

Fig. 3.1 Deformations by (a) axial stress, (b) bending stress and (c) shear stress acting on the sectional edge

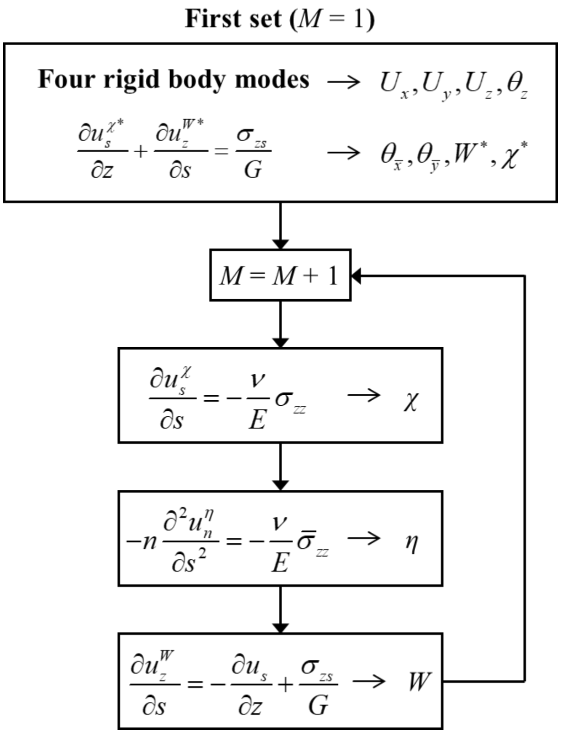

Fig. 3.2 Recursive process of the proposed higher-order mode derivation

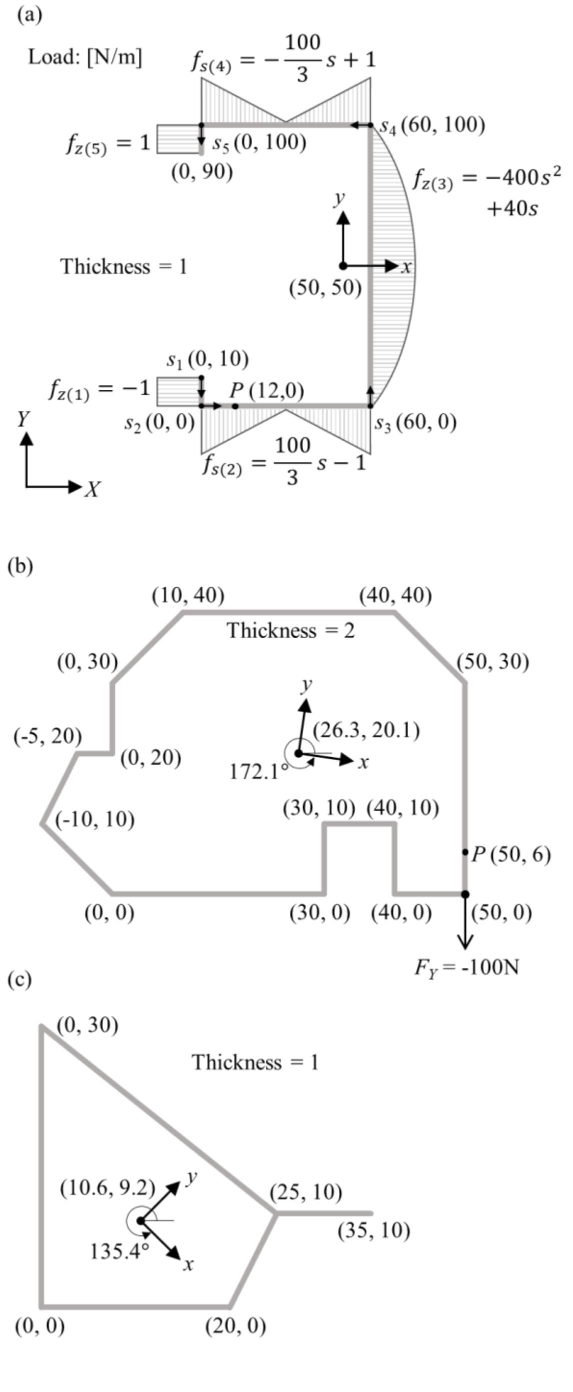

Fig. 3.3 Thin-walled cross-sections considered in the analyses: (a) an open section, (b) a closed section and (c) a flanged section

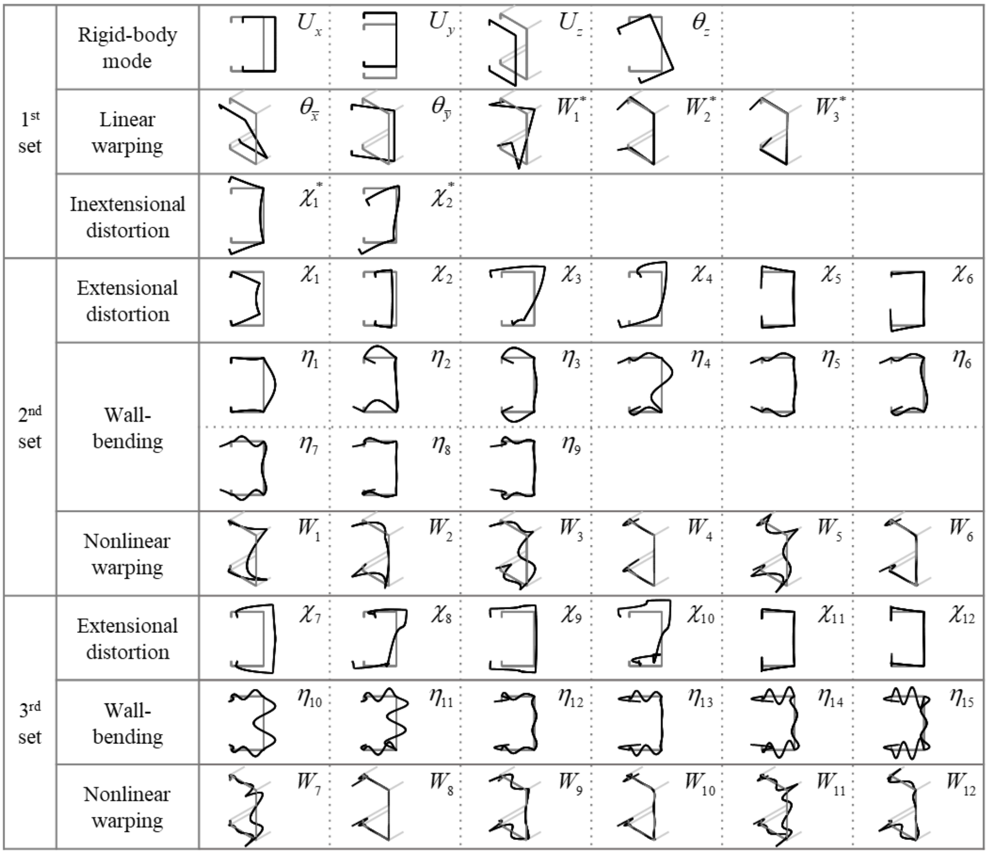

Fig. 3.4 Cross-section modes for the open section in Fig. 3.3(a)

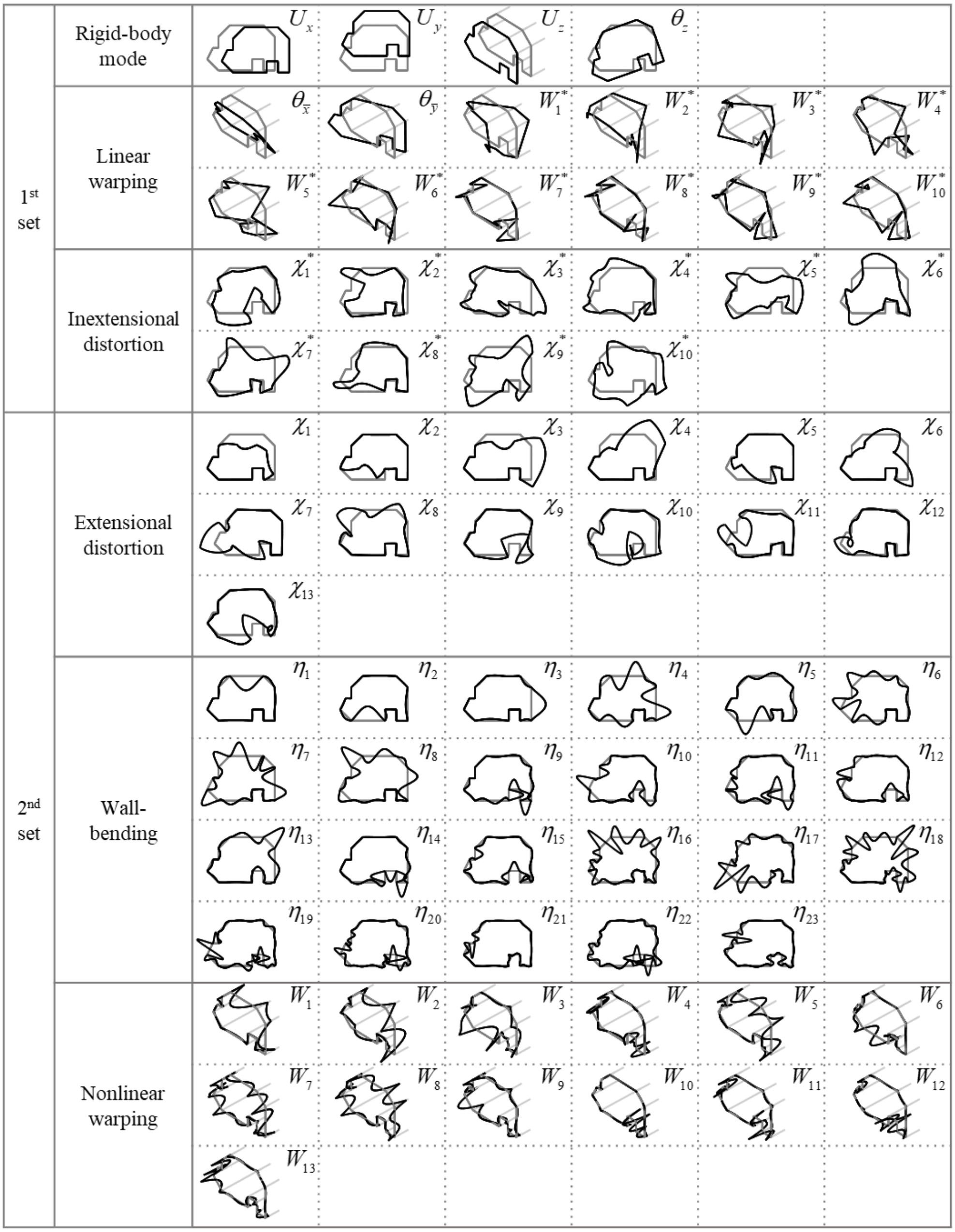

Fig. 3.5 Cross-section modes for the closed section in Fig. 3.3(b)

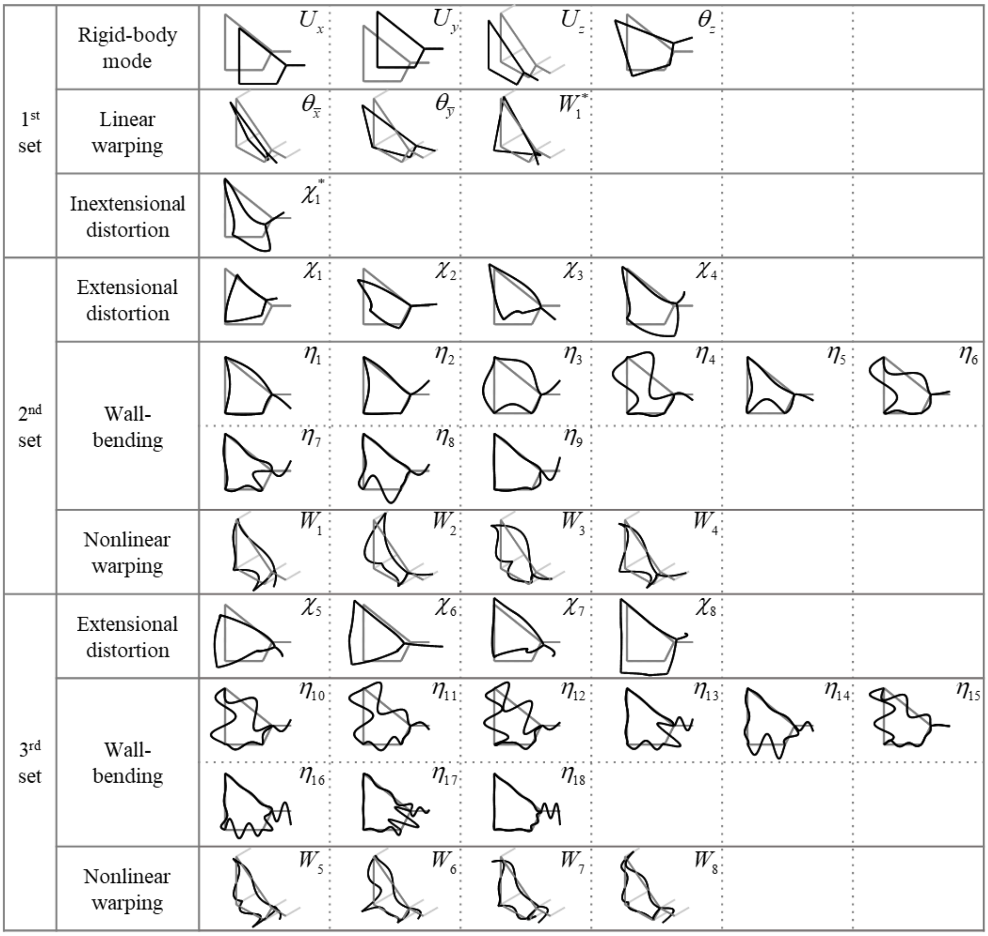

Fig. 3.6 Cross-section modes for the flanged section in Fig. 3.3(c)

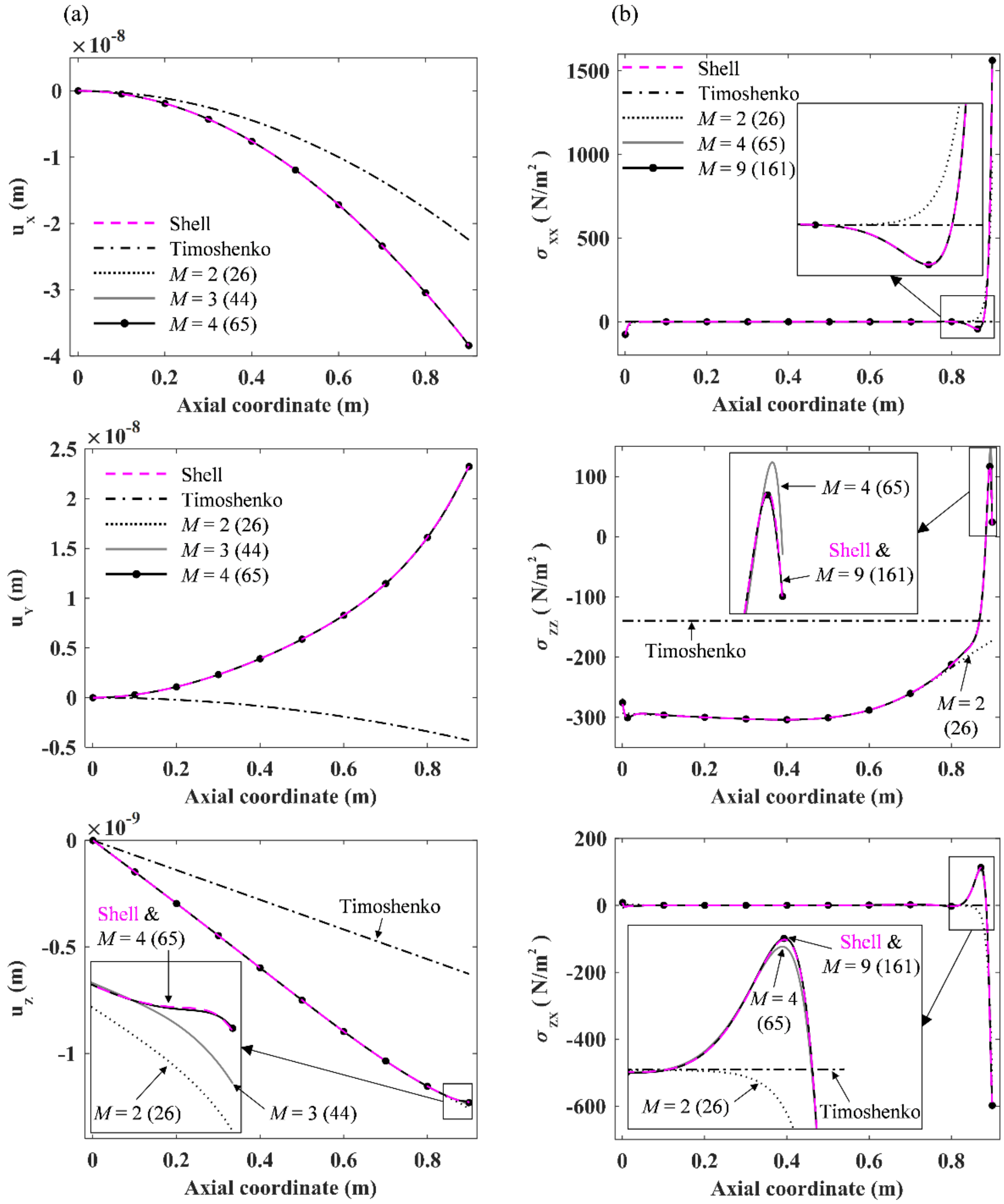

Fig. 3.7 Static analysis results measured along point P in Fig. 3.3(a): (a) displacement results and (b) stress results (the numbers in parentheses indicate the number of cross-section modes with M denoting the highest mode set number)

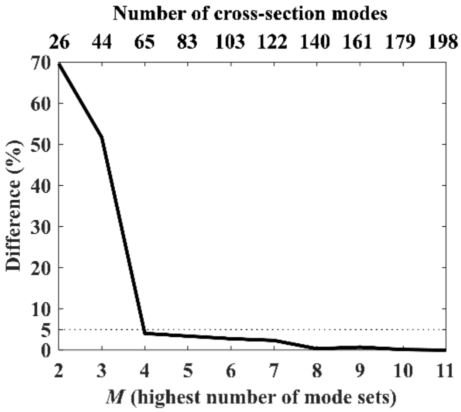

Fig. 3.8 Difference convergence of the axial stress (σ_{ZZ}) at the peak point (z = 893.4 mm) in Fig. 3.7(b) for varying numbers of mode sets

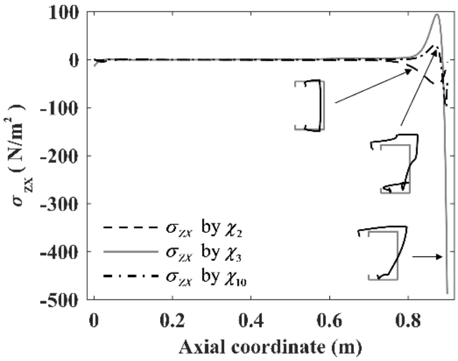

Fig. 3.9 Contribution of three dominant distortion modes to the shear stress (σ_{ZX}) in Fig. 3.7(b)

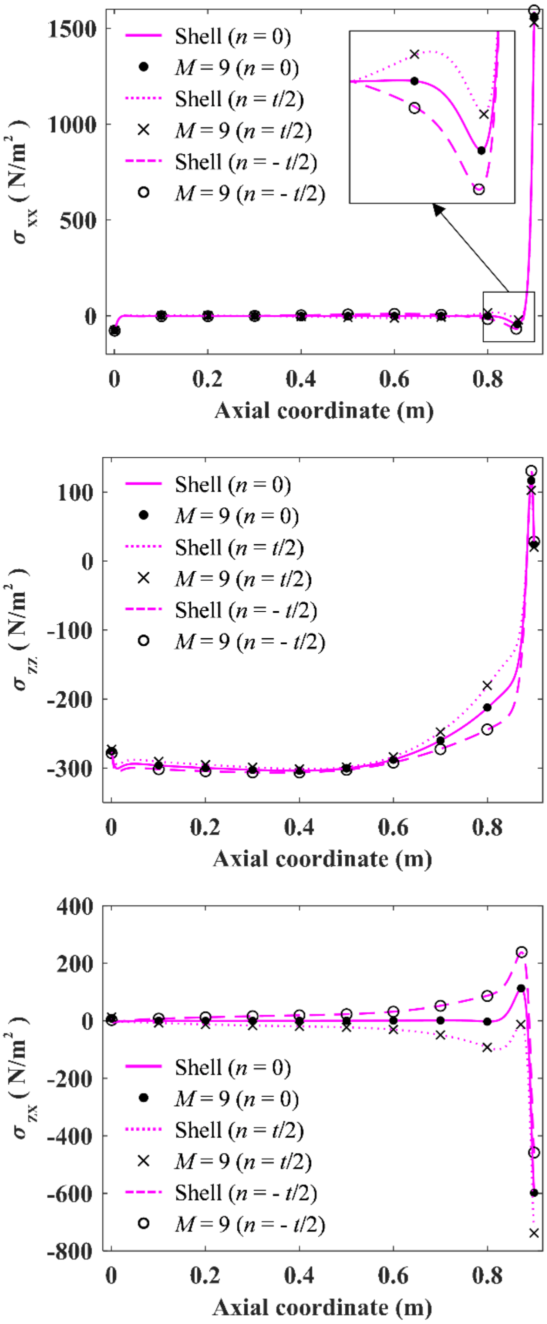

Fig. 3.10 Stress results measured at different n coordinates ($n = -t/2$, 0, $t/2$) of point P for the thin-walled beam problem with the open cross-section in Fig. 3.3(a)

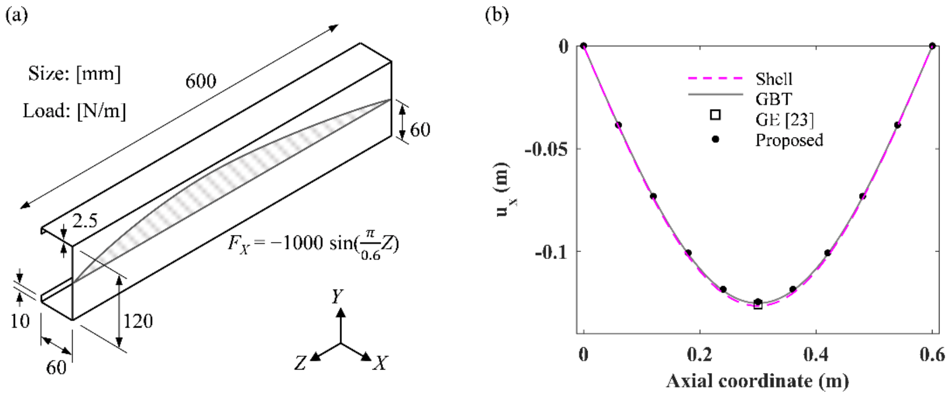

Fig. 3.11 (a) A simply supported thin-walled beam with an open cross-section subjected to a sinusoidal lateral load, and (b) resulting lateral displacements along the loading line

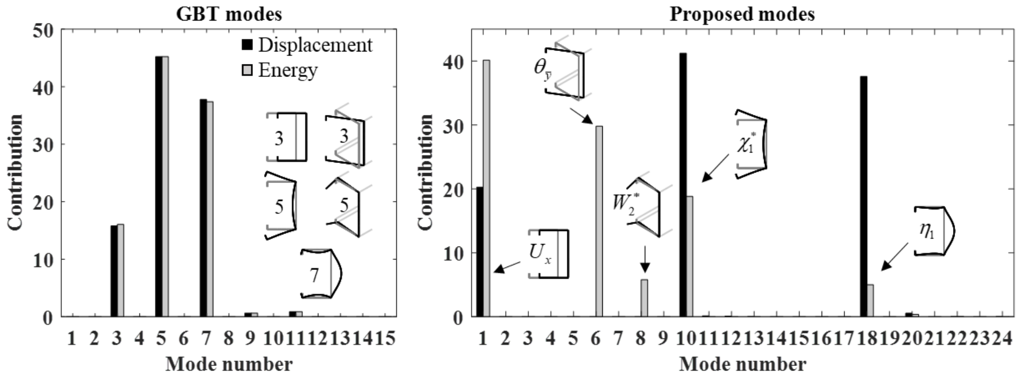

Fig. 3.12 Contributions to the strain energy and displacement at the center of the loading line by the GBT modes and proposed higher-order modes

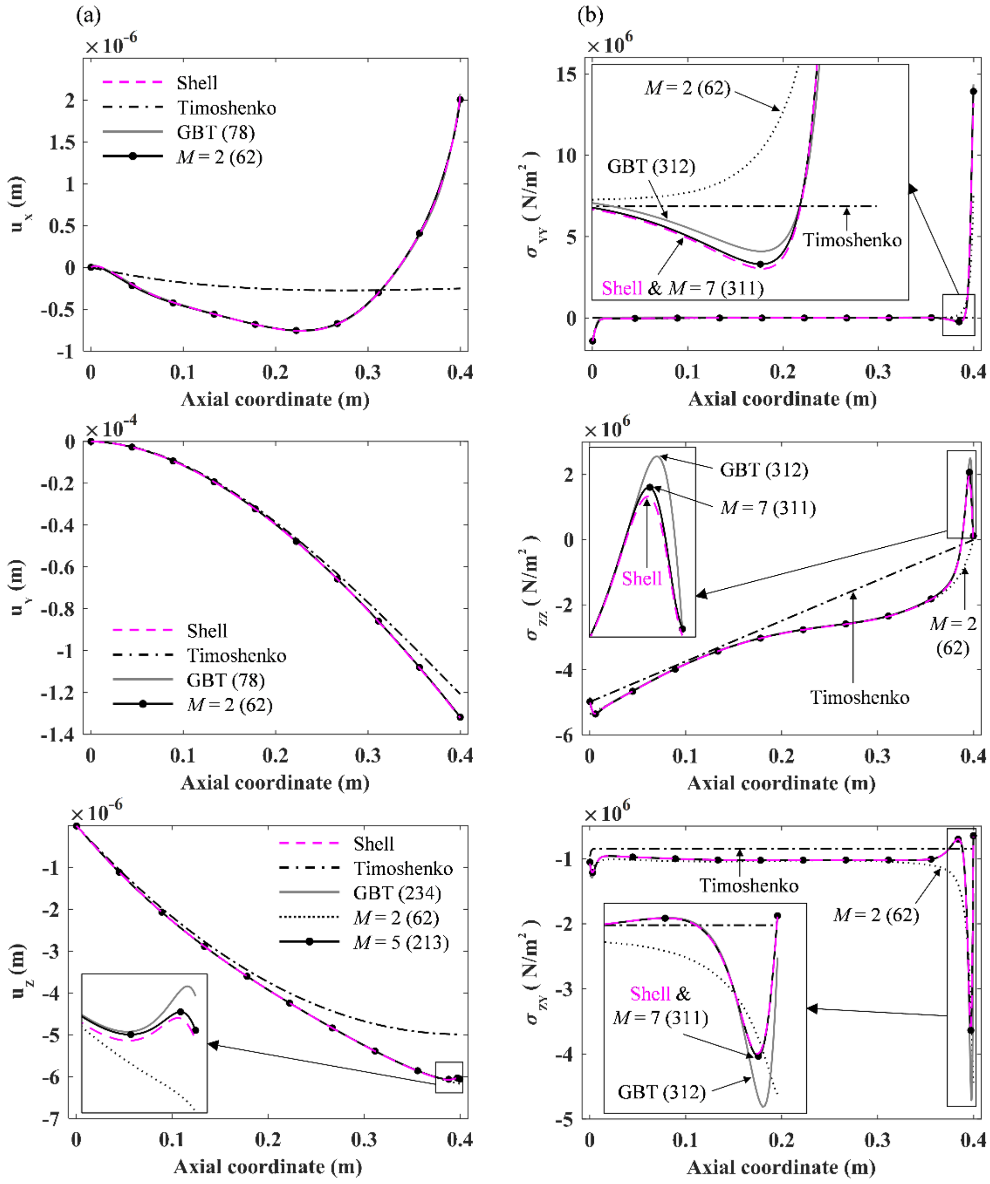

Fig. 3.13 Static analysis results measured along point P in Fig. 3.3(b): (a) displacement results and (b) stress results

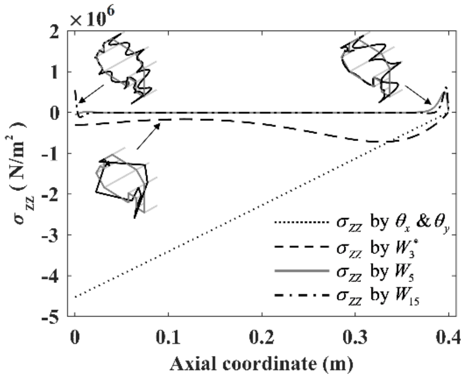

Fig. 3.14 Contribution of three dominant warping modes to the axial stress (σ_{ZZ}) in Fig. 3.13(b)

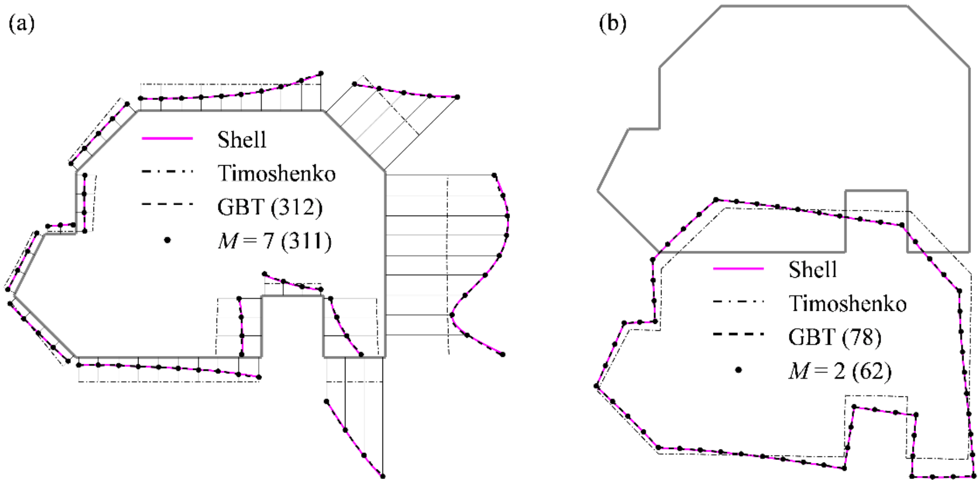

Fig. 3.15 (a) Von Mises stress and (b) in-plane deformation calculated on the cross-section at $z = 380$mm for the thin-walled beam problem with the cross-section in Fig. 3.3(b)

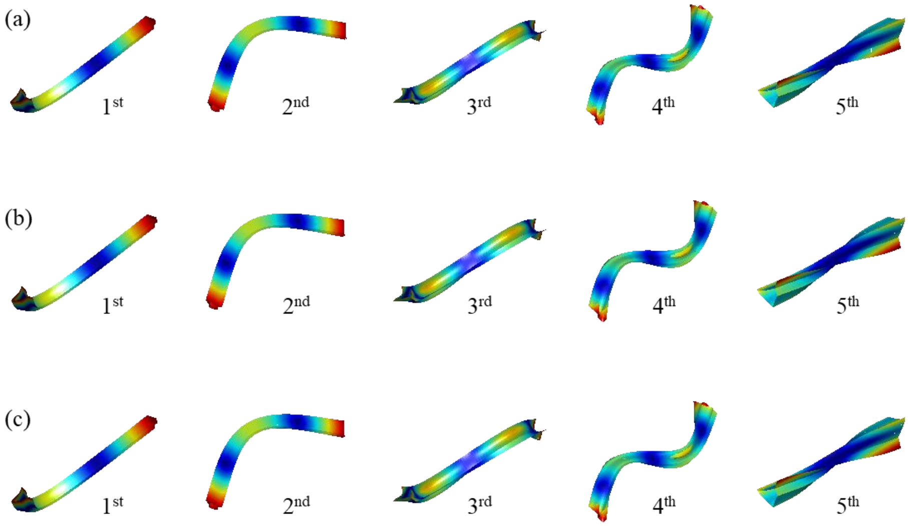

Fig. 3.16 Free-vibration mode shapes for a thin-walled beam with the flanged cross-section in Fig. 3.3(c): results by (a) the shell theory, (b) the GBT and (c) the proposed higher-order beam theory

CHAPTER 4.

Coupling relations of cross-section modes at a joint of thin-walled beam structures

4.1 Displacement and rotation continuities at a beam joint

A joint condition using displacement and rotation continuities is presented here. Figure 4.1 shows the connection points where the continuities are imposed. In the proposed approach, the connection points are placed at the cross-section corners and joint axis, while those in other approaches, e.g., the GBT [62-70], are designated inconsistently for the cross-section shape. Note that the joint axis intersects the centroid so that the mass can be correctly evaluated in the one-dimensional model. In Figs. 4.2(a, b) that show illustrative L- and T-type joints, it can be seen that connection points of each beam section do not meet directly since the beam section is normal to the beam axis. Because inaccurate results are yielded if this cross-sectional mismatch is neglected, as can be seen in other continuity-based approaches [57-61], displacements and rotations on the joint section where the connection points are actually matched have to be carefully assessed when the continuity conditions are calculated. To do this, we propose to take into account additional displacements on the joint section, which are aroused by rotations at the beam section, as can be seen in Fig. 4.2(c).

Note in Figs. 4.2(a, b) that the continuities are imposed at an end section of each beam of the L-type joint, while those of the T-type joint are imposed at an end section of one beam and several sections of the other beam.

In the Figs. 4.2(a, b), the vertical axis of each beam (Y_1 and Y_2) is set parallel to the joint axis, therefore, the relation between axes of two beams can be defined as

$$\begin{Bmatrix} X_1 \\ Y_1 \\ Z_1 \end{Bmatrix} = \begin{bmatrix} \cos\phi & 0 & \sin\phi \\ 0 & 1 & 0 \\ -\sin\phi & 0 & \cos\phi \end{bmatrix} \begin{Bmatrix} X_2 \\ Y_2 \\ Z_2 \end{Bmatrix} \triangleq \mathbf{T}_1 \begin{Bmatrix} X_2 \\ Y_2 \\ Z_2 \end{Bmatrix}, \tag{4.1}$$

where (X_b, Y_b, Z_b) is the coordinate system of beam b (b=1, 2), ϕ is joint angle, and $\mathbf{T}_1$ is a coordinate transformation matrix. Using above relation, the displacement and rotation continuities can be written as

$$\left.\begin{Bmatrix} u_{X_1}^* \\ u_{Y_1}^* \\ u_{Z_1}^* \end{Bmatrix}\right|_p - \mathbf{T}_1 \left.\begin{Bmatrix} u_{X_2}^* \\ u_{Y_2}^* \\ u_{Z_2}^* \end{Bmatrix}\right|_p = 0, \tag{4.2}$$

$$\left.\begin{Bmatrix} \Theta_{X_1}^* \\ \Theta_{Y_1}^* \\ \Theta_{Z_1}^* \end{Bmatrix}\right|_p - \mathbf{T}_1 \left.\begin{Bmatrix} \Theta_{X_2}^* \\ \Theta_{Y_2}^* \\ \Theta_{Z_2}^* \end{Bmatrix}\right|_p = 0, \tag{4.3}$$

where $u_{K_b}^*$ and $\Theta_{K_b}^*$ are displacement and rotation in K (K=X_b, Y_b, Z_b) direction for beam b (b=1, 2), respectively, and $(\ )|_p$ is the value at connection point p (p=1,

$\cdots$, N_P; N_P: the number of the connection points).

4.1.1 Rotation on the joint section at an independent point

The connection points are classified into two types; independent point defined on a single edge and dependent point where multiple edges are connected, as shown in Fig. 4.1. In this section, calculation of rotations at an independent point is presented.

The rotations are calculated by differentiating the midline displacements, where the midline displacements at an independent point p can be written as

$$\left.\begin{Bmatrix} u_{n(e)} \\ u_{s(e)} \\ u_{z(e)} \end{Bmatrix}\right|_p = \boldsymbol{\psi}(s_{e,p})\boldsymbol{\xi}(z_p), \tag{4.4}$$

where $u_{k(e)}$ (k=n, s, z) is k-directional displacement on edge e, and $s_{e,p}$ and z_p are s_e and z coordinates of the point p, respectively. Note that s_e is the shear directional axis of edge e as shown in Fig. 2.1. $\boldsymbol{\psi}$ in Eq. (4.4) is shape function matrix for cross-section mode vector $\boldsymbol{\xi}$ as

$$\boldsymbol{\psi} = \begin{bmatrix} \boldsymbol{\psi}_n \\ \boldsymbol{\psi}_s \\ \boldsymbol{\psi}_z \end{bmatrix} = \begin{bmatrix} \psi_n^{U_x} & \cdots & \psi_n^{\xi_{ND}} \\ \psi_s^{U_x} & \cdots & \psi_s^{\xi_{ND}} \\ \psi_z^{U_x} & \cdots & \psi_z^{\xi_{ND}} \end{bmatrix}. \tag{4.5}$$

Rotations can be calculated by differentiating the displacements in Eq. (4.4) as

$$\Theta_n = \frac{\partial u_z}{\partial s};\ \Theta_s = \frac{\partial u_n}{\partial z};\ \Theta_z = -\frac{\partial u_n}{\partial s}, \tag{4.6}$$

where Θ_k (k=n, s, z) is k-directional rotation. Rotations in Eq. (4.6) can be represented in a matrix form using Eq. (4.4) as

$$\begin{aligned}\left.\begin{Bmatrix}\Theta_{n(e)}\\ \Theta_{s(e)}\\ \Theta_{z(e)}\end{Bmatrix}\right|_p &= \begin{bmatrix}0 & 0 & 1\\ 0 & 0 & 0\\ -1 & 0 & 0\end{bmatrix}\frac{\partial}{\partial s}\left.\begin{Bmatrix}u_{n(e)}\\ u_{s(e)}\\ u_{z(e)}\end{Bmatrix}\right|_p + \begin{bmatrix}0 & 0 & 0\\ 1 & 0 & 0\\ 0 & 0 & 0\end{bmatrix}\frac{\partial}{\partial z}\left.\begin{Bmatrix}u_{n(e)}\\ u_{s(e)}\\ u_{z(e)}\end{Bmatrix}\right|_p \\ &= \mathbf{Q}_1\dot{\boldsymbol{\psi}}(s_{e,p})\xi(z_p) + \mathbf{Q}_2\boldsymbol{\psi}(s_{e,p})\xi'(z_p),\end{aligned} \tag{4.7}$$

where $\mathbf{Q}_1$ and $\mathbf{Q}_2$ are incidence matrices. The rotations in Eq. (4.7) can be written for local coordinate system of a beam (X, Y, Z) as

$$\begin{aligned}\left.\begin{Bmatrix}\Theta_X\\ \Theta_Y\\ \Theta_Z\end{Bmatrix}\right|_p &= \begin{bmatrix}\sin\alpha_e & \cos\alpha_e & 0\\ -\cos\alpha_e & \sin\alpha_e & 0\\ 0 & 0 & 1\end{bmatrix}\left.\begin{Bmatrix}\Theta_{n(e)}\\ \Theta_{s(e)}\\ \Theta_{z(e)}\end{Bmatrix}\right|_p \\ &= \mathbf{T}_2\mathbf{Q}_1\dot{\boldsymbol{\psi}}(s_{e,p})\xi(z_p) + \mathbf{T}_2\mathbf{Q}_2\boldsymbol{\psi}(s_{e,p})\xi'(z_p),\end{aligned} \tag{4.8}$$

where $\mathbf{T}_2$ is a coordinate transformation matrix. The rotations on the joint section are the same as those on the beam section as

$$\begin{aligned}\left.\begin{Bmatrix}\Theta^*_X\\ \Theta^*_Y\\ \Theta^*_Z\end{Bmatrix}\right|_p &= \left.\begin{Bmatrix}\Theta_X\\ \Theta_Y\\ \Theta_Z\end{Bmatrix}\right|_p \\ &= \mathbf{T}_2\mathbf{Q}_1\dot{\boldsymbol{\psi}}(s_{e,p})\xi(z_p) + \mathbf{T}_2\mathbf{Q}_2\boldsymbol{\psi}(s_{e,p})\xi'(z_p) \\ &= \mathbf{T}_2\begin{bmatrix}\mathbf{Q}_1\dot{\boldsymbol{\psi}}(s_{e,p}) & \mathbf{Q}_2\boldsymbol{\psi}(s_{e,p})\end{bmatrix}\begin{Bmatrix}\xi(z_p)\\ \xi'(z_p)\end{Bmatrix} \\ &\triangleq \mathbf{S}_{R1,p}\begin{Bmatrix}\xi(z_p)\\ \xi'(z_p)\end{Bmatrix},\end{aligned} \tag{4.9}$$

where Θ^*_K (K=X, Y, Z) is the rotation on the joint section, and $\mathbf{S}_{R1p}$ is $3\times 2N_D$ matrix to calculate Θ^*_K at independent point p.

4.1.2 Rotation on the joint section at a dependent point

As briefly mentioned in Section 2.1, out-of-plane (z-directional) deformations used in this paper meet the C^1 continuity at the dependent points [40]. Therefore, at a dependent point, in-plane rotations (Θ_X and Θ_Y) are uniquely defined using differentiated z-directional displacements on any two connecting edges. Therefore, unlike in the independent points where Θ_X and Θ_Y are calculated using n- and z-directional displacements, Θ_X and Θ_Y at a dependent point are calculated using z-directional displacements only. For example, in-plane rotations at a dependent point p are calculated using the z-directional displacements on any two connecting edges $e1$ and $e2$ as below.

$$\begin{aligned}\left.\begin{Bmatrix}\Theta_X\\ \Theta_Y\end{Bmatrix}\right|_p &= \frac{1}{\sin(\alpha_{e1}-\alpha_{e2})}\begin{bmatrix}\cos\alpha_{e2} & -\cos\alpha_{e1}\\ \sin\alpha_{e2} & -\sin\alpha_{e1}\end{bmatrix}\left.\begin{Bmatrix}\Theta_{n(e1)}\\ \Theta_{n(e2)}\end{Bmatrix}\right|_p\\ &= \frac{1}{\sin(\alpha_{e1}-\alpha_{e2})}\begin{bmatrix}\cos\alpha_{e2} & -\cos\alpha_{e1}\\ \sin\alpha_{e2} & -\sin\alpha_{e1}\end{bmatrix}\begin{bmatrix}\dot{\boldsymbol{\psi}}_z(s_{e1,p})\\ \dot{\boldsymbol{\psi}}_z(s_{e2,p})\end{bmatrix}\boldsymbol{\xi}(z_p)\\ &\triangleq \mathbf{T}_3\begin{bmatrix}\dot{\boldsymbol{\psi}}_z(s_{e1,p})\\ \dot{\boldsymbol{\psi}}_z(s_{e2,p})\end{bmatrix}\boldsymbol{\xi}(z_p),\end{aligned} \tag{4.10}$$

where α_{e1} and α_{e2} are the angles of edges $e1$ and $e2$ with respect to the X axis, respectively, as shown in Fig. 2.1, and $\mathbf{T}_3$ is a transformation matrix. z-directional rotation can be calculated using n-directional displacement on any edge e, as in the dependent points.

$$\Theta_Z\big|_p = \Theta_{z(e)}\big|_p = -\dot{\boldsymbol{\psi}}_n(s_{e,p})\boldsymbol{\xi}(z_p). \tag{4.11}$$

Note in Eq. (4.11) that the subindex e can be the $e1$ or $e2$ because it does not matter which edge is chosen due to the slope continuities of ψ_n's at cross-section corners. The rotations on the joint section can be defined using Eqs. (4.10) and (4.11) as

$$\begin{aligned}\left.\begin{Bmatrix}\Theta_X^*\\ \Theta_Y^*\\ \Theta_Z^*\end{Bmatrix}\right|_p &= \left.\begin{Bmatrix}\Theta_X\\ \Theta_Y\\ \Theta_Z\end{Bmatrix}\right|_p = \begin{bmatrix}\mathbf{T}_3\begin{bmatrix}\dot{\boldsymbol{\psi}}_z(s_{e1,p})\\ \dot{\boldsymbol{\psi}}_z(s_{e2,p})\end{bmatrix} & \mathbf{0}\\ -\dot{\boldsymbol{\psi}}_n(s_{e,p}) & \end{bmatrix}\begin{Bmatrix}\boldsymbol{\xi}(z_p)\\ \boldsymbol{\xi}'(z_p)\end{Bmatrix}\\ &\triangleq \mathbf{S}_{R2,p}\begin{Bmatrix}\boldsymbol{\xi}(z_p)\\ \boldsymbol{\xi}'(z_p)\end{Bmatrix},\end{aligned} \tag{4.12}$$

where $\mathbf{S}_{R2,p}$ is $3\times2N_D$ matrix to calculate Θ_K^* at dependent point p. Note that $\mathbf{S}_{R2p}$ contains a zero matrix to match the format with $\mathbf{S}_{R1,p}$ in Eq. (4.9).

4.1.3 Displacement on the joint section

The displacements at connection point p can be represented as

$$\begin{aligned}\left.\begin{Bmatrix}u_X\\ u_Y\\ u_Z\end{Bmatrix}\right|_p &= \begin{bmatrix}\sin\alpha_e & \cos\alpha_e & 0\\ -\cos\alpha_e & \sin\alpha_e & 0\\ 0 & 0 & 1\end{bmatrix}\left.\begin{Bmatrix}u_{n(e)}\\ u_{s(e)}\\ u_{z(e)}\end{Bmatrix}\right|_p\\ &= \mathbf{T}_2\boldsymbol{\psi}(s_{e,p})\boldsymbol{\xi}(z_p),\end{aligned} \tag{4.13}$$

where $\mathbf{T}_2$ is the transformation matrix in Eq. (4.8). Considering the additional displacements caused by rotations at a beam section, displacements on the joint section can be calculated as

$$\left.\begin{Bmatrix} u_X^* \\ u_Y^* \\ u_Z^* \end{Bmatrix}\right|_p = \left.\begin{Bmatrix} u_X \\ u_Y \\ u_Z \end{Bmatrix}\right|_p + r_p \begin{bmatrix} 0 & 1 \\ -1 & 0 \\ 0 & 0 \end{bmatrix} \left.\begin{Bmatrix} \theta_X + \Theta_X^{W1} \\ \theta_Y + \Theta_Y^{W1} \end{Bmatrix}\right|_p$$

$$= \mathbf{T}_2 \boldsymbol{\psi}(s_{e,p}) \boldsymbol{\xi}(z_p) + r_p \mathbf{Q}_3 \left.\begin{Bmatrix} \theta_X + \Theta_X^{W1} \\ \theta_Y + \Theta_Y^{W1} \end{Bmatrix}\right|_p , \tag{4.14}$$

where r_p is z-coordinate of joint section from the connection point p illustrated in Fig. 4.2(c), $\mathbf{Q}_3$ is an incidence matrix, θ_X and θ_Y are the bending rotation modes, and Θ_X^{W1} and Θ_Y^{W1} are rotation angles in X and Y directions caused by linear warping modes. Note in Eq. (4.14) that only bending rotation modes and linear warping modes are considered for the additional displacements on the joint section, where the linear warping modes mean warping modes that cause linear deformations as shown in Fig. 4.3. The bending rotation modes θ_X and θ_Y can be calculated by transforming the bending rotation modes in Eq. (2.2) as

$$\left.\begin{Bmatrix} \theta_X \\ \theta_Y \end{Bmatrix}\right|_p = \begin{bmatrix} \cos\bar{\beta} & -\sin\bar{\beta} \\ \sin\bar{\beta} & \cos\bar{\beta} \end{bmatrix} \left.\begin{Bmatrix} \theta_{\bar{x}} \\ \theta_{\bar{y}} \end{Bmatrix}\right|_p \triangleq \mathbf{T}_4 \left.\begin{Bmatrix} \theta_{\bar{x}} \\ \theta_{\bar{y}} \end{Bmatrix}\right|_p , \tag{4.15}$$

where $\bar{\beta}$ is the orientation angle of the principal axes in Fig. 2.1, $\mathbf{T}_4$ is a transformation matrix, and $\theta_{\bar{x}}$ and $\theta_{\bar{y}}$ are the 4th and 5th components of $\boldsymbol{\xi}$ in Eq. (2.2):

$$\left.\begin{Bmatrix} \theta_{\bar{x}} \\ \theta_{\bar{y}} \end{Bmatrix}\right|_p = \begin{bmatrix} 0 & 0 & 0 & 1 & 0 & 0 & \cdots & 0 \\ 0 & 0 & 0 & 0 & 1 & 0 & \cdots & 0 \end{bmatrix} \boldsymbol{\xi}(z_p) \triangleq \mathbf{Q}_4 \boldsymbol{\xi}(z_p), \tag{4.16}$$

where $\mathbf{Q}_4$ is an incidence matrix to select the bending rotation modes from the cross-section modes vector. The rotation angles by the linear warping modes can be calculated as

$$\left.\begin{Bmatrix} \Theta_X^{W1} \\ \Theta_Y^{W1} \end{Bmatrix}\right|_p = \mathbf{R}_p \xi(z_p), \tag{4.17}$$

where

$$\mathbf{R}_p = \begin{cases} \begin{bmatrix} 1 & 0 & 0 \\ 0 & 1 & 0 \end{bmatrix} \mathbf{S}_{R,p}\mathbf{H} & \text{(open section)} \\ \mathbf{0} & \text{(closed section)} \end{cases}. \tag{4.18}$$

In Eq. (4.18), $\mathbf{R}_p$ is a matrix to select $(\Theta_X^{W1}, \Theta_Y^{W1})$ from (Θ_X, Θ_Y) in Eqs. (4.8, 10), and $\mathbf{S}_{R,p}$ is the matrix defined in Eqs. (4.9, 12) to calculate the rotation angles at connection point p:

$$\mathbf{S}_{R,p} = \begin{cases} \mathbf{S}_{R1,p} & \text{(independent point)} \\ \mathbf{S}_{R2,p} & \text{(dependent point)} \end{cases}. \tag{4.19}$$

Also, $\mathbf{H}$ in Eq. (4.18) is $2N_D \times N_D$ diagonal matrix to select the linear warping modes $\{\xi_7, \cdots, \xi_{6+N_{W1}}\}$ (N_{W1}: number of the linear warping modes) from all cross-section modes, whose components are

$$H_{aa} = \begin{cases} 1 & (7 \le a \le 6 + N_{W1}) \\ 0 & \text{(otherwise)} \end{cases}. \tag{4.20}$$

Note in Eq. (4.18) that the rotation angles by linear warping modes are considered only for the open section when the additional displacements on the joint section are calculated. This is done because it is already demonstrated in the studies of Choi et al. [37, 55, 56] that joint conditions can be derived without considering the additional displacements for the closed section. Substituting Eqs. (4.15-17) into Eq.

(4.14) gives

$$\left.\begin{Bmatrix} u_X^* \\ u_Y^* \\ u_Z^* \end{Bmatrix}\right|_p = \left[\mathbf{T}_2\boldsymbol{\psi}(s_{e,p}) + r_p\mathbf{Q}_3\left(\mathbf{T}_4\mathbf{Q}_4 + \mathbf{R}_p\right)\right]\boldsymbol{\xi}(z_p) \triangleq \mathbf{S}_{U,p}\boldsymbol{\xi}(z_p), \tag{4.21}$$

where $\mathbf{S}_{Up}$ is $3 \times N_D$ matrix to calculate the displacements on the joint section at the connection point p.

4.2 Joint conditions for finite elements

The nodal solution vector **d** in Eq. (2.18) is composed of degrees of freedom (DOFs) of each beam. For example, for a beam structure that consist of two beam members, **d** can be written as

$$\mathbf{d} = \begin{Bmatrix} \mathbf{d}^{[1]} \\ \mathbf{d}^{[2]} \end{Bmatrix}, \tag{4.22}$$

where $\mathbf{d}^{[b]}$ represents the DOF vector for beam b (b=1, 2). Because the Hermite cubic polynomials are used as the finite element shape functions, $\mathbf{d}^{[b]}$ is composed of the nodal DOFs and their derivatives as

$$\mathbf{d}^{[b]} = \left\{ \boldsymbol{\xi}_1^{[b]};\ \boldsymbol{\xi}_1'^{[b]};\ \cdots;\ \boldsymbol{\xi}_{N_N^b}^{[b]};\ \boldsymbol{\xi}_{N_N^b}'^{[b]} \right\},\ (b=1,2). \tag{4.23}$$

where $\boldsymbol{\xi}_c^{[b]}$ and $\boldsymbol{\xi}_c'^{[b]}$ are nodal DOF vector for node c (c=1, $\cdots$, N_N^b ; N_N^b : number of the finite element nodes of beam b) of beam b.

By substituting Eq. (4.21) into Eq. (4.2), the condition of displacement continuity for the nodal DOFs is defined as

$$\mathbf{S}_{U,p}^{[1]}\boldsymbol{\xi}_i^{[1]} - \mathbf{T}_1\mathbf{S}_{U,p}^{[2]}\boldsymbol{\xi}_j^{[2]} = 0,\ (1 \le i \le N_N^1;\ 1 \le j \le N_N^2), \tag{4.24}$$

where $\mathbf{S}_{U,p}^{[b]}$ is the matrix to calculate displacements on the joint section at connection point p (p=1, $\cdots$, N_P; N_P: number of the connection points) on beam b (b=1, 2), $\boldsymbol{\xi}_I^{[b]}$ is the DOFs at corresponding finite element node I (I=i, j). In the similar way, substituting Eqs. (4.9, 12) into Eq. (4.3) gives the condition of rotation continuity for the nodal DOFs as

$$\mathbf{S}_{R,p}^{[1]}\begin{Bmatrix}\boldsymbol{\xi}_i^{[1]}\\ \boldsymbol{\xi}_i'^{[1]}\end{Bmatrix}-\mathbf{T}_1\mathbf{S}_{R,p}^{[2]}\begin{Bmatrix}\boldsymbol{\xi}_j^{[2]}\\ \boldsymbol{\xi}_j'^{[2]}\end{Bmatrix}=0,\ (1\le i\le N_N^1;\ 1\le j\le N_N^2), \tag{4.25}$$

where $\mathbf{S}_{R,p}^{[b]}$ is the matrix to calculate rotations on the joint section at connection point p (p=1, $\cdots$, N_P; N_P: number of the connection points) on beam b (b=1, 2). Note that $\mathbf{S}_{R,p}^{[b]}$ depends on type of the connection point as explained in Sections 4.1.1 and 4.1.2;

$$\mathbf{S}_{R,p}^{[b]}=\begin{cases}\mathbf{S}_{R1,p}^{[b]} & \text{(independent point)}\\ \mathbf{S}_{R2,p}^{[b]} & \text{(dependent point)}\end{cases},\ (b=1,2), \tag{4.26}$$

where $\mathbf{S}_{R1,p}^{[b]}$ and $\mathbf{S}_{R2,p}^{[b]}$ are the matrices defined in Eqs. (4.9, 12), respectively.

4.3 Numerical examples

For the verification of the proposed joint conditions, several numerical tests that cover L-type and T-type joints are conducted. Because the higher-order modes used in this paper are verified only for the static and vibration analyses [40], higher level analyses like buckling analyses are not included here, but they are going to be studied in our next research.

In Sections 4.3.1 and 4.3.2, static and vibration analyses for several L-type joint structures that are solved in other earlier studies are conducted by the proposed approach. Also, the results by the proposed approach are compared with the results in each original paper. In Sections 4.3.3 and 4.3.4, the new problems are solved; T-type joint structures having complicated cross-sections, and a simplified automotive frame that is composed of various L- and T-type join parts. All the results in this section are compared with the results by the shell theory (ABAQUS S8R elements). The same Poisson's ratio and density (v = 0.3 and ρ = 7850 kg/m^3), and various Young's modulus (E = 205 GPa for Section 4.3.1, E = 210 GPa for Section 4.3.2, and E = 200 GPa for the other examples) are used in the examples.

4.3.1 An L-type joint structure with rectangular section

An L-type joint structure shown in Fig. 4.4, which is covered in the study of Choi et al. [55], is analyzed. One end of the structure is fixed, and the other end is assumed to be rigid and subjected to vertical force. The analysis is conducted with various joint angles ($\phi = 30^\circ$, 60° , 90°), and the results by the shell elements, the Timoshenko beam theory, the Choi's approach and the proposed approach are compared in Figs. 4.5-7 for each joint angle. Note that three rigid-body modes (vertical deflection, bending rotation, torsional rotation) are used in Timoshenko beam theory, and warping and distortion modes are additionally considered in the Choi's approach. Also, 43 cross-section modes derived by the method in Chapter 3 are used in the proposed approach. It is shown in the graphs in Figs. 4.5-7 that the results by the Choi's approach and the proposed approach agree with the shell results consistently for the joint angle, while the Timoshenko beam results does not. Figure 4.8 shows the differences of the tip deflection by the shell elements and the proposed approach for the case of $\phi = 30^\circ$. The horizontal axis of the graph indicates the number of the cross-section modes used in the proposed analysis. It can be seen from the graph that the difference decreases as more cross-section modes are used. When the three rigid-body modes are used in the proposed approach, the result is the same as that of the Timoshenko beam theory. To make the difference comes within 5%, more than 18 modes are needed. Also, in order to obtain better result than the Choi's approach, 31 or more modes have to be used. As a result, Choi's approach shows better accuracy when the same cross-section modes are used. This is because his approach is specialized in L-type joint sutures with a rectangular cross-section subjected to out-of-plane load, in the other words, his approach is limited to this case. Although the proposed approach needs many cross-section modes for accurate analysis, the efficient analysis is possible by considering higher-set modes only for the elements near the joint, while considering the first set modes for the remaining elements, as described in Appendix F. Compared to other existing approaches, the proposed joint condition has merits in that it can cover arbitrary loading and complicated structures in a consistent manner, as can be seen in later examples.

4.3.2 L-type joint structures with I-section

L-type joint structures with flange continuity and web continuity in Fig. 4.9 are analyzed to cover the problems in the studies of the GBT [66, 70]. Although both joint structures in the examples have the same cross-section, joint conditions in [66, 70] are different each other because they have different joint continuities. The support condition in Fig. 4.9, which applies to both example, implies that both ends of the structure are fixed and out-of-plane (Y_1 and Y_2) displacement at the center of the joint section is constrained. In the analyses by the proposed approach, 20 modes for Section 4.3.2.1 and 42 modes for Section 4.3.2.2 are used.

4.3.2.1 Flange continuity

A static analysis is performed for the I-beam structure with the flange continuity. Each member of the structure has a different length (L_1=4m and L_2=3m), and a torsional moment of 1000Nm is applied at the mid-span of the beam 1 (or at Z_1=2m). The analysis results in Fig. 4.10(a) show that torsional rotations by the

GBT [66] and the proposed approach are well matched with the shell result, while the Timoshenko beam theory yields too stiff result because transmission of the torsional rotation is not captured. Also, it can be seen from Fig. 4.10(b) that full transmission of the linear warping induced by equilibrium of the bimoment, which is demonstrated in [53], is well captured by the proposed approach.

4.3.2.2 Web continuity

A vibration analysis is performed for the L-type joint structure with the web continuity (L_1=L_2=3m). Table 4.1 shows the first 15 natural frequencies yielded by the shell elements, the GBT [70] and the proposed approach. From the table, it is found that both results by the GBT and the proposed approach show good agreements with the shell results.

It is worth noting that only unstiffened joints are dealt in this section although various stiffened joints are studied in the original examples in [66, 70], because stiffened joints cannot be modeled in the proposed approach. In the GBT, the stiffening effects of various types of joints are carefully implemented, and effective stiffened joint conditions are proposed. Although the proposed approach is limited to the unstiffened joints, it has a merit in that the joint condition can be defined in a consistent manner regardless of the joint continuity types, while different joint conditions are used in the GBT depending on the continuity. This is because the GBT is mainly interested in efficient analyses of building frames, while the proposed approach is focused on analyzing more complex structures such as automotive frames.

In Appendix G, additional tests are implemented for the structures in Section 4.3.2 to check whether the proposed joint condition works with the GBT modes, showing that it is effective not only for the proposed cross-section modes but also for the GBT modes.

4.3.3 A T-type joint structure with pentagonal and rectangular sections

A T-type joint structure in which a rectangular tube (beam 2) is connected to a pentagonal sectioned beam (beam 1) with the joint angle ϕ is analyzed (see Fig. 4.11). Both ends of the beam 1 is fixed, and one end of the beam 2 is assumed to be rigid and subjected to axial force. In the proposed approach, 57 modes for the pentagonal section and 46 modes for the rectangular section are used for analyses. Figures 4.12 show the deformed shapes calculated by the shell elements, the proposed approach and the Timoshenko beam theory for various joint angles ($\phi = 30^\circ, 60^\circ, 90^\circ$), and Fig. 4.13 shows the differences between the tip displacement (magnitude) by shell and both beam based approaches. It can be seen from Figs. 4.12 and 4.13 that the results by the proposed approach are almost the same as the shell results, while the Timoshenko beam theory gives inaccurate results.

4.3.4 A simplified vehicle frame

Figure 4.14(a) shows the line along the centroid of each member of the vehicle frame in Fig. 1.3. The frame is fixed at two points and subjected to torsional forces. The sections in which forces are applied are assumed to be rigid. Figure 4.14(b) shows cross-sections of the vehicle frame members. For each cross-section, 53, 35, 53, 53, 28, 53 and 53 modes are used in the proposed model. Detailed modeling information of members marked with blue numbers in Fig. 4.14(a) is given in Table 4.2.

It can be seen from Fig. 4.15 that the deformed shape of the proposed approach well matches with that of the shell elements, while the Timoshenko beam model is too stiff. Specifically, the difference of vertical displacement at point A in Fig. 4.14(a), one of the loading point, is calculated as 0.4% in the proposed approach and 45.5% in the Timoshenko beam theory, compared to the shell result. Also, the proposed approach gives outstanding results for the free vibration analysis of the vehicle frame as can be seen in Fig. 4.16.

Table 4.1 Natural frequencies (Hz) from the vibration analysis of an L-type joint structure in Section 4.3.2.2 (numbers in parentheses denote the differences (%) from the shell results)

Mode	Shell	GBT [70]	Proposed
1	27.92	28.21 (1.1)	27.42 (1.8)
2	28.90	29.23 (1.1)	28.38 (1.8)
3	38.24	39.02 (2.0)	37.66 (1.5)
4	40.63	42.23 (3.9)	40.40 (0.6)
5	77.67	79.45 (2.3)	78.63 (1.2)
6	90.98	91.87 (1.0)	90.03 (1.0)
7	95.93	99.49 (3.7)	95.68 (0.3)
8	108.06	112.42 (4.0)	108.13 (0.1)
9	118.68	122.43 (3.2)	117.97 (0.6)
10	144.94	149.09 (2.9)	143.24 (1.2)
11	147.80	153.34 (3.7)	148.05 (0.2)
12	160.07	164.61 (2.8)	165.21 (3.2)
13	179.67	185.93 (3.5)	176.29 (1.9)
14	223.83	231.94 (3.6)	217.10 (3.0)
15	234.54	241.16 (2.8)	231.70 (1.2)

Table 4.2 Beam modeling information for the vehicle frame in Fig. 4.14

Beam	Section	Orientation			End coordinates 1			End coordinates 2		
		X_G	Y_G	Z_G	X_G	Y_G	Z_G	X_G	Y_G	Z_G
1	1	1	0	0	0.50	0	1.60	0.50	0	2.40
2	2	0	0	-1	0.80	0.07	1.55	0.80	0.50	1.55
3	1	0	0	-1	-0.85	0	1.55	0.85	0	1.55
4	5	0	0	-1	-0.85	0.50	1.55	0.85	0.50	1.55
5	1	1	0	0	0.80	0	-1.50	0.80	0	1.50
6	6	1	0	0	0	0	0.05	0	0	1.50
7	3	-0.94	-0.24	0.24	0.75	0.53	1.53	0.52	1	1.06
8	3	-1	0	0	0.52	1	1.06	0.52	1.21	0.85
9	7	0	0.71	-0.71	-0.47	1.07	0.93	0.47	1.07	0.93
10	3	-1	0	0	0.52	1.21	0.85	0.52	1.21	-0.85
11	1	0	0	-1	-0.75	0	0	0.75	0	0
12	4	0	0	1	0.79	0.07	0	0.79	0.95	0
13	4	0	0	1	0.79	0.95	0	0.54	1.19	0
14	7	0	0	-1	-0.47	1.17	0	0.47	1.17	0
15	6	1	0	0	0	0	-1.50	0	0	-0.05
16	3	-1	0	0	0.52	1.21	-0.85	0.52	1	-1.06
17	7	0	-0.71	-0.71	-0.47	1.07	-0.93	0.47	1.07	-0.93
18	3	-0.94	-0.24	-0.24	0.52	1	-1.06	0.75	0.53	-1.53
19	2	0	0	-1	0.80	0.07	-1.55	0.80	0.50	-1.55
20	1	0	0	-1	-0.85	0	-1.55	0.85	0	-1.55
21	5	0	0	-1	-0.85	0.50	-1.55	0.85	0.50	-1.55

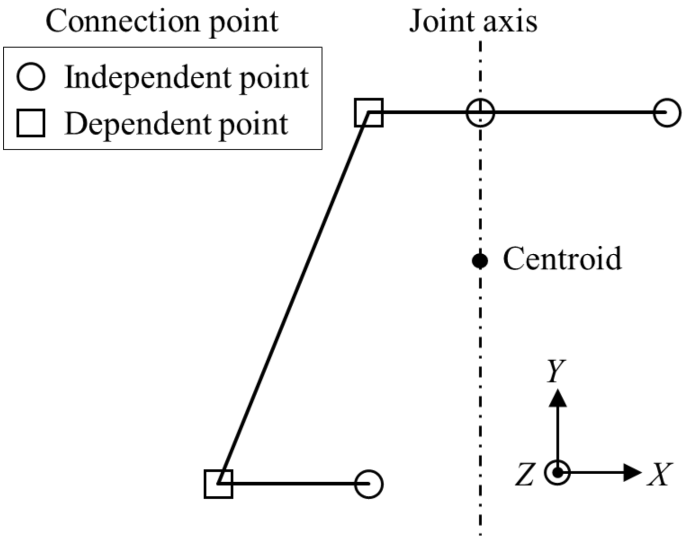

Fig. 4.1 Connection points on a thin-walled cross-section

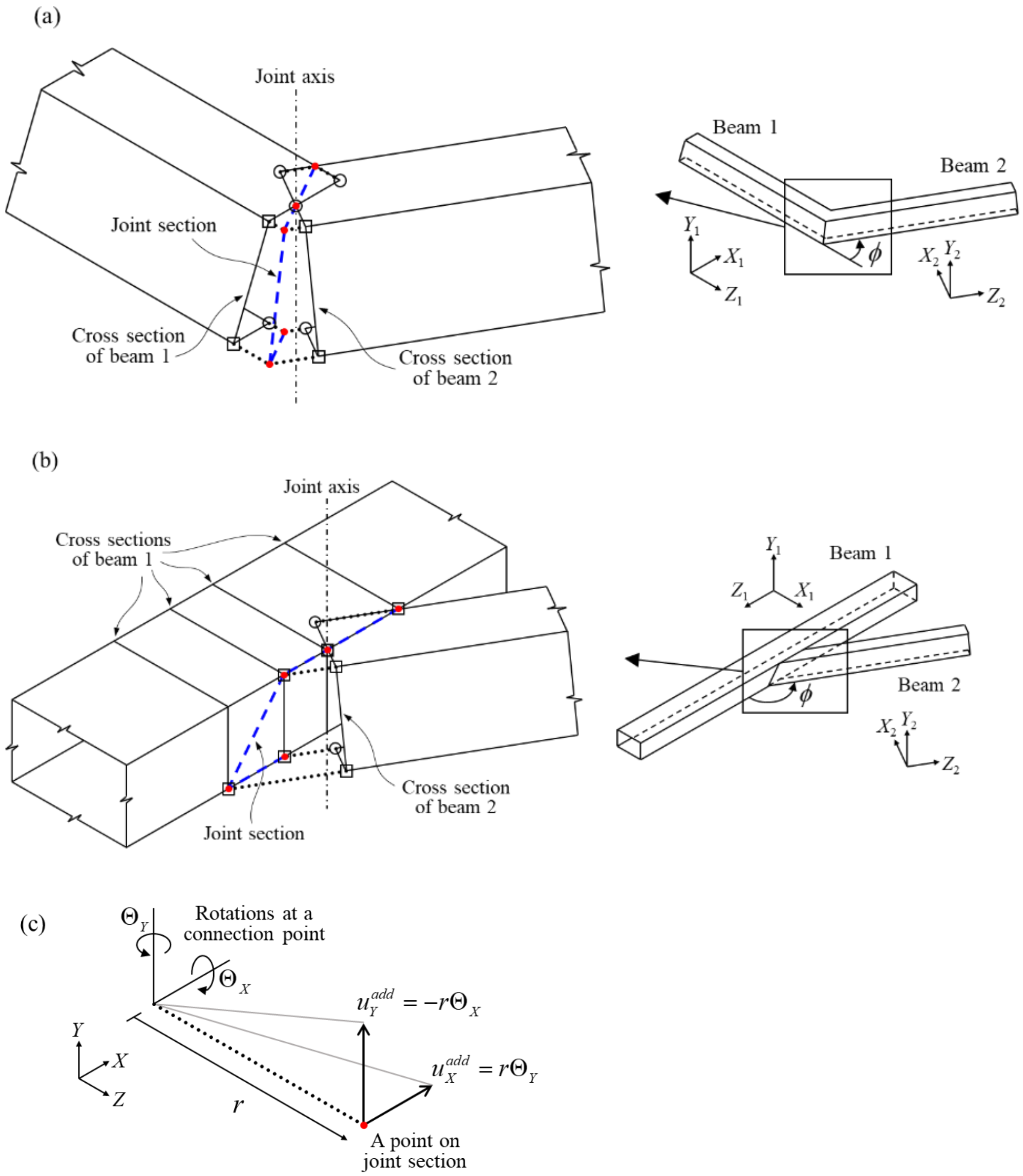

Fig. 4.2 One-dimensional models of (a) L-type joint and (b) T-type joint, and (c) additional displacements on joint section by rotations at a connection point

(a)

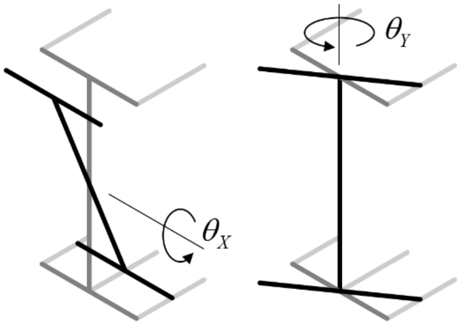

(b)

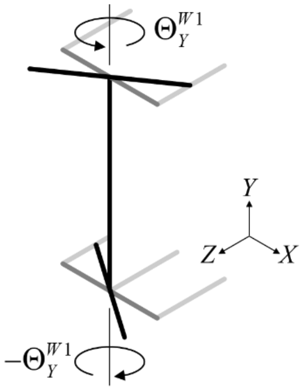

Fig. 4.3 Rotations that cause additional displacements on joint section: (a) sectional rotations by the bending rotation modes and (b) edge rotations by a linear warping mode

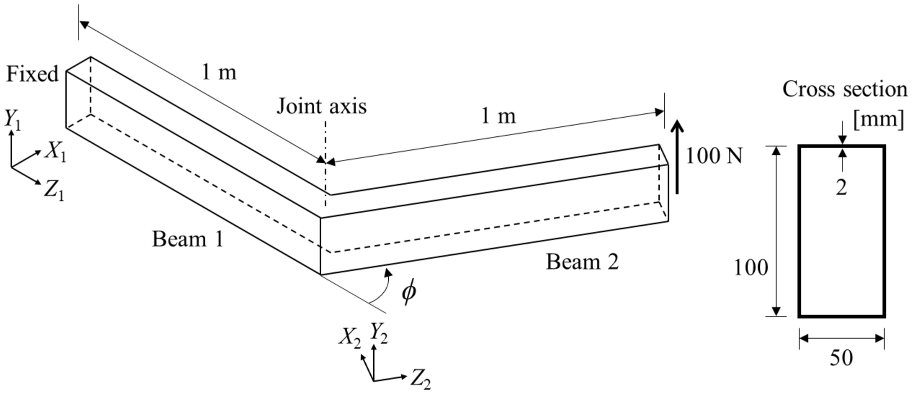

Fig. 4.4 L-type joint structure with rectangular section subjected to vertical force

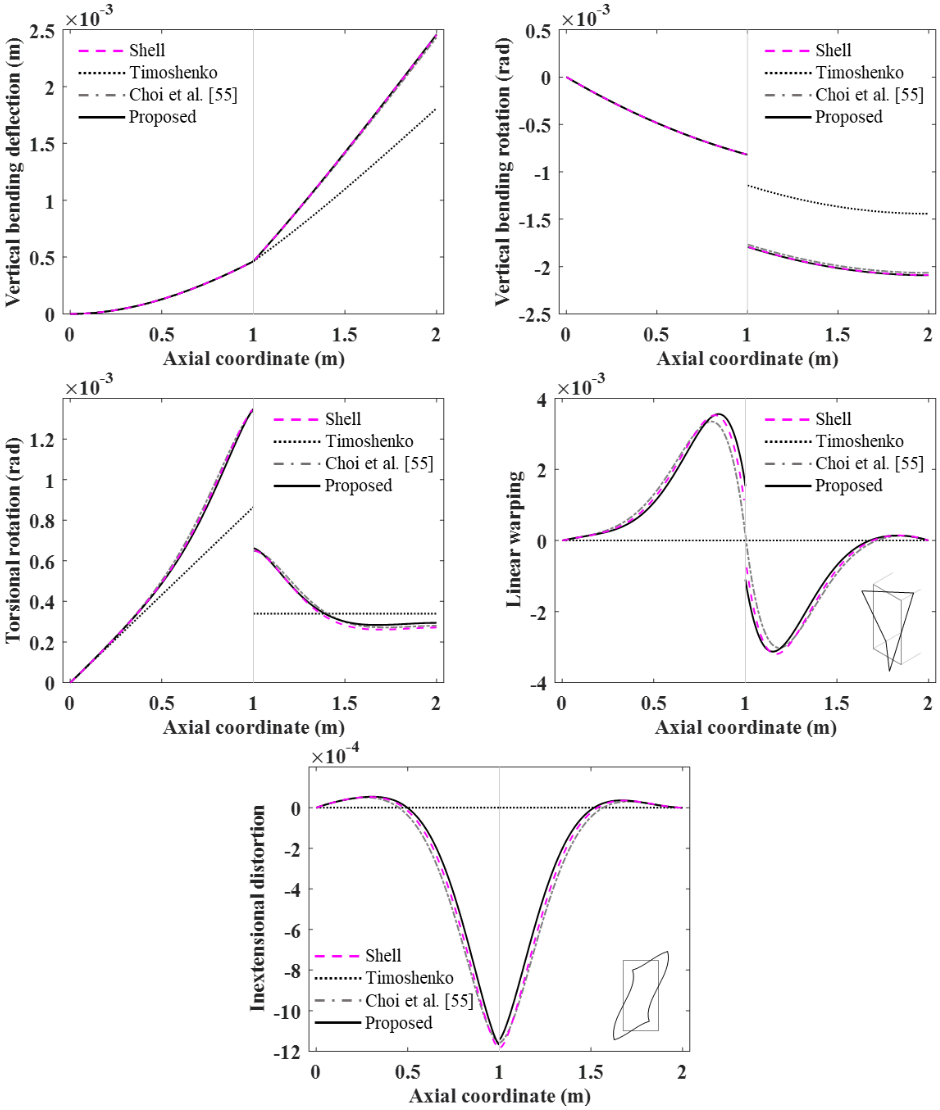

Fig. 4.5 Analysis results of the problem in Fig. 4.4 with $\phi = 30^\circ$

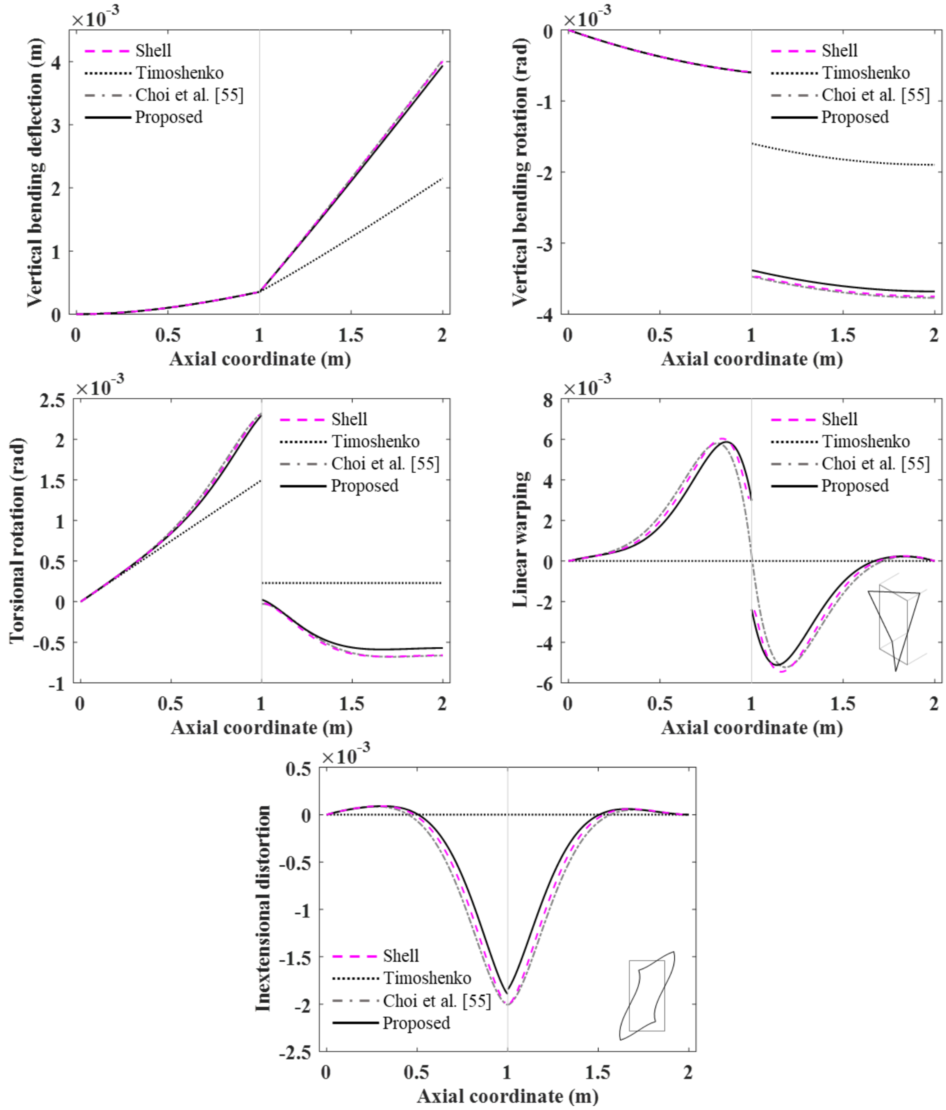

Fig. 4.6 Analysis results of the problem in Fig. 4.4 with $\phi = 60^{\circ}$

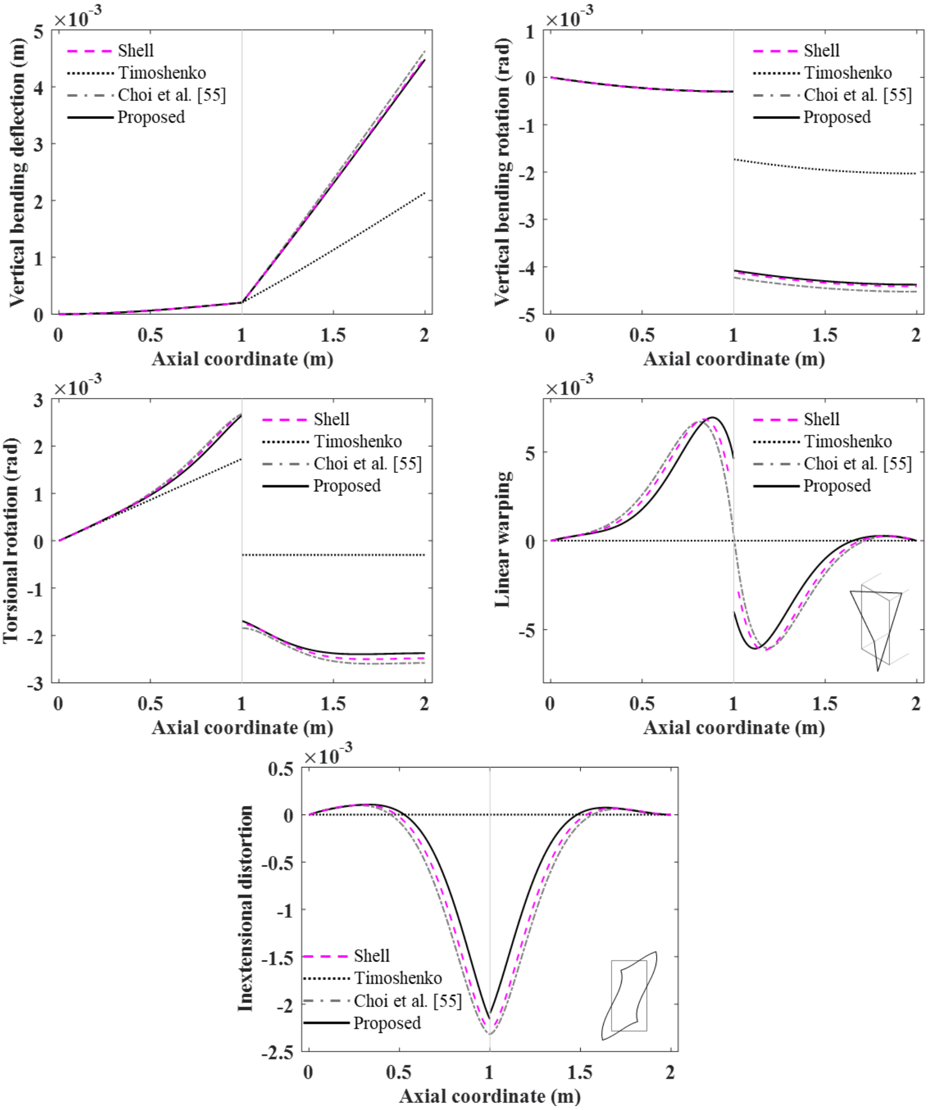

Fig. 4.7 Analysis results of the problem in Fig. 4.4 with $\phi = 90^{\circ}$

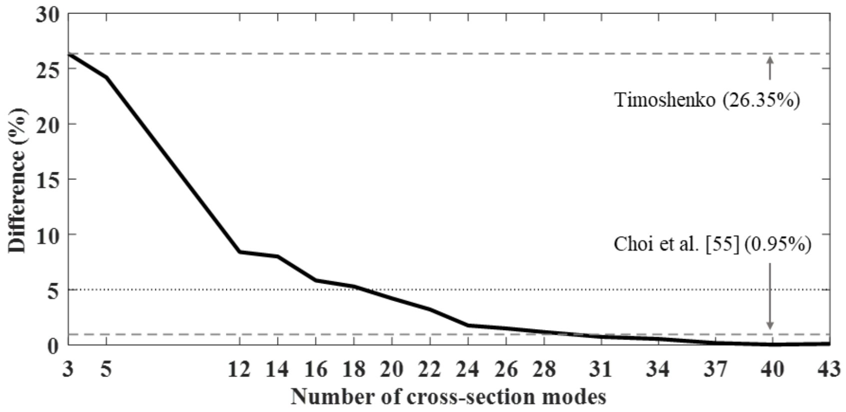

Fig. 4.8 Accuracy convergence of the tip deflection in Fig. 4.5 for the number of used cross-section modes

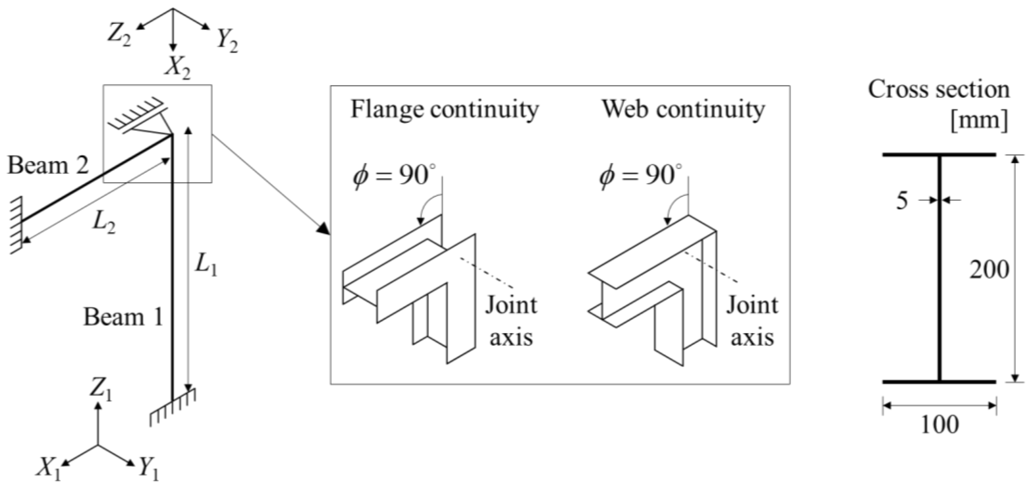

Fig. 4.9 L-type joint structure with I-section, and boundary conditions

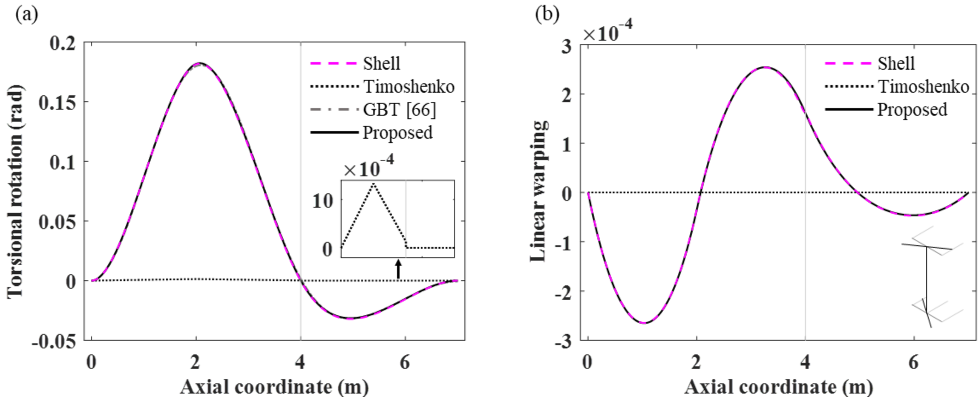

Fig. 4.10 Static analysis results of the problem in Section 4.3.2.1: (a) torsional rotation and (b) linear warping mode

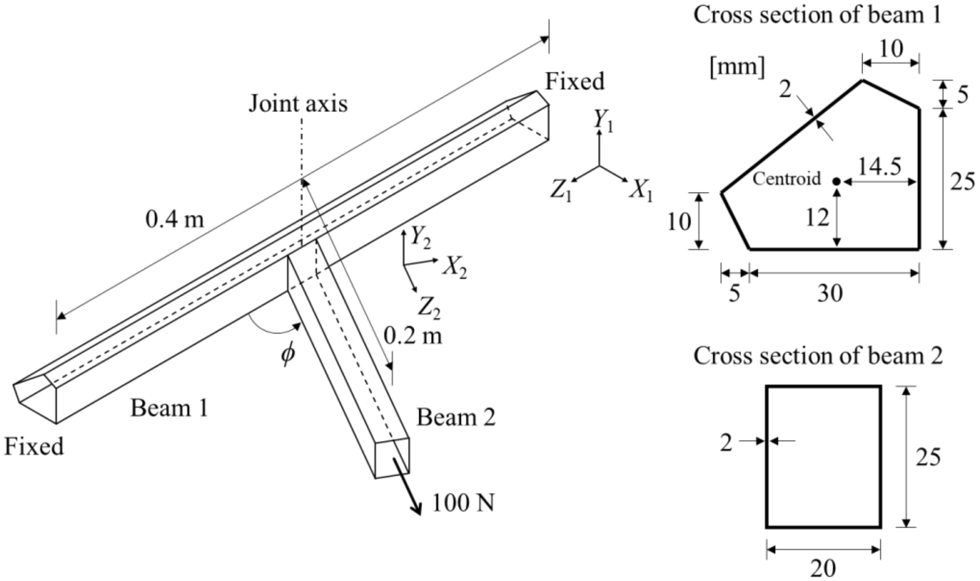

Fig. 4.11 T-type joint structure with pentagonal and rectangular sections subjected to axial force

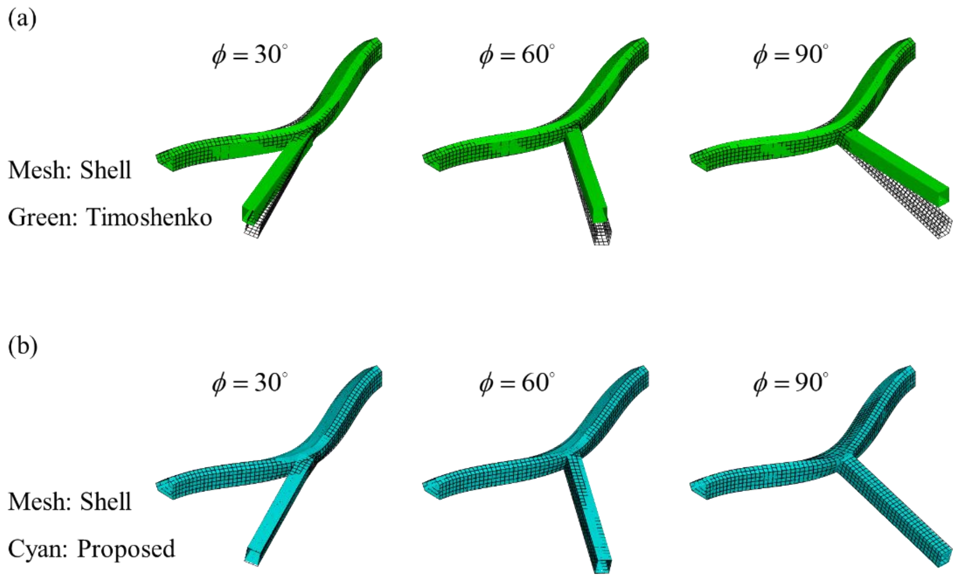

Fig. 4.12 Deformed shapes of the T-type joint structure in Fig. 4.11 with various joint angles ($\phi = 30^{\circ}, 60^{\circ}, 90^{\circ}$) yielded by the shell elements, the Timoshenko beam theory and the proposed approach

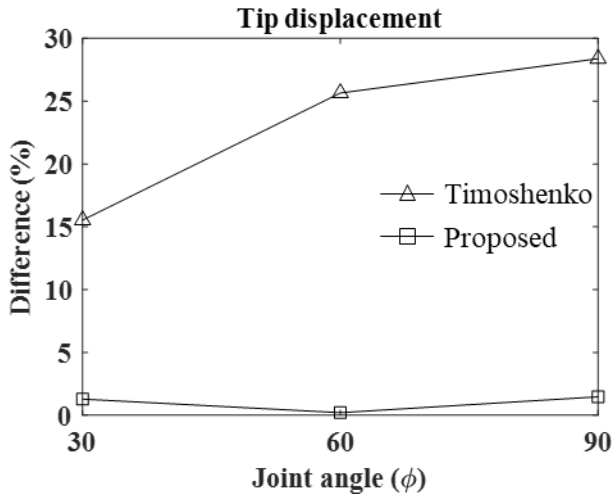

Fig. 4.13 Accuracy of the tip displacements in Fig. 4.12

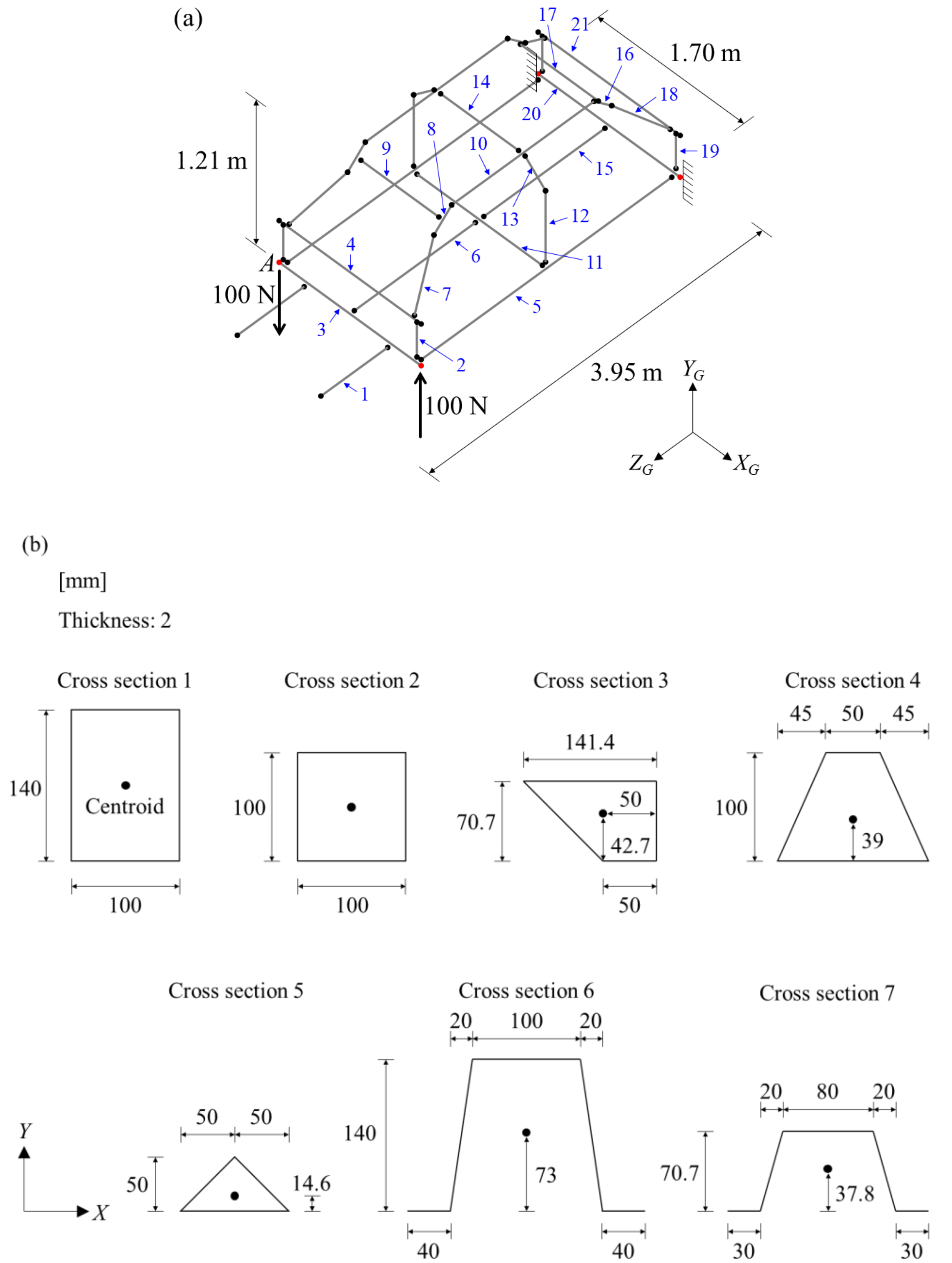

Fig. 4.14 (a) Dimensions and boundary conditions of the vehicle frame in Fig. 1.3 (the numbers in blue indicate beam numbers in Table 4.1), and (b) cross-sections of the members

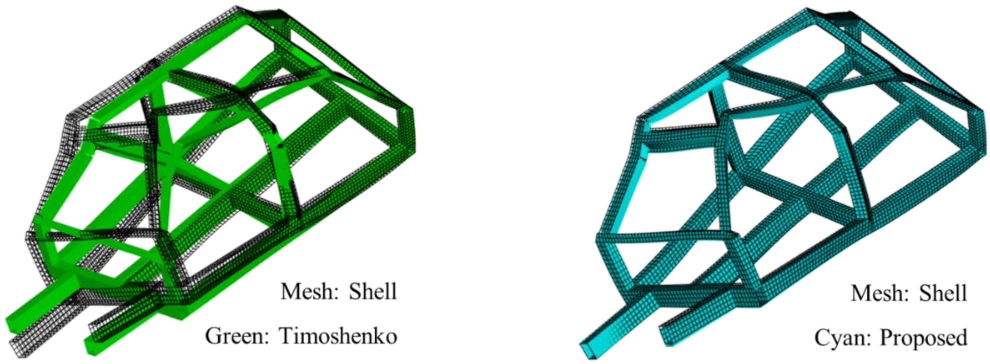

Fig. 4.15 Deformed shapes of the vehicle frame in Fig. 4.14 yielded by the shell elements, the Timoshenko beam theory and the proposed approach

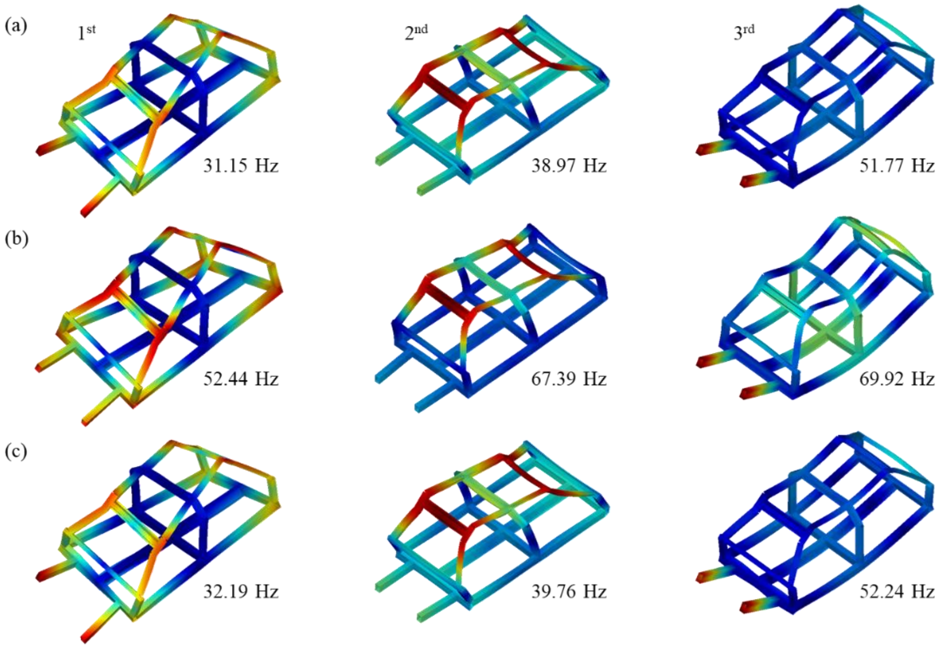

Fig. 4.16 Free vibration analysis results of the vehicle frame in Fig. 4.14 yielded by (a) the shell elements, (b) the Timoshenko beam theory and (c) the proposed approach

CHAPTER 5.
Conclusions

Through this dissertation, we presented a procedure for the one-dimensional modeling of complicated beam structures.

In Chapter 3, an analytic and systematic approach to derive cross-section modes of a thin-walled cross-section is proposed. While other constitutive relation-based approaches were limited to rectangular cross-sections, the proposed approach is applicable to arbitrarily shaped general sections, for which a formulation utilizing an eigenvalue problem was newly presented. This required the use of orthogonality among cross-section modes, from which the coefficients of basis functions for the modes in the higher set can be obtained as eigenvectors. For hierarchical derivation from lower to higher modes, we first derived integral equations between lower and higher modes using constitutive equations of a plane stress state. By doing so, the modes in the higher mode set can represent the strain field corresponding to the stress field generated by the modes in lower sets. To confirm the validity, the proposed cross-section modes were used for analyses of various thin-walled beams, whose results were compared with those by other beam-based approaches as well as full shell models. The numerical results showed that the proposed approach can yield excellent accuracy for three-dimensional displacements only using up to second set of cross-section modes. To correctly estimate rapidly changing stress by the end effect, more modes from higher-order mode sets might be required, but the error can be reduced to less than 1% as long as sufficient higher modes are employed.

In Chapter 4, an approach to define the joint condition was proposed. In the proposed approach, the joint condition is derived using the displacement and rotation continuities at the connection points. Although many enriched joint conditions that use the continuities have been proposed, e.g., the GBT, the proposed approach have some merits. First, the way the connection points are set is consistent regardless of the cross-section shapes. Second, additional displacements on the joint section caused by the rotations at a connection point are taken into account. The consideration of the additional displacements is essential for an authentic assessment of displacements at the joint, because the beam section and the joint section are in different planes for general joint angle. For the verification of the proposed joint condition, four examples were implemented. In the first two examples that were covered by Choi et al. and the GBT, respectively, it was shown that both results by the proposed approach and existing studies agree well with the shell results. Although each existing study shows its own uniqueness, it also was able to be found that the proposed joint condition has an advantage in that it is applicable to various cross-sections in a consistent manner. Last two examples covered more complicated joint structures; a T-type joint structure and a vehicle frame that is composed of various L- and T-type joints. Results of the examples showed that the proposed approach is suitable to analyze complicated and practical structures.

This dissertation showed that effective one-dimensional analyses of complicated structures can be made using the proposed approaches, while other existing beam theories are limited to simple cases only. The proposed joint condition also has a limitation in that it can be used only if the connection points of beams can meet at the intersection point by extending them along the beam axis, making it challenging to cover the vehicle frames having complex joint parts. For future works, joints of beams of chamfered section and beams of different heights will be studied.

APPENDIX A.
Determination of centroid and principal axes

Coordinates of the centroid on a cross-section are

$$X_C = \frac{\sum_{e=1}^{N_E}\left(X_e l_e + \frac{l_e^2}{2}\cos\alpha_e\right)}{\sum_{e=1}^{N_E} l_e}, \tag{A.1}$$

$$Y_C = \frac{\sum_{e=1}^{N_E}\left(Y_e l_e + \frac{l_e^2}{2}\sin\alpha_e\right)}{\sum_{e=1}^{N_E} l_e}, \tag{A.2}$$

where (X_e, Y_e) and α_e are the origin and the orientation angle of local coordinate system of edge e, l_e is the length of edge e, and N_E is the number of cross-section edges.

Using the obtained X_C and Y_C, the orientation angle of the principal axes can be calculated as

$$\bar{\beta} = \frac{1}{2}\tan^{-1}\left(\frac{2B_1}{B_2 - B_3}\right), \tag{A.3}$$

where

$$B_1 = \sum_{e=1}^{N_E} l_e \left[\left(X_e - X_C + \frac{l_e}{2}\cos\alpha_e \right)\left(Y_e - Y_C + \frac{l_e}{2}\sin\alpha_e \right) + \frac{l_e^2}{24}\sin(2\alpha_e) \right], \quad \text{(A.4)}$$

$$B_2 = \sum_{e=1}^{N_E} l_e \left[(X_e - X_C)^2 + l_e (X_e - X_C)\cos\alpha_e + \frac{l_e^2}{3}\cos^2\alpha_e \right], \quad \text{(A.5)}$$

$$B_3 = \sum_{e=1}^{N_E} l_e \left[(Y_e - Y_C)^2 + l_e (Y_e - Y_C)\sin\alpha_e + \frac{l_e^2}{3}\sin^2\alpha_e \right]. \quad \text{(A.6)}$$

APPENDIX B.
Corner continuity condition for *s*-directional displacements

If more than two edges are connected at a corner, the *s*-directional displacement of an edge at the corner should be represented by those of any other two edges according to the displacement continuity. For example, if edges $e1$, $e2$ and $e3$ are connected at corner r, the *s*-directional displacement on edge $e3$, $u_{s(e3)}$, can be expressed in terms of $u_{s(e1)}$ and $u_{s(e2)}$ as

$$\begin{aligned} u_{s(e3)}\Big|_r &= \{\cos\alpha_{e3} \quad \sin\alpha_{e3}\}\begin{Bmatrix} u_X \\ u_Y \end{Bmatrix}\Bigg|_r \\ &= \{\cos\alpha_{e3} \quad \sin\alpha_{e3}\}\begin{bmatrix} \cos\alpha_{e1} & \sin\alpha_{e1} \\ \cos\alpha_{e2} & \sin\alpha_{e2} \end{bmatrix}^{-1}\begin{Bmatrix} u_{s(e1)} \\ u_{s(e2)} \end{Bmatrix}\Bigg|_r . \end{aligned} \tag{B.1}$$

If $u_s = \psi_s^{\chi^*}\chi^* = \mathbf{\delta c}^*\chi^*$ according to Eqs. (3.9-3.12), Eq. (B.1) can be written as

$$\left\{\mathbf{\delta}_{(e3)} - \frac{\sin(\alpha_{e3}-\alpha_{e2})}{\sin(\alpha_{e1}-\alpha_{e2})}\mathbf{\delta}_{(e1)} - \frac{\sin(\alpha_{e1}-\alpha_{e3})}{\sin(\alpha_{e1}-\alpha_{e2})}\mathbf{\delta}_{(e2)}\right\}\Bigg|_r \mathbf{c}^* \triangleq \mathbf{R}_r^{\chi^*}\mathbf{c}^* = 0. \tag{B.2}$$

If corner r has N_E^r connecting edges, ($N_E^r - 2$) continuity conditions of Eq. (B.2) should be considered.

APPENDIX C.
Corner continuity conditions for *n*-directional displacements

The *n*-directional shape function of an in-plane mode should be defined to satisfy the continuity with corner displacement. For example, if the displacement at corner r is expressed by already defined s-directional shape functions of edges $e1$ and $e2$, the displacement continuity for edge ei (i = 1, 2, $\cdots, N_E^r$; N_E^r : number of connecting edges at corner r) is

$$\psi_{n(ei)}^{\chi}\Big|_r = \left(-\frac{\cos(\alpha_{e2}-\alpha_{ei})}{\sin(\alpha_{e1}-\alpha_{e2})}\psi_{s(e1)}^{\chi} + \frac{\cos(\alpha_{e1}-\alpha_{ei})}{\sin(\alpha_{e1}-\alpha_{e2})}\psi_{s(e2)}^{\chi} \right)\Bigg|_r , \tag{C.1}$$

where the corner displacement by s-directional shape function is expressed using Eq. (B.2).

In addition, the slope continuity conditions and moment equilibrium are

$$\dot{\psi}_{n(ej)}^{\chi}\Big|_r - \dot{\psi}_{n(e1)}^{\chi}\Big|_r = 0, \ (j = 2, 3, \cdots, N_E^r), \tag{C.2}$$

$$\sum_{i=1}^{N_E^r} \omega_i \, \ddot{\psi}_{n(ei)}^{\chi}\Big|_r = 0, \tag{C.3}$$

where ω_i = 1 for $s = l_{ei}$ and $\omega_i = -1$ for s = 0 because the sign of the moment differs at both ends of an edge.

If $\psi^{\chi}_{n(ei)}$ is set as a quadratic function for an open edge and as a cubic function for a closed edge, the number of coefficients is always equal to the number of conditions in Eqs. (C.1-C.3); hence, the n-directional shape function can be uniquely defined.

APPENDIX D.

Equations for the number of cross-section modes

The number of modes for warping (N_{W*} and N_W), distortion ($N_{\chi*}$ and N_χ), and wall-bending modes (N_η) are

$$N_{W*} = 2N_E - 1 - \sum_{r=1}^{N_C} \left(M_1(r) + M_2(r) \right), \tag{D.1}$$

$$N_{\chi*} = N_E - 3 - \sum_{r=1}^{N_C} M_2(r), \tag{D.2}$$

$$N_W = N_E + N_{\hat{\chi}} - N_{\hat{W}} + 2 - \sum_{r=1}^{N_C} M_1(r), \tag{D.3}$$

$$N_\chi = N_E - N_{\hat{\chi}} + N_{\hat{W}} - 2 - \sum_{r=1}^{N_C} M_2(r), \tag{D.4}$$

$$N_\eta \le 5N_E + N_{\hat{\chi}} + 3 - \sum_{r=1}^{N_C} M_3(r), \tag{D.5}$$

where N_E and N_C are the number of cross-section edges and the number of corners, respectively, and $N_{\hat{W}}$ and $N_{\hat{\chi}}$ are correspondingly the numbers of warping and distortion modes already derived in the lower sets. Above, $M_i(r)$ (i = 1, 2, 3) denotes the number of continuity conditions at corner r:

$$M_1(r) = \begin{cases} N_E^r - 1 & (N_E^r > 1) \\ 0 & (N_E^r = 1) \end{cases}, \tag{D.6}$$

$$M_2(r) = \begin{cases} N_E^r - 2 & (N_E^r > 2) \\ 0 & (N_E^r \leq 2) \end{cases}, \tag{D.7}$$

$$M_3(r) = \begin{cases} 2N_E^r & (N_E^r > 1) \\ 1 & (N_E^r = 1) \end{cases}. \tag{D.8}$$

Here, N_E^r is the number of cross-section edges connected at corner *r*. Note that an inequality is used in Eq. (D.5). This is because the rank of the matrix used in the eigenvalue problem can be lower than the number of basis functions because of not considering the orthogonality between *n*-directional displacements and wall-bending modes.

APPENDIX E.

GBT modes used for problems in Section 3.3

Figures E.1-E.3 present the GBT modes employed in problems in Section 3.3. The modes are obtained using the GBTUL [12-17].

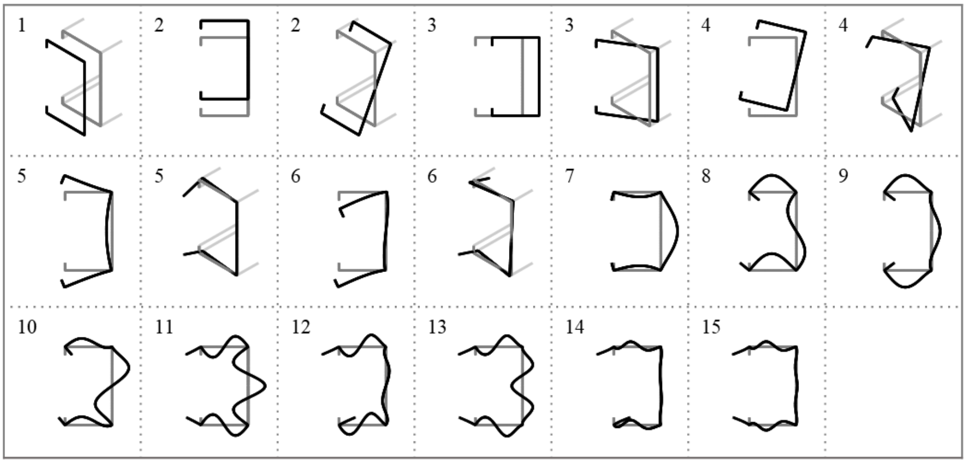

Fig. E.1 GBT modes employed in the analysis in Section 3.3.2

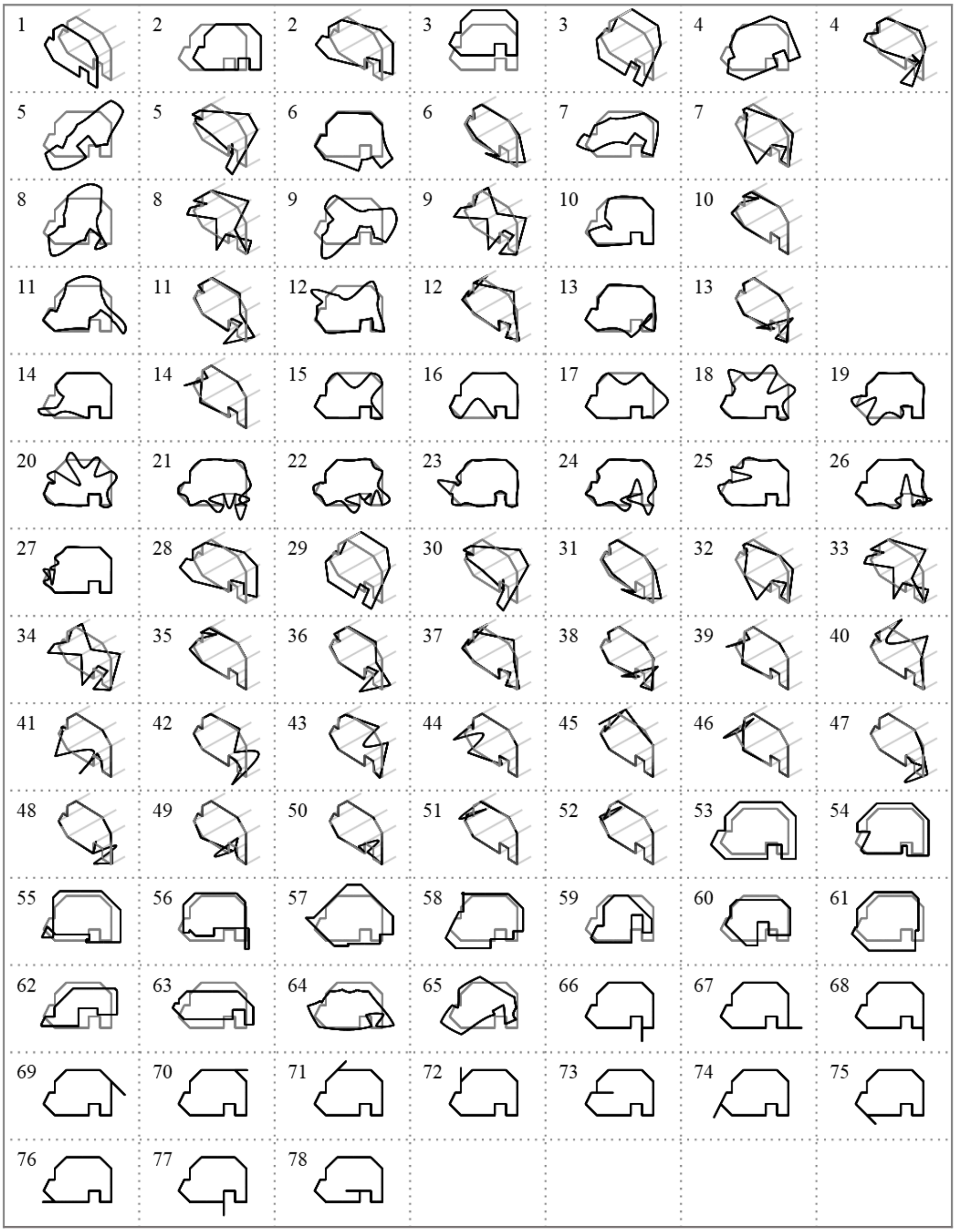

Fig. E.2 GBT modes for the cross-section in Fig. 3.3(b)

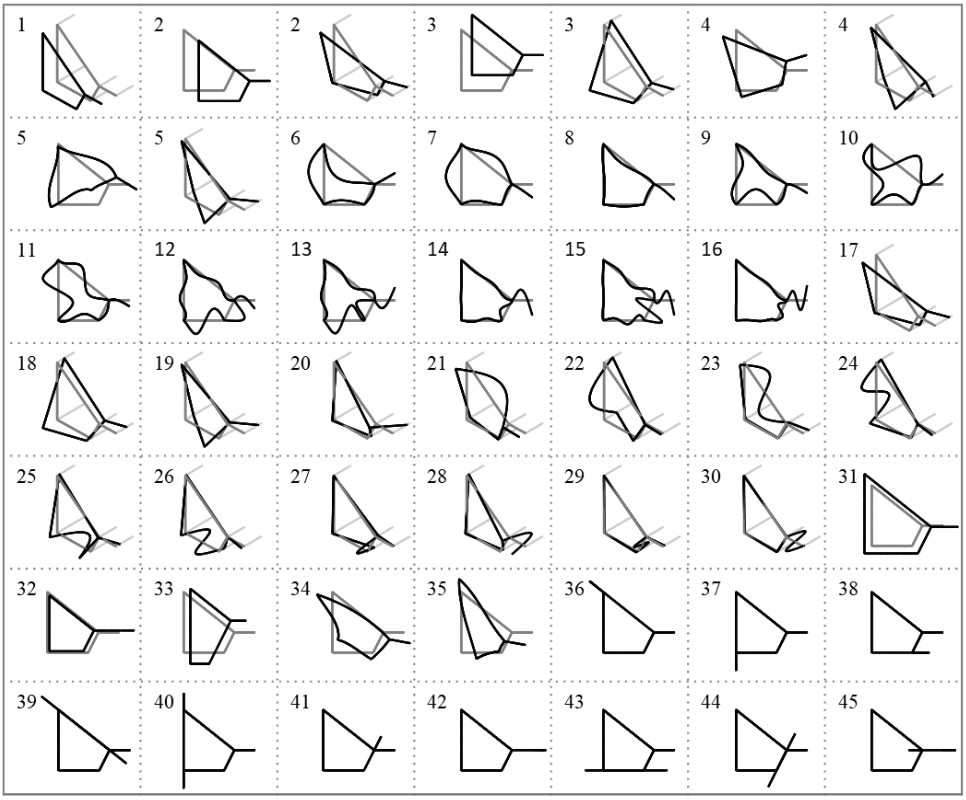

Fig. E.3 GBT modes for the cross-section in Fig. 3.3(c)

APPENDIX F.

Effectiveness of the use of higher-set modes for the joint

The L-type joint structure in Fig. 4.4 is analyzed for $\phi = 30^\circ$, considering 43 cross-section modes for the elements near the joint, while considering 8 cross-section modes used in [55] for the remaining elements. The total length of the joint elements of each beam is set 50mm. The analysis results in Fig. F.1 show that the efficient analysis is possible by considering higher-set modes only for the elements near the joint where complex deformations are occurred. In the analysis, 77% of degrees of freedom is reduced compared to the case of Section 4.3.1.

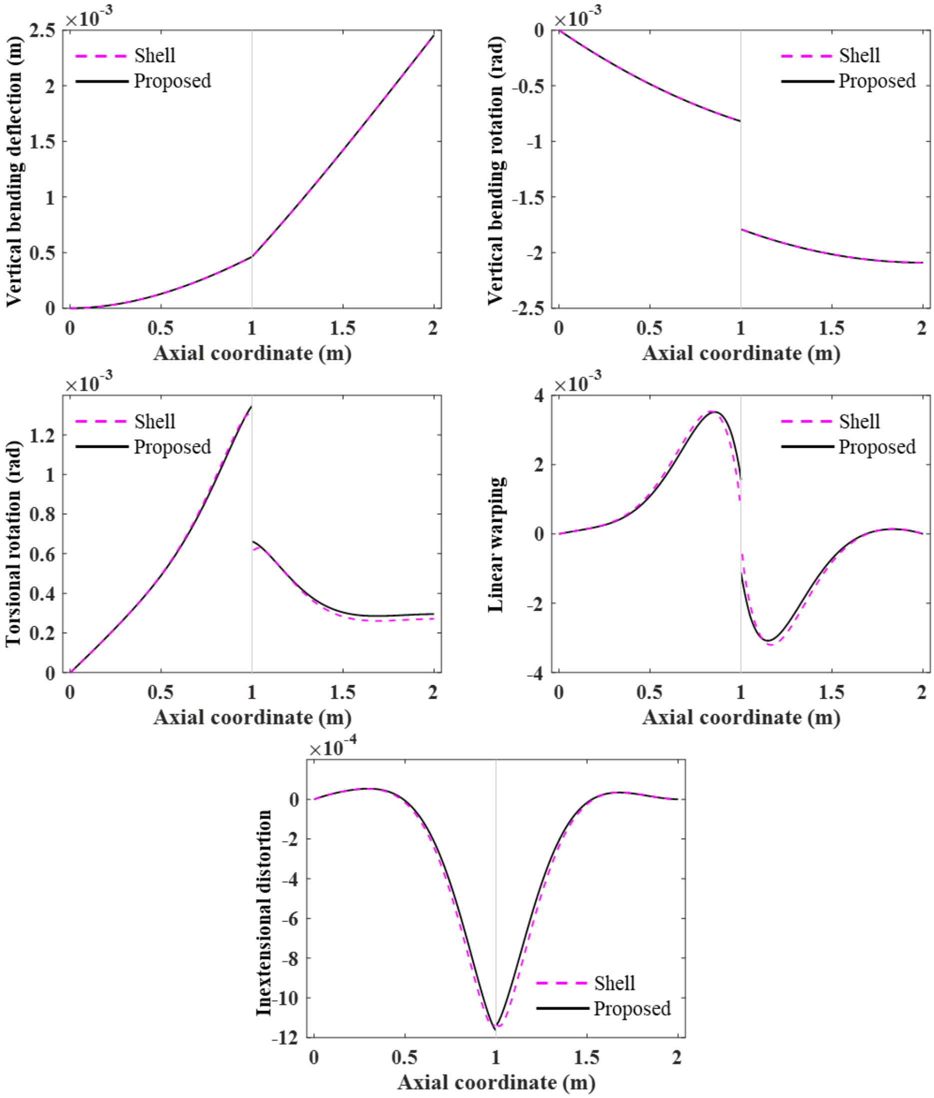

Fig. F.1 Analysis results of the problem in Fig. 4.4 with $\phi = 30^\circ$ considering 43 cross-section modes for the elements near the joint and 8 cross-section modes for the remaining elements

APPENDIX G.

Effectiveness of the proposed joint condition for the GBT modes

The numerical tests are implemented for the structures in Section 4.3.2 to check whether the proposed joint condition works with the GBT modes. Figure F.1 shows the torsional rotation and linear warping modes obtained by analyzing the structure in Section 4.3.2.1, and Table F.1 shows the modal analysis results of the structure in Section 4.3.2.2. From the results, it is found that the proposed joint condition is effective not only for the proposed cross-section modes but also for the GBT modes, although some results seem to be slightly differ from those of the shell.

Table G.1 Natural frequencies (Hz) from the vibration analysis of an L-type joint structure in Section 4.3.2.2 (numbers in parentheses denote the differences (%) from the shell results)

Mode	Shell	GBT	Proposed	GBT modes & Proposed joint condition
1	27.92	28.21 (1.1)	27.42 (1.8)	27.77 (0.5)
2	28.90	29.23 (1.1)	28.38 (1.8)	28.72 (0.6)
3	38.24	39.02 (2.0)	37.66 (1.5)	37.56 (1.8)
4	40.63	42.23 (3.9)	40.40 (0.6)	40.75 (0.3)
5	77.67	79.45 (2.3)	78.63 (1.2)	79.60 (2.5)
6	90.98	91.87 (1.0)	90.03 (1.0)	91.05 (0.1)
7	95.93	99.49 (3.7)	95.68 (0.3)	93.49 (2.5)
8	108.06	112.42 (4.0)	108.13 (0.1)	108.77 (0.7)
9	118.68	122.43 (3.2)	117.97 (0.6)	117.09 (1.3)
10	144.94	149.09 (2.9)	143.24 (1.2)	119.21 (17.8)
11	147.80	153.34 (3.7)	148.05 (0.2)	145.58 (1.5)
12	160.07	164.61 (2.8)	165.21 (3.2)	164.44 (2.7)
13	179.67	185.93 (3.5)	176.29 (1.9)	177.93 (1.0)
14	223.83	231.94 (3.6)	217.10 (3.0)	219.15 (2.1)
15	234.54	241.16 (2.8)	231.70 (1.2)	233.98 (0.2)

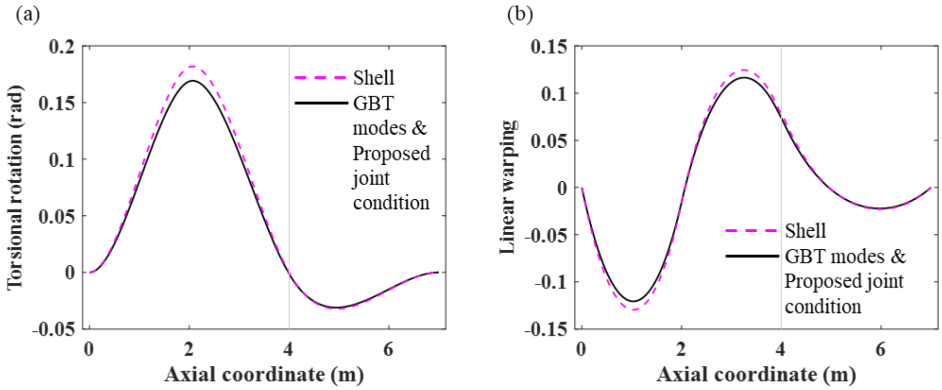

Fig. G.1 Static analysis results of the problem in Section 4.3.2.1 using GBT modes with the proposed joint condition: (a) torsional rotation and (b) linear warping mode

REFERENCES

[1] V.Z. Vlasov, Thin-walled elastic beams, Israel Program for Scientific Translations, Jerusalem, 1961.

[2] E. Carrera, G. Giunta, M. Petrolo, Beam structures: classical and advanced theories, John Wiley & Sons, Chichester, 2011.

[3] E. Carrera, E. Zappino, Carrera unified formulation for free-vibration analysis of aircraft structures, AIAA Journal, 54(1) (2016) 280-292.

[4] E. Carrera, A. Pagani, Accurate response of wing structures to free-vibration, load factors, and nonstructural masses, AIAA Journal, 54(1) (2016) 227-241.

[5] J.H. Kim, Y.Y. Kim, One-dimensional analysis of thin-walled closed beams having general cross-sections, International Journal for Numerical Methods in Engineering, 49(5) (2000) 653-668.

[6] I.S. Choi, G.-W. Jang, S. Choi, D. Shin, Y.Y. Kim, Higher order analysis of thin-walled beams with axially varying quadrilateral cross sections, Computers & Structures, 179 (2017) 127-139.

[7] H. Kim, G.-W. Jang, Higher-order thin-walled beam analysis for axially varying generally shaped cross sections with straight cross-section edges, Computers & Structures, 189 (2017) 83-100.

[8] M.K. Ferradi, X. Cespedes, A new beam element with transversal and warping eigenmodes, Computers & Structures, 131 (2014) 12-33.

[9] R. Schardt, Verallgemeinerte Technische Biegetheorie: Lineare Probleme,

Springer-Verlag, Berlin, 1989.

[10] R. Schardt, Generalized beam theory-an adequate method for coupled stability problems, Thin-Walled Structures, 19(2-4) (1994) 161-180.

[11] R. Schardt, Lateral torsional and distortional buckling of channel- and hat-sections, Journal of Constructional Steel Research, 31(2–3) (1994) 243-265.

[12] R. Goncalves, M. Ritto-Correa, D. Camotim, A new approach to the calculation of cross-section deformation modes in the framework of generalized beam theory, Computational Mechanics, 46(5) (2010) 759-781.

[13] N. Silvestre, D. Camotim, N.F. Silva, Generalised Beam Theory Revisited: from the kinematical assumptions to the deformation mode determination, International Journal of Structural Stability and Dynamics, 11(5) (2011) 969-997.

[14] R. Goncalves, R. Bebiano, D. Camotim, On the shear deformation modes in the framework of generalized beam theory, Thin-Walled Structures, 84 (2014) 325-334.

[15] R. Bebiano, R. Goncalves, D. Camotim, A cross-section analysis procedure to rationalise and automate the performance of GBT-based structural analyses, Thin-Walled Structures, 92 (2015) 29-47.

[16] R. Goncalves, D. Camotim, On distortion of symmetric and periodic open-section thin-walled members, Thin-Walled Structures, 94 (2015) 314-324.

[17] R. Goncalves, D. Camotim, GBT deformation modes for curved thin-walled cross-sections based on a mid-line polygonal approximation, Thin-Walled Structures, 103 (2016) 231-243.

[18] A. Genoese, A. Genoese, A. Bilotta, G. Garcea, A mixed beam model with non-uniform warpings derived from the Saint Venànt rod, Computers & Structures, 121 (2013) 87-98.

[19] A. Genoese, A. Genoese, A. Bilotta, G. Garcea, A generalized model for heterogeneous and anisotropic beams including section distortions, Thin-Walled Structures, 74 (2014) 85-103.

[20] A. Genoese, A. Genoese, A. Bilotta, G. Garcea, A composite beam model including variable warping effects derived from a generalized Saint Venant solution, Composite Structures, 110 (2014) 140-151.

[21] A. Genoese, A. Genoese, A. Bilotta, G. Garcea, A geometrically exact beam model with non-uniform warping coherently derived from the Saint Venant rod, Engineering Structures, 68 (2014) 33-46.

[22] A. Genoese, A. Genoese, A. Bilotta, G. Garcea, Buckling analysis through a generalized beam model including section distortions, Thin-Walled Structures, 85 (2014), 125-141.

[23] G. Garcea, R. Goncalves, A. Bilotta, D. Manta, R. Bebiano, L. Leonetti, D. Magisano, D. Camotim, Deformation modes of thin-walled members: A comparison between the method of Generalized Eigenvectors and Generalized Beam Theory, Thin-Walled Structures, 100 (2016) 192-212.

[24] B.D. Saint-Venant, Mémoire sur la torsion des prismes, Mémoires des Savants étrangers, 14 (1855) 233-560.

[25] D. Iesan, Classical and generalized models of elastic rods, CRC Press, Boca

Raton, 2008.

[26] P. Ladevèze, J. Simmonds, New concepts for linear beam theory with arbitrary geometry and loading, European Journal of Mechanics - A/Solids, 17(3) (1998) 377-402.

[27] S.B. Dong, J.B. Kosmatka, H.C. Lin, On saint-venant's problem for an inhomogeneous, anisotropic cylinder-part i: Methodology for saint-venant solutions, Journal of Applied Mechanics, 68(3) (2001) 376-381.

[28] R. El Fatmi, N. Ghazouani, Higher order composite beam theory built on Saint-Venant's solution. Part-I: Theoretical developments, Composite Structures, 93(2) (2011) 557-566.

[29] R.F. Vieira, F.B.E. Virtuoso, E.B.R. Pereira, A higher order thin-walled beam model including warping and shear modes, International Journal of Mechanical Sciences, 66 (2013) 67-82.

[30] R.F. Vieira, F.B. Virtuoso, E.B.R. Pereira, A higher order model for thin-walled structures with deformable cross-sections, International Journal of Solids and Structures, 51(3-4) (2014) 575-598.

[31] R. Vieira, F. Virtuoso, E. Pereira, Definition of warping modes within the context of a higher order thin-walled beam model, Computers & Structures, 147 (2015) 68-78.

[32] D.H. Hodges, Nonlinear composite beam theory, AIAA, Washington, DC, 2006.

[33] W. Yu, V.V. Volovoi, D.H. Hodges, X. Hong, Validation of the variational

asymptotic beam sectional analysis, AIAA Journal, 40 (2002) 2105-2112.

[34] W. Yu, D.H. Hodges, J.C. Ho, Variational asymptotic beam sectional analysis-an updated version, International Journal of Engineering Science, 59 (2012) 40-64.

[35] D. Shin, S. Choi, G.-W. Jang, Y.Y. Kim, Higher-order beam theory for static and vibration analysis of composite thin-walled box beam, Composite Structures, 206 (2018) 140-154.

[36] J.H. Kim, Y.Y. Kim, Analysis of thin-walled closed beams with general quadrilateral cross sections, ASME Journal of Applied Mechanics, 66(4) (1999) 904-912.

[37] S. Choi, Y.Y. Kim, Exact matching at a joint of multiply-connected box beams under out-of-plane bending and torsion, Engineering Structures, 124 (2016) 96–112.

[38] S. Choi, Y.Y. Kim, Consistent higher-order beam theory for thin-walled box beams using recursive analysis: Membrane deformation under doubly symmetric loads, Engineering Structures, 197 (2019) 109430.

[39] S. Choi, Y.Y. Kim, Consistent higher-order beam theory for thin-walled box beams using recursive analysis: Edge-bending deformation under doubly symmetric loads, Engineering Structures, 206 (2019) 110129.

[40] J. Kim, S. Choi, Y.Y. Kim, G.-W. Jang, Hierarchical Derivation of Orthogonal Cross-section Modes for Thin-walled Beams with Arbitrary Sections, Thin-Walled Structures (Submitted).

[41] F.G.A. AI-Bermani, B. Li, K. Zhu, S. Kitipornchai, Cyclic and seismic response of flexibly jointed flames, Engineering Structures, 16(4) (1994) 249-255.

[42] K. Zhu, F.G.A. AI-Bermani, S. Kitipornchai, B. Li, Dynamic response of flexibly jointed frames, Engineering Structures, 17(8) (1995) 575-580.

[43] M.E.M. El-Sayed, Calculation of joint spring rates using finite element formulation, Computers & Structures, 33(4) (1989) 977-981.

[44] K. Lee, E. Nikolaidis, A two-dimensional model for joints in vehicle structures, Computers & Structures, 45(4) (1992) 775-784.

[45] W. Na, S. Lee, J. Park, Body optimization for front loading design process, SAE Technical Paper, 2014-01-0388 (2014).

[46] D.S. Sophianopoulos, The effect of joint flexibility on the free elastic vibration characteristics of steel plane frames, Journal of Constructional Steel Research, 59(8) (2003) 995-1008.

[47] A.S. Galvao, A.R.D. Silva, R.A.M. Silveira, P.B. Goncalves, Nonlinear dynamic behavior and instability of slender frames with semi-rigid connections, International Journal of Mechanical Sciences, 52(12) (2010) 1547-1562.

[48] W. Zuo, W. Li, T. Xu, S. Xuan, J. Na, A complete development process of finite element software for body-in-white structure with semi-rigid beams in. NET framework, Advances in Engineering Software, 45(1) (2012) 261-271.

[49] S. Kameyama, S. Fujita, S. Kaji, Elementary body structure analysis, SAE International Journal of Passenger Cars-Mechanical Systems, 8(1) (2015) 73-81.

[50] S. Donders, Y. Takahashi, R. Hadjit, T.V. Langenhove, M. Brughmans, A reduced beam and joint concept modeling approach to optimize global vehicle body dynamics, Finite Elements in Analysis and Design, 45(6-7) (2009) 439-455.

[51] G.D. Gaetano, D. Mundo, F.I. Cosco, C. Maletta, S. Donders, Concept modelling of vehicle joints and beam-like structures through dynamic FE-based methods, Shock and Vibration, 2014 (2014).

[52] A.H. Baigent, G.J. Hancock, Structural analysis of assemblages of thin-walled members, Engineering Structures, 4(3) (1982) 207-216.

[53] P.W. Sharman, Analysis of structures with thin-walled open sections, International Journal of Mechanical Sciences, 27(10) (1985) 665-677.

[54] S. Krenk, L. Damkilde, Warping of joints in I-beam assemblages, Journal of Engineering Mechanics, 117(11) (1991) 2457-2474.

[55] S. Choi, G.-W. Jang, Y.Y. Kim, Exact matching condition at a joint of thin-walled box beams under out-of-plane bending and torsion, Journal of Applied Mechanics, 79(5) (2012) 051018.

[56] S. Choi, Y.Y. Kim, Analysis of two box beams-joint systems under in-plane bending and axial loads by one-dimensional higher-order beam theory, International Journal of Solids and Structures, 90 (2016) 69-94.

[57] G.-W. Jang, K.J. Kim, Y.Y. Kim, Higher-order beam analysis of box beams connected at angled joints subject to out-of-plane bending and torsion, International Journal for Numerical Methods in Engineering, 75(11) (2008) 1361-1384.

[58] G.-W. Jang, Y.Y. Kim, Higher-order in-plane bending analysis of box beams connected at an angled joint considering cross-sectional bending warping and distortion, Thin-Walled Structures, 47(12) (2009) 1478-1489.

[59] G.-W. Jang, Y.Y. Kim, Vibration analysis of piecewise straight thin-walled box beams without using artificial joint springs, Journal of Sound and Vibration, 326(3–5) (2009) 647-670.

[60] G.-W. Jang, Y.Y. Kim, Fully coupled 10-degree-of-freedom beam theory for piecewise straight thin-walled beams with general quadrilateral cross sections, Journal of Structural Engineering, 136(12) (2010) 1596-1607.

[61] G.-W. Jang, S. Choi, Y.Y. Kim, Analysis of three thin-walled box beams connected at a joint under out-of-plane bending loads, Journal of Engineering Mechanics, 139(10) (2013) 1350-1361.

[62] C. Basaglia, D. Camotim, N. Silvestre, Global buckling analysis of plane and space thin-walled frames in the context of GBT, Thin-Walled Structures, 46(1) (2008) 79-101.

[63] C. Basaglia, D. Camotim, N. Silvestre, GBT-based local, distortional and global buckling analysis of thin-walled steel frames, Thin-Walled Structures, 47(11) (2009) 1246-1264.

[64] D. Camotim, C. Basaglia, N. Silvestre, GBT buckling analysis of thin-walled steel frames: a state-of-the-art report, Thin-Walled Structures, 48(10–11) (2010) 726-743.

[65] C. Basaglia, D. Camotim, N. Silvestre, GBT-based buckling analysis of thin-walled steel frames with arbitrary loading and support conditions, International Journal of Structural Stability and Dynamics, 10(3) (2010) 363-385.

[66] C. Basaglia, D. Camotim, N. Silvestre, Torsion warping transmission at thin-

walled frame joints: Kinematics, modelling and structural response, Journal of Constructional Steel Research, 69(1) (2012) 39-53.

[67] C. Basaglia, D. Camotim, N. Silvestre, Post-buckling analysis of thin-walled steel frames using generalised beam theory (GBT), Thin-Walled Structures, 62 (2013) 229-242.

[68] C. Basaglia, D. Camotim, Buckling analysis of thin-walled steel structural systems using generalized beam theory (GBT), International Journal of Structural Stability and Dynamics, 15(1) (2015) 1540004.

[69] C. Basaglia, D. Camotim, N. Silvestre, Buckling and vibration analysis of cold-formed steel CHS members and frames using generalized beam theory, International Journal of Structural Stability and Dynamics, 15(8) (2015) 1540021.

[70] C. Basaglia, D. Camotim, H.B. Coda, Generalised beam theory (GBT) formulation to analyse the vibration behaviour of thin-walled steel frames, Thin-Walled Structures, 127 (2018) 259-274.

ABSTRACT (KOREAN)

임의 단면을 갖는 박판 보 연결 구조의 일차원 모델링

김 재 용
서울대학교 대학원
기계항공공학부

일차원 해석 모델에서는 단면 모드를 통해 변위장이 표현되기 때문에 고려되는 단면 모드의 정의 방법과 개수는 해석 정확도에 큰 영향을 미친다. Euler-Bernoulli 보나 Timoshenko 보 이론과 같은 고전 보 이론에서는 여섯 개의 단면 강체모드만이 고려되기 때문에 상세 변형이 표현되지 않으며, 결과적으로 실제보다 구조 강성이 높게 계산된다. 이와 같은 고전 보 이론의 한계점은 보 단면의 뒤틀림(distortion)이나 일그러짐(warping) 변형을 나타내는 고차 모드를 고려함으로써 해결될 수 있다. 고차 모드는 보의 복잡한 변위 분포를 표현함으로써 강성이 정확하게 평가되도록 하며 역학적 특성을 반영할 수 있도록 정의되어야 한다.

고차 모드는 연결된 보 구조물 해석 시 주의 깊게 다뤄져야 한다. 일차

원 해석 모델에서는 여러 개의 보가 연결되는 조인트에서 단면 모드 커플링 관계(조인트 조건)가 정의되어야 한다. 고전 보 이론에서는 단면 강체모드의 조인트 조건이 좌표 변환 행렬을 이용해 간단하게 정의되지만, 결과력을 발생시키지 않는 고차 모드의 경우 방향성을 지니지 않기 때문에 기존 방법으로는 조인트 조건을 정의할 수 없다.

본 논문에서는 임의 단면을 갖는 박판 보에 적용 가능한 단면 모드 정의 방법론과 조인트 조건이 제안된다. 제안하는 단면 모드 정의 방법론에서는 평면 응력 상태에 대한 구성 방정식으로부터 단면 모드 식이 유도되고, 그 식은 단면 모드의 직교 조건을 이용해 고윳값 문제로 변환된다. 이 고윳값 문제를 풂으로써 구해진 고유벡터들을 기반으로 한 세트의 단면 모드들이 정의된다. 이러한 과정이 반복되면서 단면 모드는 저차 세트부터 고차 세트까지 반복적으로 유도된다. 제안하는 조인트 조건은 단면 연결점(connection point)에서 변위 및 회전각 연속 조건을 부여함으로써 정의된다. 연결점은 단면의 형상에 관계없이 일관된 방법으로 지정되기 때문에 다양한 부재로 구성되는 복잡한 보 구조물에 대해서도 조인트 조건을 정의할 수 있다. 또한 보 단면과 조인트 단면이 일치하지 않음에 따라 발생되는 조인트 단면에서의 추가 변위를 고려함으로써 정확한 해석이 가능하다. 타당성 검증을 위해, 제안하는 일차원 모델링 방법론을 이용해 다양한 예제를 풀고 쉘(shell) 해석 결과와 비교해 보았다. 검증을

통해, 제안하는 방법으로 임의 단면을 갖는 복잡한 보 구조물을 고전 보 대비 정확하게 해석 가능함을 확인하였다.

주요어: 박판 보, 단면 모드, 고차 보 이론, 보 구조, 조인트 조건, 모드 커플링 관계

학 번 : 2016-30174